Electromagnetic Generators for Portable Power Applications

by

Matthew Kurt Senesky

B.A. (Dartmouth College) 1998
B.Eng. (Dartmouth College, Thayer School of Engineering) 1999
M.S. (University of California, Berkeley) 2003

A dissertation submitted in partial satisfaction of the
requirements for the degree of
Doctor of Philosophy

in

Engineering – Electrical Engineering and Computer Sciences

in the

GRADUATE DIVISION
of the
UNIVERSITY OF CALIFORNIA, BERKELEY

Committee in charge:
Professor Seth R. Sanders, Chair
Professor Albert P. Pisano
Professor Dennis K. Lieu

Spring 2005

The dissertation of Matthew Kurt Senesky is approved:

Chair Date

Date

Date

University of California, Berkeley

Spring 2005

Electromagnetic Generators for Portable Power Applications

by

Matthew Kurt Senesky

Abstract

Electromagnetic Generators for Portable Power Applications

by

Matthew Kurt Senesky

Doctor of Philosophy in Engineering – Electrical Engineering and Computer Sciences

University of California, Berkeley

Professor Seth R. Sanders, Chair

The power source that is common to almost all electrically powered portable devices — the electrochemical battery — has failed to shrink at the same rate as circuits and sensors. While this growing disparity has been partially mitigated by the decreasing power requirements of many electronic circuits, the size and weight of portable electronic devices are increasingly dominated by electrochemical batteries. An obvious set of candidates for energy storage with higher levels of specific energy are hydrocarbon fuels, long used in transportation applications for just this reason.

Several recent research efforts have sought to capitalize on the high specific energy of chemical fuels through the use of MEMS engines or turbines paired with electrical generators. Producing such a system to run efficiently on the milli- or microscale,

however, poses considerable challenges in thermal and fluid management, combustion processes, and electromechanical energy conversion.

The contribution of the research presented in this dissertation is in the area of electromechanical energy conversion. The design, construction and testing of an electrical generator intended for interface with a MEMS–scale IC engine are presented. The majority of the generator structure is built at the millimeter scale from discrete parts, with only the rotor being microfabricated. We believe that this approach offers superior performance as compared to purely microfabricated generators for power outputs on the order of milliWatts and above, with only a modest penalty in mass and volume.

Some of the design ideas from this millimeter scale generator are then extended to the macro scale, with focus on a power range of tens to hundreds of Watts. The application of interest is a generator for combustion-based portable power systems, and hence power density is a key metric. However, there are an enormous number of applications over a wide range of power levels — from implantable medical devices to power tools to electric vehicle drives to wind power generation — that would benefit from high-density motor or generator technology.

Professor Seth R. Sanders
Dissertation Committee Chair

To my mother,

for passing her cleverness on to her children,

my father,

for teaching me the value of hard work through tireless example,

my sister,

for helping me to cope with the effects of cleverness and hard work,

and Debbie,

for seeing my qualities and ignoring my faults.

Contents

List of Figures

List of Tables

Acknowledgments

I'd like to thank foremost Seth Sanders, for his patient guidance and instruction, optimistic nature, and willingness to entertain new ideas. I'd also like to thank Al Pisano, for developing the compelling idea behind the MEMS REPS project, for his input to my research, and for his heroic efforts to secure funding for many hungry students. Dave Walther contributed many insights to my efforts as well, both technical and humorous. I'd like to thank all the other members of the MEMS REPS team, particularly Aaron Knobloch, Debbie Jones, and Fabian Martinez for their work in adapting the Wankel rotor to my magnetic demands. Finally, I'd like to thank my friends and family, for their love and support.

Chapter 1

Portable Power

We have made progress in the manufacturing of small things. Moore's law has held, miraculously, since it was posed in 1965; the number of transistors that can fit on a microchip doubles approximately every 12-18 months. Over the last 15-20 years, the field of MEMS — microelectromechanical systems — has grown from a laboratory curiosity into an area of intense research and commercial opportunity. We reap the benefits of these and other technological advancements every day, with the use of increasingly convenient, increasingly commonplace and increasingly small portable electronic devices.

However, a bottleneck looms on the horizon. The power source that is common to almost all electrically powered portable applications — the electrochemical battery — has failed to shrink at the same rate as circuits and sensors. While this disparity has been partially mitigated by the decreasing power requirements of many electronic circuits, the size and weight of portable electronic devices are increasingly dominated by electrochemical batteries.

For applications such as cellular telephones and laptop computers, the size of batteries has thus far been a manageable problem. The robust sales of these devices attest to the fact that consumers find them relatively convenient. By the same measure, however, a huge commercial windfall is available to the inventor of a cost-effective technology to improve on the energy storage capability of state of the art batteries. In a competitive marketplace, portable electronic products with the increased run-time or increased functionality provided by an improved power source will be extremely attractive to consumers.

Beyond the consumer market, there exist a large number of applications for which even the best batteries are unsatisfactory. These include the most demanding military applications, for which relatively high power levels are expected over mission lengths that far exceed consumer demands, and sensor networks, which draw low levels of power but require extremely high energy storage densities to achieve truly ubiquitous application.

The remainder of this chapter will present some of the more compelling applications of small-scale power sources, followed by an overview of proposed technology solutions.

1.1 Applications and Trends

1.1.1 Consumer Electronics

Cellular telephones and notebook computers have both experienced a boom in popularity in the last decade. Between 1992 and 2001, sales of notebook computers in the United States increased almost five-fold, reaching 8.8 million units in 2001 (Fig. 1.1a). Cellular telephones have shown an even more dramatic proliferation, with units in use worldwide increasing from 1 million in 1991 to 1.35 billion in 2003 (Fig. 1.1b).

The power requirements of both notebook computers and cellular telephones are currently met by lithium-ion (Li-Ion) batteries. A notebook computer in active operation can use power on the order of tens of Watts, while a cellular telephone in talk mode may use on the order of a few Watts. The batteries in both devices are sized so as to give the user about 4 hours of active operation.

For both types of device, the battery makes up a large fraction of the overall mass, particularly for the smallest products. One of the smallest available cellular phones, the Ericsson T66, has an overall mass of 59 grams, with a battery mass of 20 grams. Thus the battery represents more than one third of the total mass [1],[2]. A lightweight notebook computer, the Dell Latitude X300, has a mass of 1.32 kg, to which the battery contributes 0.45 kg. Again the battery makes up just over one third of the total mass [3],[4].

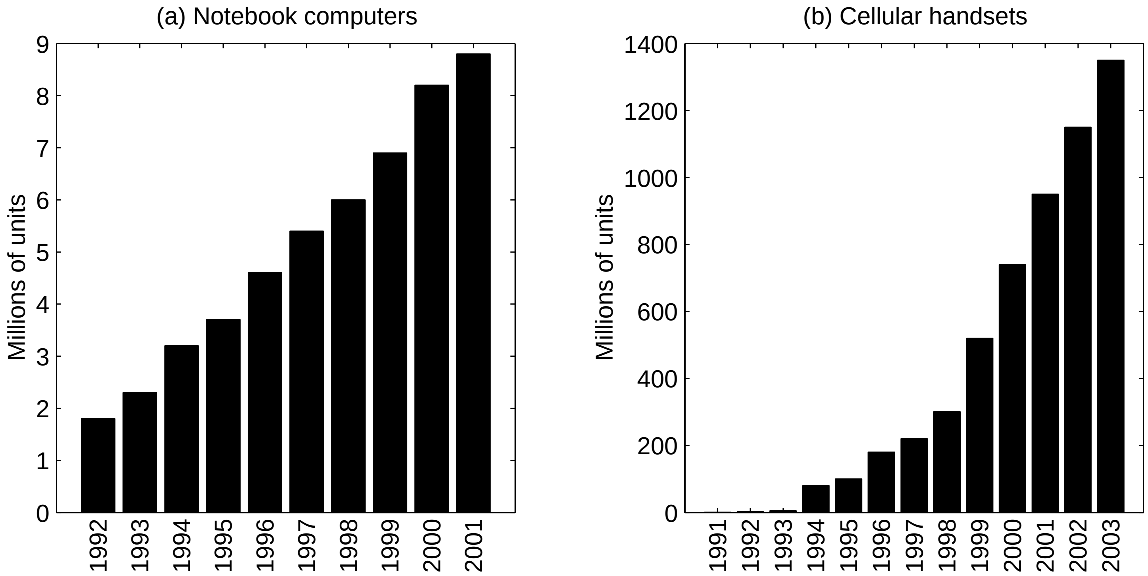

Figure 1.1: (a) Consumption of notebook computers, United States. [5] (b) Number of cellular handsets in use, worldwide. [6]

1.1.2 Military Applications

Military applications often present the most demanding power requirements. Light weight and high energy storage are key concerns for power sources, while cost is less important than in consumer applications. Meeting the power requirements of an individual soldier is particularly challenging. A recent series of reports ([7], [8], [9]) estimates that in the near future, the average power needed to operate all the electronic systems carried by a soldier will be 20 Watts, with peak power consumption of almost 70 Watts. A microclimate cooling system for chemical hazard suits is projected to consume 100-150 Watts. Meanwhile, Army researchers have asserted that no good solution currently exists for supplying power levels between 20 and 3,000 Watts [10].

1.1.3 Human Exoskeleton

Human exoskeletons are currently under investigation as a means of enhancing the mechanical performance of the human body. By means of wearable mechanical elements that supplement the force producing capability of the major muscle groups, the user's productivity could be enhanced in a warehouse or construction setting, or in a military environment.

Researchers have estimated that the act of walking (4.5 mph), for a combined exoskeleton and payload of 350 pounds, requires 310 Watts. If, in addition to walking, a 100 lb. payload is lifted at 1 ft/s, power demand rises to 440 W. The act of running (6.7 mph), again with an overall weight of 350 lbs. but with no lifting, is estimated to consume 600 W in steady-state, with peak power requirements for rapid motions reaching up to 2 kW [11].

1.1.4 Micro and Nano Air Vehicles

Several research efforts have recently created startlingly small flying vehicles. Fixed wing [12], rotary wing [13], and flapping wing craft have all been demonstrated with varying levels of success. It has been estimated that the minimum power required to keep a 50 gram MAV aloft is 600 mW [14]. The 80 gram fixed wing vehicle described in [12] draws 4.35 W for propulsion, while the 12.3 gram rotary wing craft in [13] draws 3.5 W.

1.1.5 Sensor Networks

Sensor networks are envisioned as enabling data collection over large areas at unprecedented spatial resolution. Large numbers of small, low-cost sensor "nodes", each combining sensor functionality with a radio transceiver, work in collaboration to collect data and transmit it to a base station via an ad-hoc wireless network. These networks are intended in many cases to operate for a period of months or years. Because of the large numbers of devices and their small size, changing batteries is in many cases not feasible. Thus energy storage requirements are extreme.

Table 1.1, reproduced from [15], gives the power requirements envisioned for nodes of various type and function. A simple calculation indicates that if a 1 mm^3 specialized sensing node is to run exclusively from stored energy, an average power of 2 μW over a period of 5 years requires 87.6 milliWatt-hours. Assuming the entire device volume is devoted to energy storage, a storage medium with energy density of 87.6 kWh/liter is required. Based on the data in Sec. 1.2.2, this is denser than the best available batteries by almost two orders of magnitude.

1.2 Technology

1.2.1 Energy Harvesting

A possible avenue for mitigating difficult energy storage requirements in some applications is energy harvesting or scavenging. Energy that can be captured from

Type	Size	Application	Power (Active)	Power (Sleep)	Duty Cycle
Specialized sensing	1 mm^3	Specialized low-bandwidth sensor or advanced RF tag	1.8 V, 10-15 mA	1.8 V, 1 μA	0.1-0.5 %
Generic sensing	1–10 cm^3	General purpose sensing and communications relay	3 V, 10-15 mA	3 V, 10 μA	1-2 %
High-bandwidth sensing	1–10 cm^3	High-bandwidth sensing (video, acoustic, and vibration)	3 V, 60 mA	3 V, 100 μA	5-10 %
Gateway	$>$ 10 cm^3	High-bandwidth sensing and communications aggregation gateway node	3 V, 200 mA	3 V, 10 mA	$>$ 50 %

Table 1.1: Various classes of sensor nodes [15].

the surrounding environment does not have to be stored. There are many possible effects that can be exploited, including solar, mechanical vibration, thermal gradients, wind, acoustic, RF, and human power. The most promising of these in the near term are perhaps solar power via photovoltaics, and vibrational energy harvesting devices.

Light reaching the earth's surface on a sunny day outdoors has energy per area of approximately 100 mW/cm^2. Indoors, in an office environment, this can drop to 100 μW/cm^2 [16]. Accounting for variation in light levels, in a typical sunny outdoor location in the United States, expected energy is about 700 mWh/day/cm^2 [17]. Of course, this must be derated by the efficiency of conversion. The best available multiple junction photovoltaic cells have a solar to electric conversion efficiency of 35% [17].

Vibrational energy harvesting is typically accomplished with a proof mass mounted on a spring element, coupled to an electromechanical transducer. Electromagnetic [18], electrostatic [19], and piezoelectric [20] transducers have all been attempted. The harvesting of vibrational energy is best suited to applications where the device can be mounted to a rigid, vibrating body, and frequencies of vibration are well-characterized. Uncertain placement, dissipative substrates, or frequencies far from the device resonance can adversely affect performance.

1.2.2 Batteries

Electrochemical batteries are by far the dominant technology for portable power applications. Of commercially available battery types, lithium–thionyl chloride (Li–$SOCl_2$) has the highest specific energy among primary batteries at present (660 Wh/kg), while lithium–sulfur (Li–S) leads among secondary batteries (370 Wh/kg) [21]. Data for other primary and secondary battery chemistries are given in Tables 1.2 and 1.3 respectively.

However, batteries have several disadvantages. Specific energy storage is quite low as compared to chemical fuels (see Section 1.2.4). Specific power is modest, limited by internal resistance. Secondary batteries have poor cycling characteristics; some, such as nickel-cadmium (Ni-Cd), exhibit memory effects that place strict requirements on recharging. Performance of all secondary battery types degrades with the number of charge/discharge cycles. An extreme limit is perhaps 30,000 cycles for a carefully designed and controlled system [17], with most batteries having a useful life of between 100 and 1000 cycles. The voltage of a battery decreases as energy is removed. And finally, many batteries are made from toxic chemicals, including mercury, cadmium and lead, that pose disposal problems.

Type	Specific Energy [Wh/kg]	Energy Density [Wh/l]	Ref.
Lithium-thionyl chloride	320-660	700-1080	[7, 11, 21]
Lithium-vanadium pentoxide	264	660	[21]
Lithium-sulfur dioxide	260-330	415-420	[7, 21]
Lithium-carbon monofluoride	250	600	[7]
Lithium-manganese dioxide	230	550	[7]
Lithium-iodine	200	530	[21]
Lithium-iron disulfide	130	400	[7]
Lithium-sulfuryl chloride	450	900	[7]
Aluminum-air	300-350	240	[7, 11]
Zinc-air	150-500	180-1050	[7, 21]
Carbon-zinc	55-85	120-165	[7, 21]
Zinc chloride	88	183	[21]
Mercury-zinc	99-123	300-500	[21]
Mercury-cadmium-bismuth	77	201	[21]
Mercury-cadmium	22	73	[21]
Alkaline manganese	66-99	122-268	[21]

Table 1.2: Specific energy and energy density of selected primary batteries.

1.2.3 Fuel Cells

A vast body of literature exists detailing the many types of fuel cells. A comprehensive treatment of the subject is beyond the scope of this work. However, a brief overview of fuel cell technologies appropriate for moderate power levels (>3 kW) is presented here for comparison to other small-scale power technologies. At

Type	Specific Energy [Wh/kg]	Energy Density [Wh/l]	Ref.
Lithium-sulfur	370	—	[21]
Lithium-chlorine	330	—	[21]
Li-NiO_2	155	325	[7]
Li-Mn_2O_4	140	300	[7]
Li ion	100-250	—	[11]
Li-CoO_2	95	235	[7]
Zinc-chlorine	130	—	[21]
Zinc-air	110-150	130	[7, 21]
Sodium-sulfur	240	—	[21]
Nickel-zinc	65-80	60-150	[7, 21]
Nickel-hydrogen	55-60	60	[7]
Nickel-metal hydride	55-70	120	[7]
Nickel-iron	35-60	70	[7]
Nickel-cadmium	18-55	37-120	[11, 21]
Silver-cadmium	60-95	110	[7, 11]
Silver-zinc	37-220	55-610	[21]
Lead-acid	18-50	31-85	[7, 21]

Table 1.3: Specific energy and energy density of selected secondary batteries.

present, proton exchange membrane fuel cells (PEMFCs), direct methanol fuel cells (DMFCs), and formic acid fuel cells (FAFCs) are leading candidates for portable fuel cell technology.

Polymer electrolyte membrane fuel cells oxidize pure hydrogen, and allow the protons to pass through a membrane. The electrons pass through the load circuit, delivering power. Because the protons recombine with oxygen at the other side of the membrane, water is the only byproduct of the reaction. PEMFCs can reach efficiencies of up to 60%, and specific power of approximately 1 kW/kg [9]. The technology has yet to see widespread use, however, because of several drawbacks. The storage of compressed hydrogen fuel presents the danger of explosion; the required containment vessels significantly increase system mass. The fuel cell membrane can be poisoned by small amounts of carbon monoxide (CO), requiring clean hydrogen sources. And it is necessary to precisely regulate the amount of water in the system, adding to the balance-of-plant (BOP).

Direct methanol fuel cells are similar to PEMFCs in construction, typically using the same membrane and cathode catalyst. Methanol presents less danger than hydrogen of sudden explosion, and hence DMFCs do away with ponderous containment vessels. However, a less efficient catalyst reaction reduces efficiency to approximately 40% [8]. Power density is modest at 0.2 W/kg [9]. DMFCs suffer from the same poisoning and water management problems as PEMFCs, with the additional problem of methanol crossover — leakage of unreacted fuel across the membrane — which further complicates the BOP and reduces practical efficiency.

A relatively recent development is the formic acid fuel cell [22]. Formic acid is the toxin secreted by black ants; its high acidity is a drawback for use around human operators. Further, formic acid has less than half the energy density of methanol (see Table 1.4). FAFCs can operate with higher fuel concentrations than DMFCs however, and can do so at ambient temperature. A FAFC has been presented ([23]) that achieves an area-wise power density of 110 mW/cm^2.

1.2.4 Power MEMS

An obvious set of candidates for energy storage with higher levels of specific energy are hydrocarbon fuels, long used in transportation applications for just this reason. Gasoline, as shown in Table 1.4, has specific energy of 12.2 kWh/kg, roughly 18 times that of Li–$SOCl_2$ batteries and 33 times that of Li–S batteries; the more appropriate comparison is with the primary technology however. Of course, chemical to thermal, thermal to mechanical, and mechanical to electrical conversion efficiencies must be taken into account in considering hydrocarbon fuels. However, a 10% overall conversion efficiency still results in a higher specific energy than the best available primary batteries.

Several recent research efforts have sought to capitalize on the high specific energy of chemical fuels through the use of MEMS engines or turbines paired with electrical generators [24], [25]. Producing such a system to run efficiently on the milli- or microscale, however, poses considerable challenges in thermal and fluid management, combustion processes, and electromechanical energy conversion.

Fuel	Specific Energy [kWh/kg]	Energy Density [kWh/l]	Ref.
Hydrogen	33.566	2.368	[9]
Propane	12.869	7.485	[9]
Methane	367.937	1.892	[9]
Butane	12.702	7.186	[9]
Gasoline	12.329	9.057	[9]
Diesel	11.9	—	[7]
JP-8	12.006	9.925	[9]
Methanol	5.616	4.466	[9]
Ethanol	7.488	5.893	[9]
Formic Acid	—	2.086	[23]

Table 1.4: Specific energy and energy density of selected fuels.

1.3 The MEMS Rotary Engine Power System

1.3.1 Concept

The MEMS Rotary Engine Power System is intended to be a replacement for electrochemical batteries. The system is comprised of a MEMS IC engine, a millimeter-scale generator, and ancillary equipment to provide for fuel delivery and thermal management. If the fuel reservoir mass dominates the rest of the hardware, the specific energy of the system approaches that of the fuel, derated by the conversion efficiency. Utilizing a high specific energy fuel such as those listed in Table 1.4, and assuming moderate conversion efficiencies, the overall system mass can be smaller than that of a battery of equivalent energy storage.

1.3.2 MEMS Wankel Engine

The IC engine to be used in the system is a microfabricated Wankel engine. The Wankel engine has several advantages for such an application: it is inherently planar, making it amenable to microfabrication; it is self-valving, reducing the number of parts and complexity of the design; and like diesel engines, it can burn a wide range of fuels. Sealing is a known problem of Wankel engines, and this problem can become more severe at small scales as relative tolerances become worse.

The engine is fabricated with a deep reactive ion etch process [26, 27]; it consists of a housing, shaft and rotor. The rotor is the most sophisticated component, having electroplated nickel-iron poles [28], as well as integrated cantilever tip seals [29].

1.3.3 Generator

One of the contributions of the research presented in this dissertation is in the design, construction and testing of an electrical generator intended for interface with a MEMS–scale IC engine. The majority of the generator structure is built at the millimeter scale from discrete parts, with only the rotor being microfabricated. We believe that this approach offers superior performance as compared to purely microfabricated generators for power outputs on the order of milliWatts and above, with only a modest penalty in mass and volume.

The engine and generator are integrated into a single unit by mounting the generator stator to the silicon engine housing, and utilizing the engine rotor as the generator rotor. This is achieved by electroplating nickel–iron (NiFe) poles into the rotor tips. Integration of the engine and generator avoids shaft coupling between the two machines, simplifying assembly of the devices as well as improving sealing of the engine housing and reducing unwanted heat flow out of the combustion chamber. It also, however, places unique constraints on the generator design as detailed in Chapter 5.

1.3.4 Fluidic Systems

The delivery of fuel to the engine is a nontrivial problem. A precise fuel-air mixture must flow to the combustion chamber under a wide range of operating conditions. Further, the system that performs this function must use only a small fraction of the engine output power. One possibility is to use the phase eruption of fuel in a microchannel positioned to absorb waste heat from the engine. This approach is explored in [30].

1.3.5 Packaging

As the dimensions of the engine shrink, its surface area to volume ratio increases, and heat dissipates more quickly than at larger scales. In a cold engine, quenching of the combustion flame can occur at the wall of the combustion chamber, causing a loss of power. Thus, micro-scale engines need thermal insulation to maintain an appropriate temperature, unlike macro-scale engines which need to be cooled.

The generator, however, experiences a decrease in performance as temperature rises; soft magnetic permeability and saturation induction decrease, and hard magnetic residual flux density decreases. Hence a thermal package was created with the goal of insulating the engine while providing cooling for the generator. This is accomplished through the use of aerogel insulation, which surrounds the engine housing including the small gap between the housing and the generator stator. The stator, meanwhile, is mounted directly to the metal package case, which allows heat to escape to the outside.

1.4 Scope of Research and Outline

The remainder of this work concerns the design, construction and testing of electric generators at two size scales. Both of these designs are intended for application as part of an engine/generator set for use in portable power systems. Chapter 2 details the magnetic materials that can be used in constructing an electric machine. The properties of both soft and hard magnetic materials, as well as microscale fabrication methods, are discussed. Chapter 3 gives an overview of the many possible machine configurations that can be used, noting the advantages and drawbacks of each, and providing relevant information on the state of the art where possible. Chapter 4 presents the equations governing quasi-static magnetic fields, and develops the theory underlying the common methods of analysis for electromechanical devices. Chapter 5 describes the design, construction and testing of a millimeter scale generator with several unique features. Chapter 6 describes the design methodology for a centimeter scale generator and presents calculated results. Finally, Chapter 7 draws conclusions from the results of the project, and suggests future promising avenues of research.

Chapter 2

Magnetic Properties of Materials

Electromechanical energy conversion can be performed with nothing more than electrically conductive materials. Calculations of the mechanical forces experienced by two parallel conducting wires are a staple of introductory physics classes. However, the effectiveness and efficiency of motors, generators and other types of actuators can be dramatically increased by the introduction of materials with favorable magnetic properties. Much as a conductive wire confines electric fields and currents within its volume, ferromagnetic materials can confine magnetic fields and fluxes, such that they can be directed and concentrated in geometrically advantageous arrangements.

Just as every material has a conductivity (σ) that relates electric field to current density and acts as a figure of merit for application as an electrical conductor, every material also has a permeability (μ), which relates magnetic field to flux density and serves as a figure of merit for magnetic applications. Based on the magnitude of their permeability, materials can be grouped into three categories, as shown in Table 2.1. With the exception of a few engineering curiosities, only ferromagnetic materials are exploited for their magnetic properties; hence the term "magnetic materials" will be taken hereafter to refer to ferromagnetic materials, and the remainder of this chapter will focus exclusively on ferromagnetic materials and effects.

Type	Permeability Range
Ferromagnetic	$\sim 1.1 < \mu_r < \infty$
Paramagnetic	$1.0 < \mu_r < \sim 1.1$
Diamagnetic	$0 < \mu_r < 1.0$

Table 2.1: Magnetic material designations.

2.1 Material Properties

There exist a confusingly large number of variations on the definition of permeability (see, for example, [31] for 18 of them). For the sake of simplicity, we take permeability to be the ratio of the magnitudes of **B** and **H**, that is,

$$\mu = \frac{|\mathbf{B}|}{|\mathbf{H}|} \tag{2.1}$$

for **B** in Gauss and **H** in Oersteds, or

$$\mu = \mu_r \mu_o = \frac{|\mathbf{B}|}{|\mathbf{H}|} \tag{2.2}$$

for **B** in Tesla and **H** in A/m. In Eq. 2.2, μ_r is known as the "relative permeability" and μ_o is the permeability of vacuum, a constant equal to $4\pi \times 10^{-7}$. Note that for a given material, μ in Eq. 2.1 has the same value as μ_r in Eq. 2.2. Hereafter, only the SI units of Tesla and A/m will be used. Note that for ferromagnetic materials, μ_r depends strongly on the particular operating point; it is always prudent to determine how a given permeability was calculated.

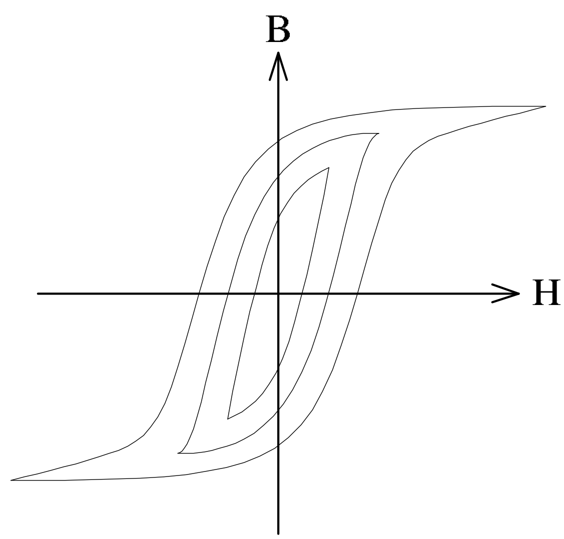

Figure 2.1: Typical family of B-H loops.

Permeability is only one of several properties that characterize a magnetic material. A more complete characterization at a given frequency is given by a family of B-H curves, as shown in Figure 2.1. Each curve represents the periodic steady-state trajectory of magnetic field and flux density in a sample of material uniformly subjected to an alternating field. The family of curves is parameterized by the applied field amplitude. Although the exact shape and extent of the curves depends on the particular material under test, all ferromagnetic materials exhibit qualitatively similar behavior — notably saturation, which is the tendency of the slope of the plot to approach μ_o (i.e. μ_r=1) at high fields, and hysteresis, which is the multivalued nature of the flux density for a given field.

The characteristic saturation and hysteresis of the ferromagnetic B-H loop are the result of the material structure, in which atomic moments tend to self-align into magnetic domains of relatively large extent (>0.1 μm [32]) in the absence of external fields. The atomic moments within a domain are aligned, giving the domain a net magnetization; however, the orientation of the magnetization from domain to domain is random, resulting on average in a zero net magnetization for a given sample of material. As the externally applied field is increased, initially domain boundaries shift so as to increase the volume of the domains whose magnetization is parallel with the applied field. This results in an increase in flux density. At higher levels of applied field, domain magnetizations rotate to align with the field, increasing the flux density further. However, at extremely high fields the great majority of domains are aligned, and further increases in field fail to increase the flux beyond the increase expected from vacuum. Thus the material saturates. The shifting of domain boundaries and rotation of the domain magnetizations requires non-reversible work to be done by the applied field. Hence the B-H loop must have a nonzero area equal to the net energy required to traverse it; this is the origin of the hysteresis effect.

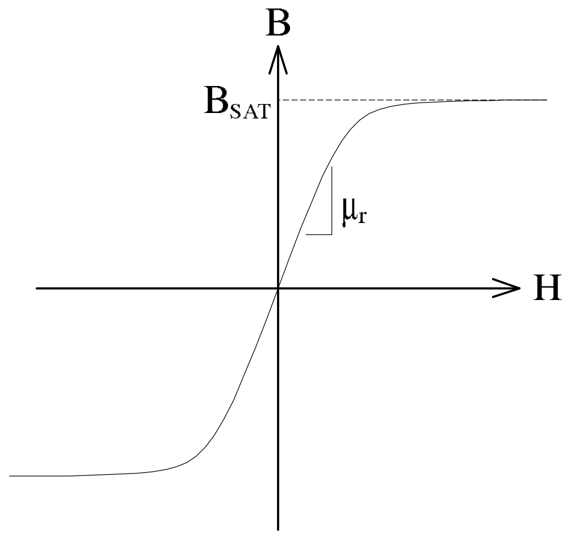

Figure 2.2: Typical B-H characteristic for soft magnetic material.

2.1.1 Soft Magnetic Materials

Soft magnetic materials are ferromagnetic materials with a narrow hysteresis characteristic of the B-H loop, as shown in Fig. 2.2. The figure illustrates two critical parameters for designing soft magnetic structures — the permeability and saturation flux density or saturation induction. Given Equations 2.1 and 2.2, the permeability appears as the slope of the plot. Saturation flux density (B_{SAT}) is the value of flux density at which the slope of the plot reaches μ_o, indicating that further field increases will result in only the incremental flux increase expected from vacuum.

The analysis of magnetic structures is covered in Chapter 4; however brief remarks on the implications of these quantities are offered here. Permeability determines the ease with which magnetic flux can be induced to flow in a material. Because most useful magnetic actuator designs incorporate an air gap with very low permeability,

permeability of a soft magnetic material is often of only secondary importance. Saturation flux density, on the other hand, places a fundamental limit on the performance of an electromechanical actuator (see Sec. 3.3.1). A low saturation value limits the amount of stored energy, and hence limits the force or torque of an actuator. Typical values for relative permeability and saturation flux density are given in Table 2.2.

Material	μ_r	B_{SAT} (Tesla)
Fe	5000	2.158
Co	245	1.787-1.875
Ni	4800	0.608
$Ni_{80}Fe_{20}$	840-7000	1.04
$Ni_{45}Fe_{55}$	3500	1.6
2.75% Si Steel	5800	2.04

Table 2.2: Properties of selected soft magnetic materials [33].

2.1.2 Hard Magnetic Materials

Permanent magnet materials, also known as “hard” magnetic materials, are those having a wide hysteresis loop, as shown in Fig. 2.3. Key parameters for hard materials are remanence (B_r) and coercivity (H_c), as indicated in the figure. Remanence is the flux density at the point on the B-H trajectory where field is zero; it is a measure of how much flux can be supplied by the magnet. Similarly, coercivity is the field at the point where flux density has been driven to zero by an external field; coercivity is a measure of how difficult it is to demagnetize a magnet. The point on the B-H loop where the product of B and H is at a maximum is called the “maximum energy product”, and is often given as a figure of merit for evaluating hard magnetic

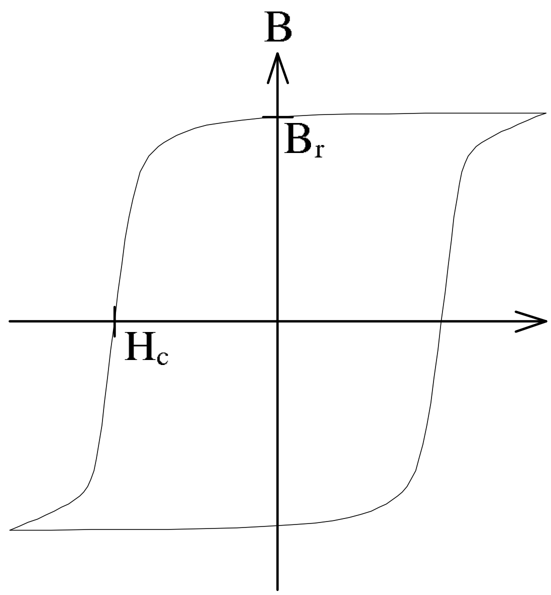

Figure 2.3: Typical B-H characteristic for hard magnetic material.

materials. Optimal designs use the magnet at or near its point of maximum energy product.

Permanent magnets are useful because of the extremely large fields they can develop in a small volume. For example, for a simple C-core with cross sectional dimensions of 1 cm by 1 cm and a 1 mm air gap, a magnet with $B_r = 0.7$ and volume of 1×10^{-6} m^3 (i.e. a cube with 1 cm sides) can provide a uniform flux density of 0.636 Tesla in the gap. A copper winding that provides the same flux density in the gap, operating with a current density of 10×10^6 A/m^2 would have a volume of approximately 2.03×10^{-6} m^3 — a factor of two increase. Note also that unlike a current-carrying conductor, the magnet does not dissipate power to provide field in the gap. (Methods for calculation of fields due to permanent magnets are covered in Chapter 4).

The magnetization of a permanent magnet is generally not intentionally changed once it is assembled into an actuator. This can be a drawback, as in applications where control over magnetic field is desired, or a useful feature, as in applications where field is desired even when external power sources are unavailable.

There are numerous types of permanent magnet material; a detailed survey is beyond the scope of this work. The most commonly commonly used materials, however, are alnico, ferrite, and the rare earth materials samarium cobalt and neodymium iron boron.

Alnico is perhaps the oldest permanent magnet material still in widespread use, having been discovered by Japanese researchers in 1931. It is capable of operating at elevated temperatures, up to 520° C [34]. Alnico has high remanence, but low coercivity, making it easy to demagnetize. Further, alnico's demagnetization curve is highly nonlinear, with the result that a freshly magnetized alnico magnet can become partially demagnetized upon removal from the magnetizing fixture. Thus to achieve the best performance, it may be necessary to magnetize alnico magnets in place, only after a magnetic structure has been assembled. A final consideration is the material's brittleness. This makes machining difficult, and increases the cost of parts that require close tolerances.

Ferrite magnets, also known as ceramic magnets, are alloys of Barium (Ba) or Strontium (Sr) with ferrite (Fe_2O_3). The materials have a linear demagnetization characteristic, and hence are easier to work with than alnico. This, and ferrites' low cost make them the most common magnets for general purpose applications.

Samarium cobalt (SmCo), along with Neodymium, falls under the heading of "rare earth" permanent magnet materials. Samarium cobalt is a high performance material, having high remanence and coercivity, and a linear demagnetization curve. It is expensive, however, owing to the high cost of the component Sm and Co.

Neodymium iron boron (NdFeB) magnets are a relatively recent development, becoming available in the early 1980s. Because Nd is more readily available than Sm, they are less expensive than SmCo. Neodymium magnets currently have the best magnetic properties at room temperature. However, the material is sensitive to high temperatures, with a maximum operating temperature of 250° C. Neodymium magnets can also corrode if proper precautions are not taken.

Table 2.3 summarizes the properties of these materials.

Material	B_r [T]	H_c [kA/m]	$(BH)_{max}$ [kJ/m^3]	Ref.
Ceramic 1	0.23	147	8.36	[35]
Ceramic 5	0.38	191	27.0	[35]
Ceramic 7	0.34	259	21.9	[35]
Ceramic 8	0.385	235	27.8	[35]
Ceramic 10	0.41	223	31.8	[35]
Alnico 2*	0.71	43.8	11.9	[35]
Alnico 5*	1.05	47.8	24	[35]
Alnico 6*	0.94	62.9	23	[35]
Alnico 8*	0.76	119	36	[35]
Alnico 2**	0.75	44.6	13.5	[35]
Alnico 5**	1.24	50.9	43.8	[35]
Alnico 6**	1.5	62.1	31.0	[35]
Alnico 8**	0.82	131.3	42.2	[35]
$SmCo_5$	0.83	600	128	[35]
Sm_2Co_{17}	1.0	480	192	[35]
$SmCo_5^\dagger$	0.65	460	80	[35]
$Sm_2Co_{17}^\dagger$	0.86	497	130	[35]
NdFeB (MQ I)	0.61	424	64	[35]
NdFeB (MQ II)	0.80	520	104	[35]
NdFeB (MQ III)	1.18	840	256	[35]
Alnico 2	0.73	44.6	13.6	[33]
Alnico 5	1.25	45.8	36	[33]
Alnico 12	0.58	75.8	—	[33]
PtCo	0.45	207	—	[33]
$Sm_2Co_{17}^{*\ddagger}$	1.05-1.12	600-730	200-240	[34]
NdFeB$^{*\sharp}$	1.29-1.35	980-1040	315-350	[34]

* Sintered ** Cast † Bonded ‡ Vacomax 240 HR
$^\sharp$ Vacodym 633 HR

Table 2.3: Properties of selected hard magnetic materials.

2.2 Temperature Effects

All ferromagnetic materials experience a drop in saturation flux density as temperature increases. This drop is gradual at first, becomes steep at higher temperatures, and levels off again as the value approaches zero. The Curie point, or Curie temperature, is the extrapolation of the steep part of the curve to zero saturation. Above this temperature, saturation is effectively, if not identically, zero. Physically, when temperature is below the Curie point, fields resulting from atomic moments cause an ordered domain structure; above the Curie point thermal effects dominate, pushing the structure towards disorder [32]. Table 2.4 gives Curie points for some common soft magnetic materials.

Material	Curie Point (°C)	Ref.
Fe	770	[33]
Co	1130	[33]
Ni	358	[33]
$Ni_{80}Fe_{20}$	560†	[33]
$Ni_{50}Fe_{50}$	530†	[33]
2.75% Si Steel	760†	[33]
Alnico 5*	900	[35]
Ceramic 10	450	[35]
Sm_2Co_{17}	750	[35]
NdFeB (MQIII)	312	[35]

* Sintered † Approximate

Table 2.4: Curie point of selected magnetic materials.

2.3 Frequency Effects

The design of magnetic structures is treated extensively in Chapter 4. However, the skin depth, a measure of the depth of penetration of an AC magnetic field, and core loss, energy dissipated by AC fields, both depend on material properties as well as operating point. Hence they appropriately fit into a discussion of material properties, but must be considered in the context of design.

2.3.1 Skin Effect at High Frequency

The skin effect, with reference to magnetic fields, describes the tendency of alternating magnetic fields in soft magnetic materials to achieve maximum value at the surface of an object, while decreasing in amplitude towards the center. The layer of high flux density forms a "skin" on the object. The skin effect is the result of circulating eddy currents, which tend to cancel some of the field. In practice, if the skin depth of a material at the desired operating frequency is smaller than the thickness of the structure, quasi-static calculations will overestimate the amount of flux carried in the core. The skin depth is given by

$$s = \sqrt{\frac{2\rho}{\mu_r \mu_o \omega}} \tag{2.3}$$

where s has units of meters, ρ has units of $\Omega{\cdot}$m, μ_r is the unitless relative permeability, μ_o=$4\pi\times10^{-7}$ is the permeability of vacuum, and ω has units of $\frac{\text{rad}}{\text{sec}}$. Thus for pure iron ($\mu_r$=5000, ρ=97×10^{-9} Ω·m) at 500 Hz (ω=3142 $\frac{\text{rad}}{\text{sec}}$), Eq. 2.3 gives

$$s = \sqrt{\frac{2 \cdot 97\times10^{-9}}{5000 \cdot 4\pi\times10^{-7} \cdot 3142}} \cong 100\times10^{-6} \text{ m} \tag{2.4}$$

Table 2.5 gives skin depths for some common soft magnetic materials.

2.3.2 Losses in Soft Magnetic Materials

The primary sources of loss in soft magnetic materials are eddy current loss, due to circulating currents in the material associated with time-varying flux density, and hysteresis loss, which is the non-reversible energy needed to shift domain boundaries and rotate the individual domain magnetization vectors. In addition, there exist "anomalous losses", which are seen in practice but not predicted by the other loss mechanisms; the source of these losses is not well understood.

A simple loss model is given by Equation 2.5. The core loss density (P'_{core}) is given in W/m^3. Note that eddy current losses alone would predict loss proportional to f^2B^2, while hysteresis loss can be approximated as proportional to fB^2 [36]. Thus reasonable choices for a and b might be 2 and 1.5, respectively.

$$P'_{core} = KB^a f^b \tag{2.5}$$

Material	μ_r	ρ (Ω·m)	Skin Depth (μm)
Fe	5000	97×10^{-9}	100
Co	245	62×10^{-9}	358
Ni	4800	68×10^{-9}	85

Table 2.5: Skin depths of selected materials at 500 Hz.

Several measures can be taken to mitigate core loss. From a design standpoint, lower flux densities and lower frequencies should be used when feasible. Materials having higher resistivities, such as ferrites, can reduce eddy current losses, while those with narrow B-H loops can reduce hysteresis loss. Finally, composite materials can be fashioned such that electrical insulation introduced into the magnetic structure limits eddy current losses. Such low-loss materials include silicon-iron alloy (silicon steel) formed into thin laminated layers, powdered iron (also known as SMC or soft magnetic composite).

$$P'_{core} = \frac{Kf}{\frac{a}{B^3} + \frac{b}{B^{2.3}} + \frac{c}{B^{1.65}}} + df^2B^2 \tag{2.6}$$

Figure 2.4 shows core loss densities for silicon steel laminations and powdered iron. The plot for silicon steel was made by fitting Eq. 2.5 to manufacturer data [37]; the resulting constants were K=24.6, a=1.78 and b=1.35. The manufacturer loss expression for the powdered iron is given by Eq. 2.6, where K=1×10^3, a=1×10^{-3}, b=69.4×10^{-3}, c=477×10^{-3} and d=19×10^{-3} [38]. In this case the silicon steel shows lower losses than powdered iron by about a factor of 10.

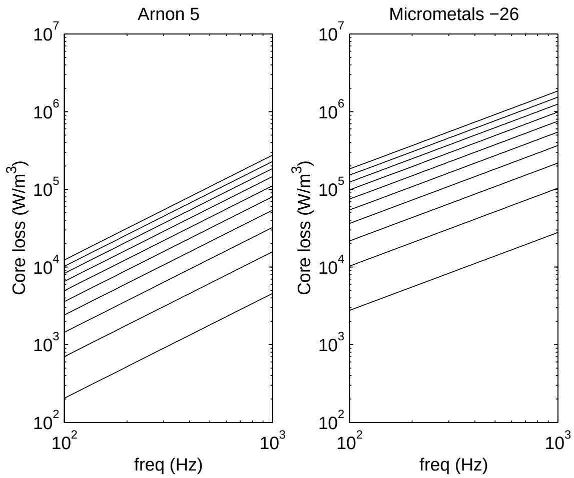

Figure 2.4: Core loss density for Arnon 5 silicon steel laminations (a), and Micrometals -26 powdered iron (b).

2.4 Magnetic Materials in MEMS

It should be noted that not all the material options presented in Sections 2.1.1 and 2.1.2 have been successfully implemented at the microscale. The field of magnetic materials for MEMS continues to be explored.

2.4.1 Fabrication Techniques

Presented below is a brief summary of MEMS fabrication techniques, as found in [39].

Electrodeposition Electroplating is also known as electrodeposition or electroforming. The process has been used since the 1800's to deposit metals on conductive surfaces. Electroplating is carried out in a bath of electrolyte, in which the plating material (anode) and object to be plated (cathode) are submerged.

An electrical current carries ions from the anode to the cathode, creating a conformal coating. If specific shapes are desired for the deposited structures, electroplating can be performed in conjunction with a mold.

Sputtering Sputtering is often used for the deposition of metal films, although it is also suitable for amorphous silicon, glass and piezoelectric materials. Although there are several variations, the essential mechanism is the firing of ions at a target made from the desired deposition material. Particles displaced from the target are guided towards the wafer by electric and/or magnetic fields. Sputtering gives good conformality (uniform feature coverage), and can be performed at relatively low temperatures. A drawback is high stress in deposited films, and difficulty of precisely controlling film stress.

Evaporation Evaporation is another thin-film deposition technique, in which a target is heated with an electrical current or electron beam. Vaporized target material then condenses on the wafer. This is a directional process, which can result in "shadowing" effects if the wafer is not rotated.

LIGA LIGA is a multistep process that combines lithography, plating and molding (hence the German acronym Lithographie, Galvanoformung und Abformung). Relatively thick, high aspect ratio metal structures can be formed with this process. X-ray lithography is used, which makes LIGA expensive and somewhat inconvenient.

Other Techniques Various other techniques such as screen printing and molding can also be employed.

2.4.2 Soft Magnetic Materials for MEMS

NiFe Nickel-iron (sometimes called Permalloy in its 80:20 alloy) is a popular soft magnetic material for MEMS. It is easy to deposit, has high permeabiliy, high saturation flux density, low hysteresis, low magnetostriction, and in the alloy ratio of 36:64 has a coefficient of thermal expansion approximately equal to that of silicon. There is a large body of literature on NiFe MEMS. Recent work includes: [28], in which a 50:50 nickel:iron ratio alloy was electroplated into deep silicon molds; [40], describing an electroplating process for vertically laminated NiFe structures; and [41] investigating both sputtering and electroplating of NiFe.

NiFeMo Nickel-iron-molybdenum alloy has been explored as an alternative to NiFe. The addition of molybdenum to nickel-iron alloy increases both resistivity and initial permeability, and allows for simpler heat treatment [33]. It has been shown that NiFeMo alloy can be deposited by electroplating; saturation flux densities as high as 1.07 T, and relative permeabilities up to 7000 have been reported [42]. Gas flow sputtering has also been used to deposit NiFeMo in films up to 15 μm thick [41].

CoFe- and CoNi- Alloys A large body of literature exists detailing magnetic materials that find application in the magnetic recording and data storage industry. Although few MEMS applications have been reported, these alloys are nonetheless potential candidates for sensors and actuators: CoFeB; CoFeCr; CoFeP; CoFeCu; CoNiFe; CoNiFeS; CoFeNiCr; CoFeSnP; and CoNiFeB [43].

2.4.3 Hard Magnetic Materials for MEMS

$Sr\text{-}Fe_{12}O_{19}$ Strontium-ferrite (commonly known as “ferrite” or “ceramic”) magnets have been made by mixing $Sr\text{-}Fe_{12}O_{19}$ powder with an epoxy resin binding agent, and spreading the resulting paste into photoresist molds. Completed cylindrical magnets, 65 μm thick and ranging in diameter from 50 to 200 μm, showed coercivity of 356 kA/m and maximum energy product of 2.7 kJ/m^3 [44]. A similar approach, mixing $Sr\text{-}Fe_{12}O_{19}$ powder with epoxy, but utilizing screen printing for deposition, achieved intrinsic coercivity of 320 kA/m and residual induction of 60 mT [45].

CoNiMnP Cobalt-Nickel-Manganese-Phosphorus can be deposited via electroplating. In [46], electroplating was performed in the presence of a DC magnetic field, improving the magnets’ coercivity, rententivity and energy product, which were 87.6 kA/m, 0.19 T and 2.3 kJ/m^3, respectively for 18-20 μm thick structures.

NdFeB Neodymium-iron-boron, as described in Section 2.1.2, is the permanent magnet material of choice for applications that are not cost or temperature constrained. Relatively thick films (up to 800 μm) of NdFeB have been formed via tape casting, as described in [47]. Measured values of 885 mT and 760 kA/m are reported for remanent flux density and intrinsic coercivity, respectively. Cured tapes were successfully magnetized with multipole patterns having a 1 mm pole pitch.

SmCo Deposition of samarium cobalt permanent magnets is reported in [41]. The process reported requires an annealing step at relatively high temperature ($> 500\,^{\circ}$C), and hence sputtered SmCo may be difficult to incorporate into some structures. The authors also note that while thicknesses up to 50 μm are possible on ceramic and glass substrates, films on silicon are limited to 3 μm due to delamination during annealing. The same researchers, in [48], report coercivity of 800 kA/m, retentivity of 0.5 T and energy product of 20 kJ/m^3 for sputtered SmCo measured in the in-plane direction.

CoPt and FePt Alloys Although not widely used for MEMS applications, CoPt, FePt and their alloys appear in the magnetic materials literature as candidates for microscale permanent magnets. Sputtered FePt is reported in [49] with in-plane coercivity and energy product of 637 kA/m and 126 kJ/m^3, respectively, while electroplated CoPtW(P) and CoPtZn(P) having coercivity as high as 300 kA/m are reported in [50].

Chapter 3

Electric Machine Technology

This chapter attempts to provide an overview of electric machine technology. By necessity the treatment is superficial and incomplete. It is worthwhile however, considering the nature of the reported research. The goal of the chapter is to document technologies that are appropriate for portable electric power generation, and provide information on the state of the art. In addition to serving as a basis for evaluation of the designs presented in Chapters 5 and 6, this chapter may also be useful as a reference for the reader interested in selecting small electric motors or generators. Many of the concepts here are extremely basic for the reader familiar with electric machines. However, the information is included to aid in defining terms used throughout this work, and to make the work accessible to as wide an audience as possible. While reference will be made to basic results concerning the analysis of electromechanical devices, detailed analysis is left for Chapter 4.

The focus here is on machines that may be considered for portable applications. DC machines are neglected due to their poor reliability. Further, only rotary machines and primarily electromagnetic actuation are considered; machines making use of electric fields make an appearance only at the micro scale. The first section introduces the various means by which torque can be developed from magnetic and electric fields. The second section presents different rotary machine configurations that can make use of these torque-producing effects. The third section gives a scaling analysis along with design implications for small-scale machines. The last section gives relevant data on existing macro-scale and micro-scale machines, including commercial devices as well as state of the art research examples.

3.1 Electric Machine Types

3.1.1 Reluctance

Reluctance is the simplest electromagnetic mechanism for producing a torque. Reluctance forces are those that attract soft magnetic materials to a magnetic field. Typically, a reluctance machine consists of a soft magnetic stator with wound conductors, and a soft magnetic rotor. The rotor must have either saliency (non-uniform shape) or anisotropy (non-uniform permeability), while the stator may be uniform, salient, or anisotropic. When a winding is energized, torque acts to minimize the reluctance of the magnetic circuit formed by the rotor and stator. By energizing multiple windings in sequence, the rotor can be made to turn.

Several types of machine depend on reluctance effects to develop torque: synchronous reluctance machines (SRMs); switched reluctance, variable reluctance or "stepper" motors. The advantages of the reluctance machine are its robust construction, low cost, precise positioning capability, and ability to hold a static position.

3.1.2 Electromagnetic Induction

Induction machines typically have a soft magnetic stator and rotor separated by a uniform air gap, a wound stator, and windings or other conductive material (e.g. copper bars) in the rotor. Because the stator and rotor are coupled magnetically, AC currents in the stator will excite currents in the rotor, much like in a transformer. The interaction of the magnetic fluxes resulting from rotor and stator currents produces torque. However, should the rotor speed rise to become synchronous with the stator electrical frequency, the frequency of the stator excitation relative to the rotor is zero, no current is excited in the rotor, and the machine loses torque. Thus induction machines are inherently asynchronous — the rotor does not move in lock-step with the stator frequency.

Induction machines are the most commonly used in industrial settings and in home appliances because of their simplicity of operation and low cost. Because they are open loop stable with a wide range of attraction, no sensors or closed-loop controls are needed to run the machine for simple line-connected applications like fans and pumps. And because the machine can start up and run from AC line power, no semiconductor elements are needed for these applications. Induction machines are less common in small-scale and portable applications, where power density is critical.

3.1.3 Permanent Magnet

As the name implies, permanent magnet machines employ hard magnetic materials, usually in the rotor. The interaction of the stator windings with the field produced by the magnets gives rise to torque. Permanent magnet machines typically have higher specific torque, specific power and efficiency than other types of machines because of the high field provided by the magnets. Recall the example given in Section 2.1.2; compared to a winding providing the same field, permanent magnet excitation requires less volume and mass, and does not carry the penalty of resistive power loss.

Permanent magnet machines fall into two main categories: permanent magnet synchronous machines (PMSM); and brushless DC (BLDC). PMSMs are excited by sinusoidal voltages, and often operate without direct sensing of position. BLDC machines are excited by square-wave voltages, and feature electronic commutation, in which feedback from position sensors (often hall effect sensors) determines the correct phase excitation to be supplied by the inverter. Note that BLDC machines are not true DC machines, but only appear so to the end user because they are packaged with sensors and drive electronics that perform the function of traditional mechanical brushes.

Type	Self exciting	Holding torque	Synchronous	Torque
Reluctance	No	Yes	Yes	Low
Induction	No	No	No	Moderate
Permanent Magnet	Yes	Yes	Yes	High

Table 3.1: Comparison of electric machine technologies.

3.1.4 Electrostatic

Due to both practical and fundamental limitations, electrostatic machines are not competitive at the macro-scale. However, at extremely small size scales the technology begins to look more attactive, as explained in Sec. 3.3.1. Thus many MEMS devices utilize electrostatic actuation. Such devices will not be discussed in this work; the reader is directed to the copious literature on MEMS actuators.

3.2 Electric Machine Configurations

3.2.1 Radial

Radial flux machines are those in which the rotor, air gap, and stator are concentric cylinders; flux crosses the air gap in the radial direction, perpendicular to the rotor's axis of rotation, as shown in Fig. 3.1. The overwhelming majority of electric machines have a radial flux configuration. The popularity of radial flux machines is due to their

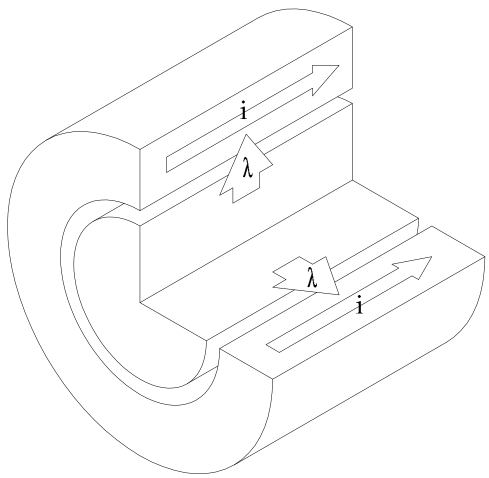

Figure 3.1: Radial flux machine configuration.

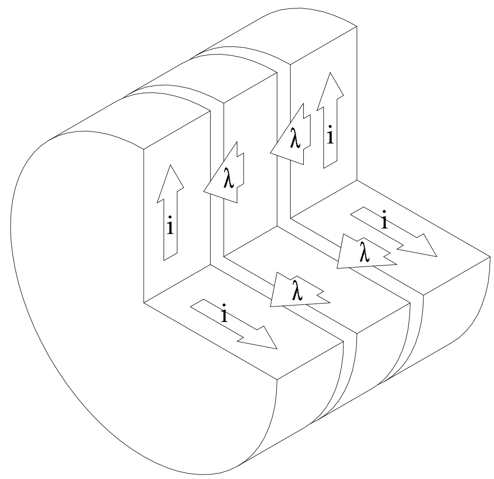

Figure 3.2: Axial flux machine configuration.

ease of construction. Windings are oriented axially, and hence can have a uniform cross-section, while soft magnetic portions of the machine can be made from stacked laminations of silicon steel with excellent magnetic properties. An additional benefit is ease of analysis - the machine can be accurately modeled by a two-dimensional cross-section taken perpendicular to the axis or rotation.

3.2.2 Axial

In the axial flux configuration, the rotor, air gap and stator are stacked discs; flux crosses the air gap parallel to the rotor's axis of rotation, as in Fig. 3.2. Axial flux machines are acknowledged to achieve higher torque densities, at the expense of more complex construction [51, 52, 53]. An approximate two-dimensional model can be drawn by taking a circumferential cross section. However, because the dimensions of the model depend on the particular radius chosen for the cross-section, the model is not exact.

3.2.3 Transverse

Transverse flux machines (TFMs) are currently the subject of much research; however they are rarely found outside of the laboratory. A TFM is shown in Fig. 3.3, although there are a number of different design variations that can properly be termed "transverse flux machines". TFMs are characterized by concentrated windings that are oriented circumferentially, and stator iron that directs flux radially across the gap and axially through the stator. Benefits of this configuration include simple windings with no end turns, and the possibility of higher specific torque. However, the construction tends to be more complex than conventional radial flux machines, and the power factor can be low due to the high winding inductance [54].

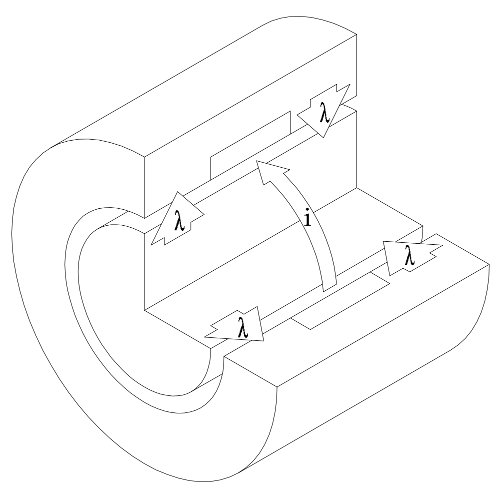

Figure 3.3: Transverse flux machine configuration

.

3.3 Scaling of Electromechanical Actuators

3.3.1 Fundamental Limits

There are fundamental limits to the amount of force or torque an electromagnetic or electrostatic actuator can produce. As described in Chapter 4, force is developed when the amount of stored energy in an electric or magnetic field changes with actuator displacement. Thus, in general, higher field intensities translate into larger absolute changes in stored energy, and larger forces. The majority of energy storage takes place in the gap (usually filled with air) that separates the stationary and moving portions of the actuator. So the highest field that can be established in an air gap is a good figure of merit for the actuator.

For electrostatic actuators, the limitation on electric field is the electrostatic breakdown of the medium in the gap. When the field in the gap is too high (i.e. the voltage across the gap is too high), a plasma arc will form, transferring all the charge from high to low potential. With the field discharged, the actuator cannot produce force. The field at which the arc forms depends on the medium as well as on pressure. The empirical relation between electrostatic breakdown voltage and gap length is known as the Paschen curve, shown in Fig. 3.4. It should be noted that to achieve the limits of the Paschen curve, surfaces with high smoothness are required. Sharp points or defects on the surface can cause localized field concentrations that cause breakdown before the field limit is reached throughout the volume of the gap.

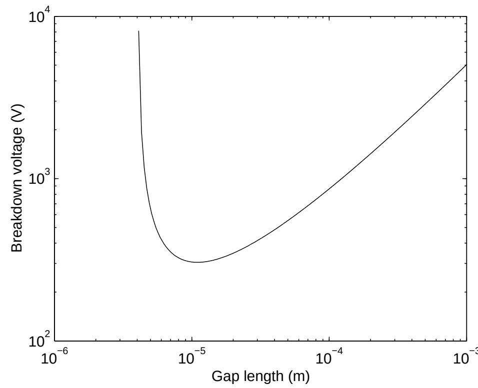

Figure 3.4: Paschen's curve for electrostatic breakdown [55].

For magnetic actuators employing soft magnetic material, a practical limit on magnetic flux density is determined by the material's saturation level. As shown in Table 2.2, the highest achievable saturation is for pure iron, at about 2.2 Tesla. In practice, pure iron is not a practical material to work with, and high AC flux densities can result in excessive power loss with the associated poor efficiency and problems with heat dissipation. Hence practical flux densities reach up to perhaps 1.5 Tesla.

Given these limits, a comparison can be made between electric and magnetic fields, as in [56],[55]. It can be shown that as gap lengths get smaller, electrostatic actuation begins to look more attractive. However, the analysis requires several assumptions, and hence the crossover point can vary over a wide range. The references above, for example, calculate various crossover points anywhere between 160 nm and 5 μm, depending on assumptions.

3.3.2 Scaling of Electromagnetic Machines

The two critical specifications for an electric motor or generator in portable applications are specific power (i.e. power per mass), and efficiency. A machine with high specific power contributes less mass to the application for a given power level, allowing greater portability, greater functionality, or more energy storage (i.e. the saved mass can be replaced by batteries, capacitors, or fuel). A high efficiency machine increases run time for a given level of energy storage.

On the macro-scale, electric machines are often designed with specific power, efficiency, or a trade-off between the two in mind. Below, the effects of scaling down a machine and their implications for design are examined. First some key quantities are defined.

- **Torque**: The torque (τ) produced by a rotary electromagnetic actuator is proportional to the product of the current (i) in the windings and the magnetic flux (λ) linking those windings.

$$\tau \propto \lambda i \tag{3.1}$$

- **Power**: Both electrical power (P_e) and mechanical power (P_m) can be defined as measures of energy transfer per time.

$$P_e = vi \tag{3.2}$$

$$P_m = \tau\omega \tag{3.3}$$

Here v indicates voltage and ω indicates angular speed of the shaft. Note that voltage is given by the time derivative of flux. Thus for a two-pole machine

$$v = \frac{d}{dt}\lambda = \omega\lambda. \tag{3.4}$$

Substituting Eqs. 3.1 and 3.4 into Eq. 3.3, we see that for an ideal machine with no losses, the average values of electrical and mechanical power are identical.

- **Losses**: There are three main sources of loss in electric machines: copper loss (P_{Cu}); iron loss (P_{Fe}); and frictional loss (P_{fr}). Copper loss is simply power dissipated by the resistance (R) of the windings

$$P_{Cu} = i^2 R. \tag{3.5}$$

Iron loss, sometimes called core loss, is the result of time-varying magnetic fields in the ferromagnetic materials that are used to constrain the flux in most motors. Iron loss has a component due to eddy currents in the material, and a component due to the hysteresis characteristic of the material's BH loop. Expressions for iron loss are usually obtained by fitting a curve to experimental data, and are often quite complex (see Section 2.3.2 and Appendix B). For the purposes of the scaling argument below however, core loss will be approximated by

$$P_{Fe} \propto \omega B^2 \cdot volume. \tag{3.6}$$

- **Efficiency**: The efficiency (η) of a machine is given by the fraction of input power remaining after losses are subtracted. In motoring operation this implies

$$\eta_{mot} = \frac{P_{mech}}{P_{elec}} \tag{3.7}$$

while in generator operation

$$\eta_{gen} = \frac{P_{elec}}{P_{mech}}. \tag{3.8}$$

A scaling analysis proceeds from a thought experiment which begins with a macro-size electric motor, and scales it down by a factor s $(0 < s < 1)$ along each of the three spatial dimensions, while holding the flux density (B), current density (J) and speed (ω) constant.

Because $\lambda = B \cdot area$ and $i = J \cdot area$, it can be seen from Eqs. 3.1 and 3.3 that torque and power are both proportional to s^4:

$$\tau \propto BJs^4 \tag{3.9}$$

$$P \propto \omega BJs^4 \tag{3.10}$$

The resistance of the motor windings is given by $R = \sigma\frac{length}{area}$, and substituting into Eq. 3.5 gives

$$P_{Cu} \propto \sigma J^2 s^3. \tag{3.11}$$

From Eq. 5.3, iron loss is also proportional to volume:

$$P_{Fe} \propto \omega B^2 s^3. \tag{3.12}$$

Thus it can be seen that as s decreases, torque and power decrease rapidly. Furthermore, power density drops linearly

$$\frac{P}{volume} \propto \omega BJs \tag{3.13}$$

and efficiency drops as well

$$\eta \propto 1 - \frac{\sigma J}{\omega Bs} - \frac{B}{Js}. \tag{3.14}$$

3.3.3 Scaling Strategies

To maintain the levels of power density and efficiency associated with the macro-scale as a machine is scaled down, scaling up of J and ω is warranted; B in most designs is close to material saturation limits, and hence it is not reasonable to expect that it can be scaled. Note that the thermal dissipation ability of windings is increased as surface area becomes large relative to volume, and lower centrifugal forces and higher mechanical resonances at small scale allow higher speeds.

A possible plan is to attempt to keep efficiency constant, by scaling $J \propto \frac{1}{s}$ and $\omega \propto \frac{1}{s^2}$, while holding B constant. Under this "constant efficiency" scheme, power decreases only linearly, and specific power actually increases. Of course, as s becomes very small, limitations arise from the viscous losses of the high-speed rotor as well as higher order terms in the copper and iron loss.

3.4 Survey of Small Electric Machines

3.4.1 Macro-Scale Machines

A wide array of small machines exists for power levels in the tens to hundreds of Watts. Rather than attempt to document this vast space, Tab. 3.2 is offered to give a representative sample of high-performance permanent magnet machines. These machines utilize high energy product magnets, and hence achieve impressive specific power and power density. Further, the brushless design is low maintenance and environmentally rugged. Any small machine proposed for portable power must be measured against these machines.

3.4.2 Microfabricated Machines

Tiny rotational electric machines making use of microfabrication technology have been described in the literature since at least the late 1980's (see for example [59]). For reasons explained in Section 3.3.1, the majority of these designs utilize electrostatic forces for actuation. A review of such devices is beyond the scope of this work. However, MEMS rotational actuators based on electromagnetic forces also appear in the literature, and this section attempts to summarize a representative sample of these.

Some of the earliest work is presented in [60], [61], [62]. The first paper describes a two-pole, two-phase reluctance machine with a 400 μm diameter rotor that reached

Model	Manuf.	Power W	Max. Speed krpm	Max. Eff. %	Length mm	Dia. mm	Mass g	Volume m^3	Spec. Power W/kg	Power Dens. W/m^3
EC16	Maxon	40.0	50	84.3	57.2	16.0	58.0	1.15E-05	689.7	3.48E+06
602006B	Faulhaber	1.6	100	57.0	21.9	6.0	2.5	6.19E-07	624.0	2.52E+06
EC22	Maxon	50.0	50	88.0	63.7	22.0	130.0	2.42E-05	384.6	2.07E+06
EC 6	Maxon	1.2	100	50.0	21.5	6.0	2.8	6.08E-07	428.6	1.98E+06
EC16	Maxon	15.0	50	68.1	41.2	16.0	34.0	8.28E-06	441.2	1.81E+06
2444024B	Faulhaber	36.0	38	77.0	45.0	24.0	100.0	2.03E-05	360.0	1.77E+06
3564012B	Faulhaber	109.0	27	81.0	65.4	35.0	310.0	6.29E-05	351.6	1.73E+06
1628012B	Faulhaber	10.0	65	68.0	29.0	16.0	31.0	5.83E-06	322.6	1.72E+06
2036012B	Faulhaber	20.0	49	70.0	37.0	20.0	50.0	1.16E-05	400.0	1.72E+06
EC32	Maxon	80.0	25	77.0	61.1	32.0	263.0	4.91E-05	304.2	1.63E+06
EC45 Flat	Maxon	50.0	10	82.7	21.3	42.8	110.0	3.06E-05	454.6	1.63E+06
4490024B	Faulhaber	201.0	16	86.0	91.5	44.0	750.0	1.39E-04	268.0	1.45E+06
EC-max 22	Maxon	25.0	18	73.0	49.5	22.0	110.0	1.88E-05	227.3	1.33E+06
EC40	Maxon	120.0	18	79.0	72.6	40.0	390.0	9.12E-05	307.7	1.32E+06
EC-max 30	Maxon	40.0	15	79.0	43.2	30.0	163.0	3.05E-05	245.4	1.31E+06
EC-max 30	Maxon	60.0	15	80.0	65.2	30.0	271.0	4.61E-05	221.4	1.30E+06
EC45 Flat	Maxon	30.0	10	77.6	16.4	42.8	88.0	2.36E-05	340.9	1.27E+06
3056012B	Faulhaber	48.0	28	73.0	56.0	30.0	190.0	3.96E-05	252.6	1.21E+06
EC32 Flat	Maxon	15.0	10	64.0	15.7	32.0	58.0	1.26E-05	258.6	1.19E+06
EC22	Maxon	20.0	50	84.0	45.5	22.0	85.0	1.73E-05	235.3	1.16E+06
EC-max 16	Maxon	8.0	20	65.0	36.7	16.0	43.0	7.38E-06	186.1	1.08E+06
EC45 Flat	Maxon	12.0	10	77.4	8.2	42.8	57.0	1.18E-05	210.5	1.02E+06
EC-max 16	Maxon	5.0	20	55.0	24.7	16.0	27.0	4.96E-06	185.2	1.01E+06
EC32 Flat	Maxon	6.0	12	60.0	7.9	32.0	32.0	6.35E-06	187.5	9.45E+05
EC90 Flat	Maxon	90.0	5	86.0	27.3	90.0	648.0	1.74E-04	138.9	5.18E+05

Table 3.2: Specifications of selected off-the-shelf BLDC machines [57], [58].

8 krpm with external magnetic excitation. The second paper represents a refinement of the design, with a 3-phase variable reluctance machine having 6 stator poles and 4 rotor poles. The machine has integral windings for phase excitation as well as photodiode rotor position sensors. Designs with 423 μm and 285 μm diameter rotors achieved 12 krpm and 30 krpm, respectively. Neither of the first two papers give estimates of machine torque or power. In the third paper, the design has evolved to a 3-phase variable reluctance machine with a 50 tooth rotor which has diameter of 1 mm. It is a hybrid MEMS-macro design, using hand-assembled wound coils for excitation. The machine is coupled by a gear train to a MEMS dynamometer. A maximum speed of 8 krpm, output torque of 0.3 μNm, and mechanical output power of 20 μW are reported.

More recently, MEMS induction machines have been fabricated, as described in [63], [64], [65]. Researchers at MIT have produced a microfabricated electromagnetic induction motor with 8 mm diameter and 2 mm thickness. Experimentally demonstrated torque of this machine is 1.2 uNm, although higher values are projected from the data.

Researchers in Germany have produced a motor with 12.8 mm diameter and 1.4 mm thickness utilizing a combination of conventional techniques and microfabrication, and have demonstrated a torque constant as high as 0.4 uNm/mA [66]. Another effort there has microfabricated reluctance type linear stepper actuators with dimensions of 8 mm by 1 mm [67], [68].

Chapter 4

Analysis of Electromechanical Systems

This chapter is intended to provide the theoretical basis for the design and analysis presented in Chapters 3, 5 and 6. The chapter begins by presenting Maxwell's equations for magnetic quasi-static fields, and explaining their significance. It is then shown how, with the proper assumptions, the field equations can be rewritten to allow lumped-element analysis. The calculation of magnetic field quantities in simple structures is presented as analogous to that of electrical quantities in electrical circuits. Provided with either lumped or distributed field calculations, a simple method for the calculation of forces and torques can be derived from conservation of energy assumptions. A brief overview is given of the finite-element method for magnetic field solutions and its application to calculating forces and torques. Finally, the chapter concludes with a detailed example of the various analyses.

The chapter does not address the analysis of electromechanical systems which develop force from electrostatic fields. However, it can be shown that the analysis given here does apply to such systems with a few minor changes. The chapter also does not cover the Maxwell stress tensor, which can be used for force calculations; the method is limited to distributed field solutions, and is not used for analysis in any of the following chapters.

4.1 Maxwell's Equations

In this section, the empirical results collectively known as Maxwell's equations are presented. The treatment is superficial, serving mainly as a basis for the development of the lumped-element analysis presented in Section 4.2. For a more detailed treatment of Maxwell's equations as they relate to electromechanical interactions, the interested reader is referred to [69] or the excellent appendices in [70]. Note also that the quasi-static form of the equations is used below, in which some dynamic effects (notably the displacement current in Ampère's Law) are assumed to make vanishingly small contributions over the frequency range of interest, and hence are neglected. Throughout this chapter, $\mathbf{H}$ is magnetic field intensity, $\mathbf{B}$ is magnetic flux density, $\mathbf{J}$ is current density, $\mathbf{E}$ is electric field intensity and $\mathbf{n}$ is an outward-pointing normal vector, with boldface type indicating a vector quantity.

4.1.1 Quasi-static Magnetic Equations

Equation 4.1, also known as Ampère's Law, relates magnetic field intensity and electrical current density. Its practical implication is that a current-carrying wire acts as a source of magnetic field. The contour C of the left-hand integral encloses the surface S on the right, and hence the line integral of $\mathbf{H}$ traversing the contour is equal to the area integral of current density passing through the surface.

$$\oint_C \mathbf{H} \cdot \vec{d\ell} = \int_S \mathbf{J} \cdot \mathbf{n} \, da \tag{4.1}$$

If $\mathbf{H}$ can be constrained such that its value is constant and everywhere parallel to $\vec{d\ell}$, and the integral of the normal component of current density is defined as I, then 4.1 simplifies to

$$H\ell = I \tag{4.2}$$

where H and ℓ are scalar, and ℓ is the length of a path that encloses I.

Considering the right-hand side of Eq. 4.1, if S encloses a finite volume, Eq. 4.3 requires that the net current passing through S be zero. In other words, current flows in a closed loop — there are no point sources or sinks of current. This can be thought of as a general statement of the more familiar Kirchoff's current law (KCL).

$$\oint_S \mathbf{J} \cdot \mathbf{n} \, da = 0 \tag{4.3}$$

Equation 4.4, also called Gauss' Law, has the same form as Eq. 4.3, with magnetic flux density substituted for current density. The implication is the same — magnetic flux flows in closed loops, and Eq. 4.4 amounts to a version of KCL for magnetic flux.

$$\oint_S \mathbf{B} \cdot \mathbf{n}\ da = 0 \tag{4.4}$$

Finally, Eq. 4.5, known as Faraday's Law, describes how changing magnetic flux density induces an electric field. The time rate of change of the net flux through the surface S is equal to the line integral of electric field along the contour C, where C encloses S.

$$\oint_C \mathbf{E} \cdot \vec{d\ell} = -\frac{d}{dt} \int_S \mathbf{B} \cdot \mathbf{n}\ da \tag{4.5}$$

Equation 4.5 is often applied such that the C is coincident with a number of turns (N) of conducting wire. The electric field is thus everywhere aligned with $\vec{d\ell}$, and the integral along the length of the wire gives the voltage across the two ends:

$$V = \oint_C \mathbf{E} \cdot \vec{d\ell}. \tag{4.6}$$

Defining the flux through an open surface S as

$$\Phi = \oint_S \mathbf{B} \cdot \mathbf{n} da, \tag{4.7}$$

and flux linkage as

$$\lambda = N\Phi, \tag{4.8}$$

an expression for the voltage measured across the ends of the wire can be found by substituting Eqs. 4.6-4.8 into 4.5:

$$V = -\frac{d}{dt}\lambda. \tag{4.9}$$

4.2 Magnetic Circuit Analysis

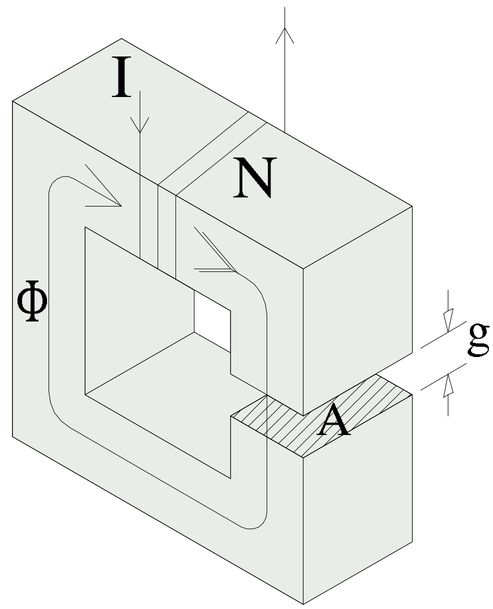

Figure 4.1: A simple magnetic circuit.

Condsider Fig. 4.1. A high permeability core of uniform cross-section A is wound with N turns of wire. The wire carries a constant current I, which produces a flux Φ in the core. A gap in the core has length g.

Along any contour that links the wires, Eq. 4.1 states that the line integral of $\mathbf{H}$ will be equal to the net enclosed current, in this case NI. In particular, if the contour is chosen to coincide with the core such that it is everywhere parallel to $\mathbf{H}$, Eq. 4.2 applies and H is treated as a scalar. From Eq. 4.4, the same flux passes through both core and gap, and by assumption is evenly distributed over the area. Recall from Eq. 2.1 that

$$B = \mu_o \mu_r H. \tag{4.10}$$

Assuming permeability of $\mu_{r,air} = 1$ in the gap, it must be that inside the core H is lower than in the gap by a factor of $\mu_{r,core}$. Thus for a sufficiently high permeability core, H is negligible everywhere except the gap, and from Eq. 4.2 the value of H in the gap must be

$$H = \frac{NI}{g} \tag{4.11}$$

Substituting 4.11 into 4.10 gives

$$B = \frac{\mu_o}{g} NI, \tag{4.12}$$

where μ_r has been suppressed. Multiplying 4.12 on both sides by the area A and applying 4.7 gives

$$\Phi = \frac{\mu A}{g} NI. \tag{4.13}$$

Finally, rearranging terms gives

$$NI = \left(\frac{g}{\mu_o A} \right) \Phi. \tag{4.14}$$

Comparison of Eqs. 4.3 and 4.4 suggests that in an analogy between the magnetic and electrical domains, magnetic flux is the counterpart to electric current. Further, note that the term in parentheses in Eq. 4.14 has the same form as the expression for the resistance of a bulk material. This new quantity is defined as "reluctance"

$$R = \frac{\ell}{\mu A}. \tag{4.15}$$

The term NI is analogous to voltage, and "magnetomotive force" (MMF) is defined as the counterpart to electromotive force (i.e. voltage). Hence

$$NI = R\Phi, \tag{4.16}$$

Relation	Electrical Circuit	Magnetic Circuit
Across variable	$V = E\ell$	$NI = H\ell$
Through variable	$I = JA$	$\Phi = BA$
Component	$R = \frac{\ell}{\sigma A}$	$R = \frac{\ell}{\mu A}$
"Ohm's Law"	$V = IR$	$NI = \Phi R$

Table 4.1: Comparison of electric and magnetic circuit quantities.

giving a magnetic analogy to Ohm's law. This electrical circuit analogy is summarized in Table 4.1.

4.3 Energy Method Analysis

The energy method is a powerful analysis tool for calculating forces or torques produced by stationary and slowly varying magnetic fields. The method applies equally well to electrostatic fields, but the focus here will be on the magnetic development. The method is relatively easy to use, and is entirely appropriate for hand calculations with lumped-element systems. However, it can also be applied to distributed field problems, and is often used in conjunction with finite-element analysis (FEA) as described in Section 4.4. The discussion here draws from similar analyses found in [36] and [70].

The basis for the energy method analysis is a simple conservation of energy. A high-level description of an electromechanical actuator is a two-port "black box", as shown in Fig. 4.2. One terminal is associated with the flow of electrical energy, and has flux linkage as the across variable and current as the through variable. The

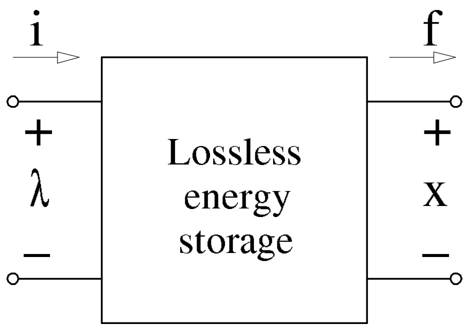

Figure 4.2: Conceptual electromechanical actuator [36].

other terminal is associated with the flow of mechanical energy, and may use either linear displacement and force, or angular displacement and torque, as the across and through variables, respectively. Inside the box is a lossless energy storage medium (i.e. a slowly-varying magnetic field). The energy balance proceeds as follows: if the excitation of one port is held constant, any change in the energy stored in the box will result in net work being done at the terminal that is allowed to vary. Thus by calculating the energy stored in a magnetic field and differentiating under the proper conditions, force or torque can be calculated. This explanation is formalized in Section 4.3.1.

4.3.1 Calculations Using the Energy Method

Assume that the system shown in Fig. 4.2 is initially at rest (i.e. the electrical and mechanical excitations are zero), and there is no energy stored inside the box. Now imagine that the mechanical terminal is fixed so as to have zero displacement, and the electrical terminal is energized with constant electrical power for an incremental time period dt. Since no mechanical work was done in this time, all of the energy supplied to the terminal must have been stored inside the box. Thus an incremental change in stored energy due to electrical excitation is given by

$$dW_e = vidt, \tag{4.17}$$

and substituting in Eq. 4.9 gives

$$dW_e = (\frac{d\lambda}{dt})idt = id\lambda. \tag{4.18}$$

If λ is then held constant, and power fu (where f is force and u is velocity) is applied to the mechanical terminal for incremental time dt, a similar incremental change in stored energy will result. Noting that $u = \frac{dx}{dt}$, the incremental change in stored energy due to mechanical excitation is

$$dW_m = -fudt = -f(\frac{dx}{dt})dt = -fdx. \tag{4.19}$$

The total incremental change in stored energy is thus the sum of the electrical and mechanical contributions,

$$dW = id\lambda - fdx. \tag{4.20}$$

and total energy stored in the system for a given operating point (λ_o,x_o) is given by the integral

$$W = \int_{(0,0)}^{(\lambda_o,x_o)} i(\lambda, x)d\lambda - f(\lambda, x)dx, \tag{4.21}$$

where notation has changed slightly to indicate explicitly that i and f are functions of λ and x.

Because the energy storage inside the black box is specified to be lossless, the function W is uniquely defined for (λ, x) — i.e. W is a state, or potential, function. Hence the value of W in Eq. 4.21 does not depend on the integration path between the points (0,0) and (λ_o,x_o). For mathematical simplicity, a convenient choice is a path with two legs: zero flux linkage from x=0 to x=x_o, implying zero force, and constant displacement from λ=0 to λ=λ_o:

$$W(\lambda_o, x_o) = \int_0^{x_o} i(0,x)d\lambda - f(0,x)dx + \int_0^{\lambda_o} i(\lambda, x_o)d\lambda - f(\lambda, x_o)dx. \tag{4.22}$$

Equation 4.22 can be interpreted as a zero force displacement (which contributes no stored energy), followed by an increase in flux with displacement held constant (which contributes energy from the electrical terminals only). Hence the first integral in Eq. 4.22 drops out entirely, and the second consists only of electrical quantities. Thus

$$W(\lambda_o, x_o) = \int_0^{\lambda_o} i(\lambda, x_o)d\lambda. \tag{4.23}$$

Finally, note that an incremental change in energy can be written as

$$dW(\lambda, x) = \left.\frac{\partial W}{\partial \lambda}\right|_{x=const} d\lambda + \left.\frac{\partial W}{\partial x}\right|_{\lambda=const} dx, \tag{4.24}$$

where it is critical that each partial derivative be taken with the other variable held constant. Comparing Eqs. 4.20 and 4.24, it is clear that

$$i = \left.\frac{\partial W}{\partial \lambda}\right|_{x=const} \tag{4.25}$$

$$f = -\left.\frac{\partial W}{\partial x}\right|_{\lambda=const}. \tag{4.26}$$

Using Eq. 4.26, force can be determined from a change in stored energy.

4.3.2 Energy Versus Coenergy

The use of flux linkage as an independent variable is a significant drawback to the energy method. Most engineers find it more natural to write down an expression for flux linkage as a function of current rather than vice versa. More importantly, the requirement that the partial derivative of Eq. 4.26 be taken with λ held constant is particularly onerous; most finite-element analysis (FEA) problems are formulated such that currents and material magnetization are held constant.

Fortunately, relief is available in the form of the "coenergy method". Coenergy, denoted W_c, can be thought of as a quantity that is equivalent, but not necessarily equal, to energy. The strategy for using the coenergy to calculate force is identical to that for energy, with the exception that current becomes the independent electrical variable. This is accomplished via a Legendre transform, such that

$$W_c = \lambda i - W. \tag{4.27}$$

Figure 4.3 shows the graphical interpretation of the relationship between energy and coenergy. On the plot of flux linkage versus current in the figure, energy is the area $W = \int i d\lambda$ as in Eq. 4.23, whereas coenergy is the area

$$W_c = \int_0^{i_o} \lambda(i, x) di. \tag{4.28}$$

For a linear material, energy and coenergy are exactly equal, as shown by the areas OAB and OBC, while for nonlinear materials the two quantities are not necessarily equal as in ODE and OEF. Figure 4.4 shows the effect of a change in displacement on

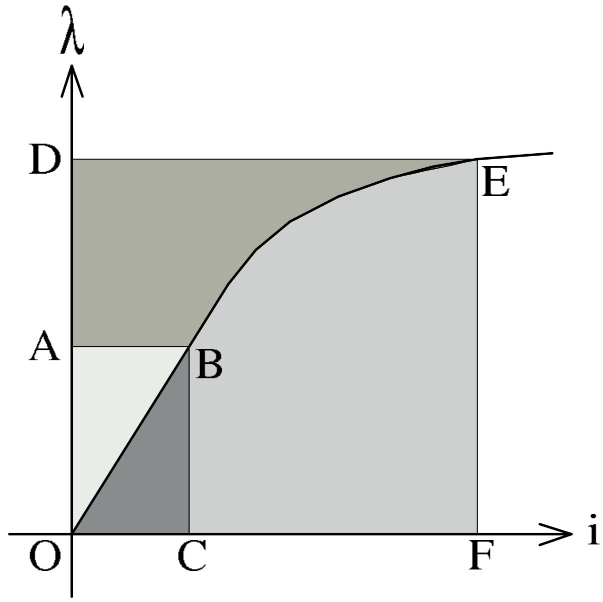

Figure 4.3: Relationship between flux, current, energy and coenergy.

current and flux linkage. The slope of the λ-i plot is inductance, which is a function of actuator displacement. If λ is held constant, the change in energy ΔW is given by the area OAB, while if i is held constant, the change in coenergy ΔW_c is given by the area OAC. Hence ABC is the difference between the two quantities; even for linear materials, a large change in energy is not equal to a large change in coenergy. It is only in the limit, as $\Delta x \rightarrow dx$, that the magnitude of the changes in energy and coenergy are the same. Note however that regardless of magnitude, a change in coenergy has the opposite sign of the corresponding change in energy. Otherwise the calculation follows Eqs. 4.20–4.24, with current as the independent electrical variable. Thus when using the coenergy, Eqs. 4.25 and 4.26 are replaced by

$$\lambda = \left. \frac{\partial W_c}{\partial i} \right|_{x=const} \tag{4.29}$$

$$f = \left.\frac{\partial W_c}{\partial x}\right|_{i=const} . \tag{4.30}$$

The benefit of the coenergy calculation is now apparent — in the force calculation of Eq. 4.30, the differentiation is performed with a constant current in the winding, which is more convenient for finite-element analysis, and provides better physical intuition.

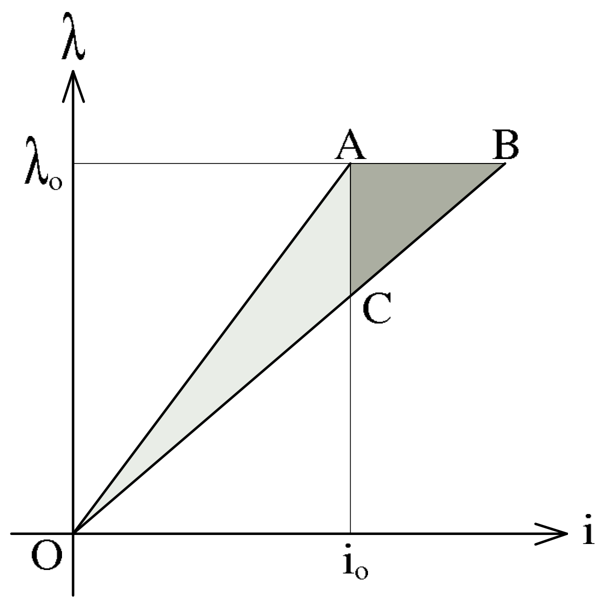

Figure 4.4: Change in energy and coenergy resulting from a change in displacement.

4.3.3 Treatment of Permanent Magnets

Examining Fig. 4.2, it is not immediately apparent how an actuator employing permanent magnets fits into the analysis strategy described in Sections 4.3.1 and 4.3.2. Certainly one can design an actuator that employs a permanent magnet and no windings — such as a simple lifting or holding device — that will nevertheless develop useful mechanical force. How does the analysis proceed when no external currents are present?

There are two approaches to the lumped-element analysis. The first, presented in [70], replaces the magnet with an "equivalent winding" and series reluctance. The winding MMF is chosen to match that of the magnet

$$NI = H_c \ell_{mag} \tag{4.31}$$

and the reluctance is determined by the magnet geometry and permeability

$$R = \frac{\ell_{mag}}{\mu_r \mu_o A_{mag}}. \tag{4.32}$$

For most permanent magnet materials, μ_r falls in the range of 1-10. Consequently, the coenergy (or energy) within the permanent magnet material is significant, and its change with displacement must be included in force calculations. With these changes, analysis can proceed as described in Sec. 4.3.2.

An alternative method for dealing with permanent magnets with arguably more intuitive appeal is presented in [36]. To allow the problem to fall into the mathematical framework of Sections 4.3.1 and 4.3.2, a "fictitious" winding is added to the magnetic circuit in series with the permanent magnet (rather than replacing it). In this way the MMF of the winding can be chosen to exactly cancel that of the magnet (the value can be obtained by negating Eq. 4.31). This allows for the zero-force displacement required by the conceptual development, and introduces a current into the lumped-element model. The integration in Eq. 4.28 is then carried out starting from a nonzero negative current which ensures zero flux in the gap, to a final value of zero current (which is the actual operating point of the real device, which has no winding in that location). Equation 4.28 then becomes

$$W_c(0, x_o) = \int_{i=-i_o}^{i=0} \lambda(i, x) di|_{x=x_o}. \tag{4.33}$$

4.3.4 Treatment of Multiple Windings

It is common for electromechanical actuators to have two, three, or more independent phases to produce a more constant force or torque, and to ensure that displacement occurs in the proper direction. These devices may also incorporate permanent magnets, adding a number of equivalent or fictitious windings in addition to real windings. Hence for many applications, the energy or coenergy method analysis must be extended to account for an arbitrary number of windings. The coenergy method is developed below; the energy method is similar via the Legendre transform described in Sec. 4.3.2.

Imagining the black box in Fig. 4.2 with n electrical terminals, an incremental change in coenergy can be written as

$$dW_c = \sum_{k=1}^{n} \lambda_k di_k + f dx \tag{4.34}$$

and hence the coenergy is given as

$$\begin{aligned} W_c \quad = \quad & \int_{i_1=0}^{i_1=I_1} \lambda_1(i_1, i_2{=}0, \ldots, i_n{=}0) di_1 + \ldots \\ & + \int_{i_k=0}^{i_k=I_k} \lambda_k(i_1{=}I_1, \ldots, i_{k-1}{=}I_{k-1}, i_k, i_{k-1}{=}0, \ldots, i_n{=}0) di_k + \ldots \\ & + \int_{i_n=0}^{i_n=I_n} \lambda_n(i_1{=}I_1, \ldots, i_{n-1}{=}I_{n-1}, i_n) di_n. \end{aligned} \tag{4.35}$$

For linear systems,

$$\begin{aligned} \lambda_1(i_1, i_2{=}0, \ldots, i_n{=}0) \quad &= \quad L_{11} i_1 \\ \lambda_k(i_1{=}I_1, \ldots, i_{k-1}{=}I_{k-1}, i_k, i_{k-1}{=}0, \ldots, i_n{=}0) \quad &= \quad L_{k1} I_1 + \ldots + L_{kk-1} I_{kk-1} + L_{kk} i_k \\ \lambda_n(i_1{=}I_1, \ldots, i_{n-1}{=}I_{n-1}, i_n) \quad &= \quad L_{n1} I_1 + \ldots + L_{nn-1} I_{nn-1} + L_{nn} i_{nn} \end{aligned} \tag{4.36}$$

and the integral 4.35 can be written succinctly as

$$W_c = \tfrac{1}{2}\mathbf{I^T L I} \tag{4.37}$$

where $\mathbf{L}$ is the inductance matrix whose elements satisfy $\lambda_j = L_{jk} i_k$ and $\mathbf{I}$ is the corresponding vector of winding currents. Equations 4.29 and 4.30 then apply as before, where 4.29 is applied to each (λ_k, i_k) pair, and $\mathbf{I}$ replaces i in 4.30.

4.3.5 The Energy Method for Distributed Fields

As stated earlier, the energy and coenergy methods can be applied to distributed field systems as well as lumped element systems. The difference in the distributed case is that the energy or coenergy is not computed from the terminal quantities λ

and i, but rather by computing an energy or coenergy density throughout space, and integrating this density over the volume in question.

Once again the coenergy analysis will be used due to its greater utility for engineering analysis. However, in theory the energy density could be used as well. Coenergy density is defined as

$$W_c' = \int_0^H \mathbf{B} \cdot \mathbf{dH}. \tag{4.38}$$

Of course $\mathbf{B}$ in Eq. 4.38 is a function of $\mathbf{H}$, and the particular function depends on the material in which the fields are acting. For soft magnetic and nonmagnetic materials $B = \mu H$, and thus

$$W_c' = \int_0^H \mu \mathbf{H} \cdot \mathbf{dH}, \tag{4.39}$$

where μ may be a function of $\mathbf{H}$. For linear materials, i.e. those with constant μ, Eq. 4.39 integrates to

$$W_c' = \frac{1}{2}\mu |H|^2. \tag{4.40}$$

For hard magnetic materials, recall that

$$\mathbf{B} = \mu \mathbf{H} + \mathbf{B_r}, \tag{4.41}$$

and thus

$$W_c' = \int_0^H (\mu \mathbf{H} + \mathbf{B_r}) \cdot \mathbf{dH}. \tag{4.42}$$

Again assuming a constant μ, Eq. 4.42 integrates to

$$W_c' = \frac{1}{2} H^2 + \mathbf{Br} \cdot \mathbf{H}. \tag{4.43}$$

From here, the coenergy can be calculated as

$$W_c = \sum_k \int_{V_k} W_c' \, dVol, \tag{4.44}$$

where the integration over each volume V_k in Eq. 4.44 is carried out using an expression for W_c' appropriate for the material occupying the volume (i.e. Eqs. 4.39, 4.40, 4.42, or 4.43). The resulting expression for W_c can be substituted into Eq. 4.30 to find force.

4.4 Finite Element Analysis

Finite element analysis (FEA), sometimes referred to as the finite element method (FEM), is a mathematical tool for obtaining approximate solutions to sophisticated distributed field problems. (The solutions are approximate in a strict mathematical sense; in fact FEA is far more accurate than lumped-element techniques.) The approach is to discretize the problem such that it is amenable to solution with a computer. A detailed description of FEA is beyond the scope of this work — the interested reader is referred to [71] or similar works. In this section, a brief overview of the method is given, along with notes on its application to force calculations for electromagnetic devices.

4.4.1 Calculation of the Finite Element Solution

Finite element analysis begins with the definition of a problem geometry and boundary conditions, and the generation of a mesh. The geometry is the physical shape of the device under consideration; material properties such as permeability, and operating point information such as current density, are typically associated with various regions of the geometry. Boundary conditions are of three types: "Dirichlet", in which the value of the solution vector is held constant; "Neumann", in which the derivative of the solution is set to zero; and "periodic" in which a fixed relationship between two node solutions is specified. In magnetic field problems, the Dirichlet condition forces magnetic flux lines parallel to the boundary, the Neumann condition forces flux lines perpendicular to the boundary, and the periodic condition can be used to model a single pole pair of a multi-pole machine by setting boundaries on opposite sides of the geometry to be equal.

The mesh is the set of points (called nodes) within the volume of the geometry that discretizes the problem. The nodes define the vertices of polygons — usually triangles in 2–D, or tetrahedra in 3–D — which are called the elements. A shape function is chosen to approximate the solution over the area (or volume) of each element. Linear or quadratic functions of the spatial variables suffice for many problems. The coefficients of this polynomial can then be determined in terms of the node values, and hence a closed-form expression exists for the solution within each element.

A scalar expression for the difference between energy stored in the field (expressed as the integral of **H** with respect to **B**) and energy delivered to the system (expressed as the integral of **J** with respect to **A**) is developed for each element. The sum of the value of this expression over all the elements is called an energy functional, and for the exact field solution its value is zero. However, because the shape function is in general only an approximation, the "best fit" solution is that which drives the energy functional closest to zero. Hence the essence of finite element analysis is the minimization of this functional.

The finite-element solution for magneto-quasistatic problems is given in terms of the magnetic potential vector **A**. The flux density **B** can then be reconstructed from the definition

$$\mathbf{B} = \nabla \times \mathbf{A}, \tag{4.45}$$

and **H** then determined from Eq. 4.10 or Eq. 4.41 as appropriate.

4.4.2 Force Calculations

The strategy for force or torque calculation via FEA follows Sec. 4.3.5, with the volume integral in Eq. 4.44 replaced by a summation over the elements:

$$W_c = \Sigma_k W_c'[k] \cdot Vol[k]. \tag{4.46}$$

For each displacement at which the force is to be determined, the finite-element solution and coenergy must be calculated twice: once at a small negative perturbation

ϵ from the point of interest; and once at a small positive perturbation. The two displacements and two coenergy values can then be used to approximate the force via a numerical differential:

$$F(x_o) = \frac{W_c(x_o+\epsilon) - W_c(x_o-\epsilon)}{(x_o+\epsilon) - (x_o-\epsilon)} = \frac{\Delta W_c}{2\epsilon}. \tag{4.47}$$

The fact that two solutions must be calculated for each displacement, and that each solution can require significant computation time (on the order of minutes to hours with modest computing resources), limits the utility of FEA for design synthesis or optimization, in which many solutions are desired quickly.

4.5 A Comparison of Various Analysis Methods

Here the analyses described in Secs. 4.2-4.4 are performed for a simple test structure. The purpose of this section is to provide practical detail to support the theoretical calculations above, as well as to highlight some of the advantages and drawbacks of the various methods.

The test structure is shown in Fig. 4.5. This is an extremely simple device in which a permanent magnet and soft magnetic yoke apply force to a soft magnetic sliding element which is constrained to move only in the horizontal direction. The winding is a “fictitious winding”, as described in Sec. 4.3.3, which is not part of the actuator structure but rather a conceptual tool that will be required for the analysis in some of the sections below. The structure has uniform thickness, and uniform

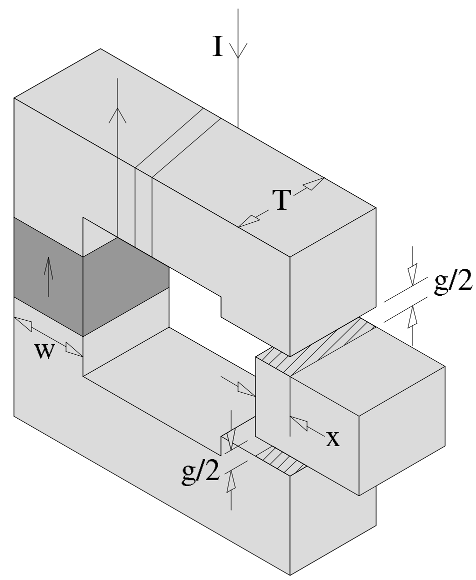

Figure 4.5: Test structure for electromagnetic analysis.

cross section in the yoke. The soft magnetic material has high permeability, and it is henceforth assumed to support no differential in **H** along its length, or equivalently to have zero reluctance. The gaps are filled with air having permeability of μ_o; the permanent magnet has remanent flux density $\mathbf{B_r}$, and for simplicity is assumed to have relative permeability $\mu_r = 1$.

4.5.1 Field Quantities

In this section, disregard the fictitious winding. From the assumptions above and Eq. 4.2, the magnetic fields in the magnet (H_m) and gap (H_g) are related by

$$H_m \ell_m = -H_g g, \tag{4.48}$$

and from Eq. 4.4, the magnet and gap flux densities are related by

$$B_m A_m = B_g A_g. \tag{4.49}$$

Noting that $B_g = \mu_o H_g$, Eqs. 4.48 and 4.49 can be combined to give

$$B_m \frac{A_m}{A_g} = -\mu_o H_m \frac{\ell_m}{g}. \tag{4.50}$$

Rearranging and multiplying top and bottom by μ_o results in

$$B_m = -\mu_o H_m \frac{R_m}{R_g}, \tag{4.51}$$

where the reluctances of the magnet and gap are defined according to Eq. 4.15.

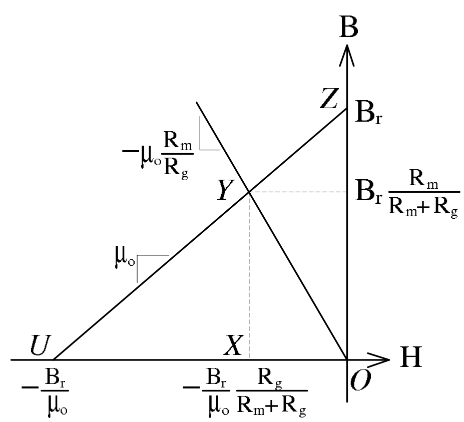

Figure 4.6: Graphical depiction of field quantities in test structure.

Figure 4.6 shows a graphical interpretation of Eqs. 4.48-4.51. The permanent magnet can operate at any point on its demagnetization curve, given for an ideal magnet by Eq. 4.41. This is the line UZ in the figure. Meanwhile the gap reluctance constrains the magnet to operate on a line passing through the origin with slope

$-\mu_o \frac{R_m}{R_g}$ (line OY). The intersection of the two lines must be the operating point of the magnet, which can be shown to be the point where

$$B_m = B_r \frac{R_m}{R_m + R_g} \tag{4.52}$$

and

$$H_m = -\frac{B_r}{\mu_o} \frac{R_g}{R_m + R_g}. \tag{4.53}$$

The corresponding quantities for the gap can then be found from Eqs. 4.48 and 4.49:

$$B_g = B_r \frac{R_m}{R_m + R_g} \frac{A_m}{A_g} \tag{4.54}$$

and

$$H_g = \frac{B_r}{\mu_o} \frac{R_g}{R_m + R_g} \frac{\ell_m}{g}. \tag{4.55}$$

4.5.2 Magnetic Circuit Analysis

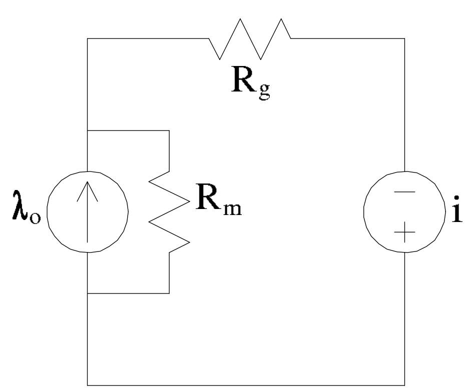

Figure 4.7: Magnetic circuit model of test structure.

Figure 4.7 shows the equivalent magnetic circuit for the magnetic structure of Fig. 4.5. Applying equation 4.4 at the node between the permanent magnet and the gap reluctance gives

$$\lambda_m = \lambda_o - \lambda_g \tag{4.56}$$

where λ_o is the flux linkage corresponding to B_r, λ_m is the leakage flux across the magnet, and λ_g is the flux that crosses the gap. Summing MMFs around the loop gives

$$\lambda_m R_m - \lambda_g R_g + i = 0. \tag{4.57}$$

Substituting in Eq. 4.56 then gives the gap flux, in terms of the magnet remanent flux and the current in the fictitious winding:

$$\lambda_g = \lambda_0 \frac{R_m}{R_m + R_g} + i \frac{1}{R_m + R_g} \tag{4.58}$$

4.5.3 Coenergy Calculation Via Fictitious Winding

To find the coenergy using the magnetic circuit model and the fictitious winding method, Eq. 4.33 is applied. Recall that the integration of flux linkage with respect to current is carried out from a starting current that ensures zero flux in the gap, in this case $i_o = -\lambda_o R_m$ (by inspection of Eq. 4.58). Thus

$$W_c = \int_{-\lambda_o R_m}^{0} \lambda_g(i) di = \int_{-\lambda_o R_m}^{0} \lambda_0 \frac{R_m}{R_m + R_g} + i \frac{1}{R_m + R_g} di, \tag{4.59}$$

which evaluates to

$$W_c = \frac{1}{2} \frac{(\lambda_o R_m)^2}{R_m + R_g}. \tag{4.60}$$

4.5.4 Coenergy Calculation Via Equivalent Winding

The alternative to the fictitious winding method, as discussed in Sec. 4.3.3, is to simply replace the permanent magnet, for purposes of analysis, with a Thevenin equivalent winding and series reluctance. In this case the fictitious winding is not necessary. The Thevenin equivalent winding carries current $i = \lambda_o R_m$, and the series reluctance is simply $R_m = \frac{\ell_m}{\mu_o A_m}$. The coenergy is calculated by integrating the flux linking the equivalent winding with respect to current:

$$W_c = \int_0^{\lambda_o R_m} \lambda_g(i) di = \int_0^{\lambda_o R_m} \frac{i}{R_m + R_g} di. \tag{4.61}$$

Equation 4.61 evaluates, as expected, to

$$W_c = \frac{1}{2} \frac{(\lambda_o R_m)^2}{R_m + R_g}. \tag{4.62}$$

4.5.5 Coenergy Calculation Via Coenergy Density

The coenergy can also be calculated by first finding the coenergy density in a particular region, and then integrating over the volume of the region as discussed in Sec. 4.3.5. In the case of a structure with permanent magnets, a large portion of the coenergy can be contained within the magnet volume, and hence this volume must be included in the calculation. Recalling Eq. 4.38, the coenergy density in the permanent magnet can be found by substituting in Eq. 4.41:

$$W'_{c,pm} = \int_0^{H_m} (\mathbf{B_r} + \mu_o \mathbf{H}) \mathbf{dH} = (\mathbf{B_r} \cdot \mathbf{H_m}) + \frac{1}{2} \mu_o |\mathbf{H_m}|^2. \tag{4.63}$$

Substituting in Eq. 4.52, after some manipulation, gives

$$W'_{c,pm} = -\frac{B_r^2}{\mu_o}\left(\frac{\frac{1}{2}R_g^2 + R_g R_m}{(R_g{+}R_m)^2}\right). \tag{4.64}$$

For the gap,

$$W'_{c,gap} = \int_0^{H_g} \mu_o \mathbf{H}\cdot\mathbf{dH} = \frac{1}{2}\mu_o|\mathbf{H_g}|^2, \tag{4.65}$$

and using Eq. 4.38 and Eqs. 4.54 and 4.55:

$$W'_{c,gap} = \frac{B_r^2}{\mu_o}\left(\frac{\frac{1}{2}R_g^2}{(R_g{+}R_m)^2}\right)\left(\frac{\ell_m}{g}\right)^2. \tag{4.66}$$

The total coenergy is thus given by

$$W_c = W'_{c,pm}\ell_m A_m + W_{c,gap} g A_g, \tag{4.67}$$

which reduces to

$$W_c = -\frac{1}{2}\lambda_o^2\frac{R_m R_g}{R_g + R_m}. \tag{4.68}$$

That this result does not match Eqs. 4.60 and 4.62 would seem to be a problem. However, it is demonstrated in the next section that both expressions give the same result for the calculation of force.

4.5.6 Equivalence of Lumped Element and Field Calculation

Consider again Fig. 4.6. If the figure is scaled by A_m on the B axis, and by ℓ_m on the H axis, the plot is now in terms of permanent magnet flux linkage and MMF. The remanent flux density B_r is replaced by λ_o, and the point $-\frac{B_r}{\mu_o}$ on the H axis becomes $-\lambda_o R_m$. The slope of the permanent magnet operating characteristic is now

$\frac{1}{R_m}$, and the slope of the load line is $-\frac{1}{R_g}$. This scaled situation is depicted in Fig. 4.8, which also indicates other relevant quantities.

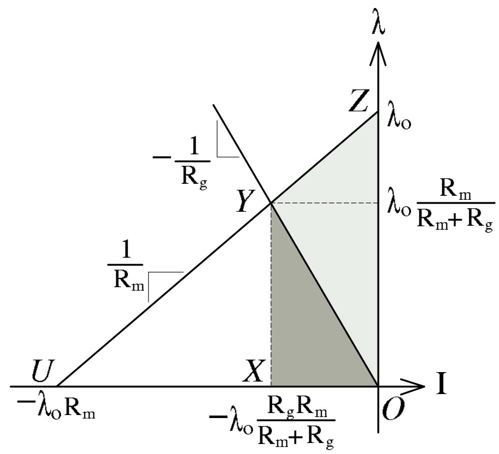

Figure 4.8: Graphical depiction of terminal quantities of test structure.

It can be shown that region OYZ in Fig. 4.8 now represents the coenergy calculated via the coenergy density in Eq. 4.68. Meanwhile, examining Eqs. 4.60 and 4.62 it is clear that this is the expression for the area of region OYU in the figure.

A displacement of the mechanism's sliding element will cause a change in the gap reluctance and hence the slope of the load line OY. This displacement causes a change of equal magnitude in the areas OYZ and OYU, although with different signs (hence the differing signs of Eqs. 4.62 and 4.68). In fact OYZ and OYU differ by the constant OUZ, and thus it must be that when the actuator force is calculated via the differentiation of Eq. 4.30, both coenergy expressions must give the same result. Differentiating either expression with respect to x, with the quantity $\lambda_o R_m$

held constant, results in the force expression

$$F = \frac{1}{2}\left(\frac{B_r}{\mu_o}\right)^2 \frac{\mu_o T g}{(\frac{g}{\ell_m} + \frac{x}{w})^2}. \tag{4.69}$$

Figures 4.9 and 4.10 compare Eqs. 4.68 and 4.69, respectively with values computed via FEA. Results are for dimensions w=ℓ_m=T=1 cm and g=0.25 mm, and remanence B_r=1.0 T. For large displacements, the gap reluctance is low, and the results are in good agreement. For small displacements, however, the fringing reluctance in the FEA result is of the same order as the gap reluctance; the magnetic circuit analysis does not model this effect, leading to significant error.

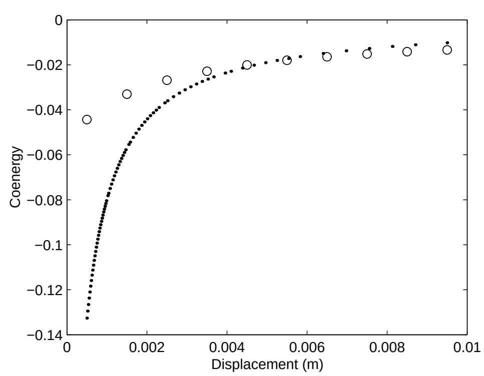

Figure 4.9: Coenergy versus displacement of test structure. The FEA result is given by circles, while the magnetic circuit result is given by dots.

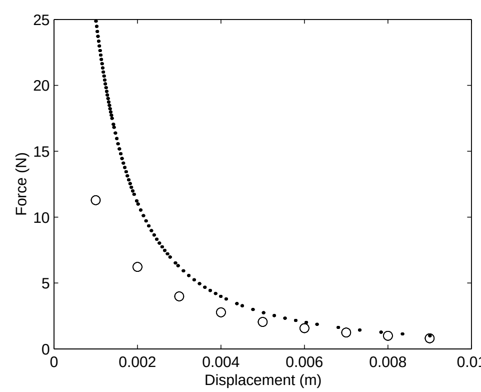

Figure 4.10: Force versus displacement of test structure. The FEA result is given by circles, while the magnetic circuit result is given by dots

Chapter 5

Machine Design and Analysis — Millimeter Scale

This chapter describes the design, construction and testing of a millimeter-scale electromagnetic generator intended to be coupled to a MEMS internal combustion engine. The novel configuration of the machine posed several challenges to analysis which are described in Sec. 5.2. The machine's configuration as well as its size — small for the macro-scale, large for the micro-scale — introduced some construction issues, as detailed in Sec. 5.3. Experimental results are presented in Sec. 5.4.

5.1 Design

The generator configuration shown in Figs. 5.1 and 5.2 was developed in response to two major constraints: the unusual Wankel rotor geometry, which is not well

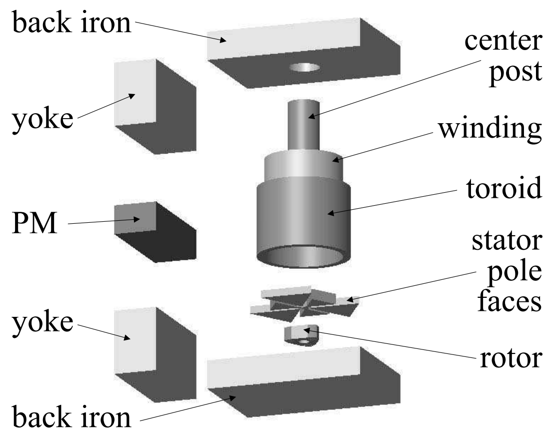

Figure 5.1: Millimeter-scale generator assembly (engine housing suppressed for clarity).

suited to a radial flux design; and the high temperature of the rotor (300°C), which operates in a combustion environment, making a permanent magnet rotor impractical. The generator could be described as an axial flux circumferential current (AFCC) permanent magnet machine, although we note significant differences with the design presented in [72]. The configuration might best be described as an axial-flux claw-pole stator machine, not unlike radial flux designs with concentrated windings presented in [73] and [74]. The stator is a six-pole, single-phase configuration, with the permanent magnet being part of the stator assembly. The flanged triangular rotor (shown in Fig. 5.3) has a soft magnetic pole in each of its three tips. The design allows for thermal insulation between the stator and combustion chamber, and places the permanent magnet in a relatively low temperature location. The axial flux configuration is insensitive to the shape of the rotor poles, and allows simple assembly by sandwiching the engine housing between the upper and lower halves of the stator. The winding

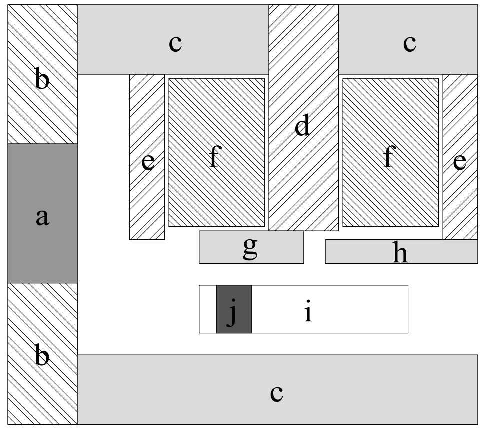

Figure 5.2: Millimeter-scale generator schematic cross-section (not to scale). Part names and materials are given below.

a.	Permanent magnet	Bonded NdFeB
b.	Magnet yoke	Low-carbon steel
c.	Back iron	Powdered iron
d.	Center post	Silicon Steel
e.	Toroid	Silicon Steel
f.	Winding	Copper
g.	Center-connected pole face	Powdered iron
h.	Edge-connected pole face	Powdered iron
i.	Rotor	Silicon
j.	Rotor pole	Nickel-iron

arrangement provides for excellent utilization of copper — there are no end turns, none of the dimensions of the coil are constrained by the rotor or permanent magnet structures, and the winding resistance is independent of pole number. The inner diameter of the winding is determined only by the saturation and loss properties of the core material, while the outer diameter and length can be varied to meet performance and size criteria.

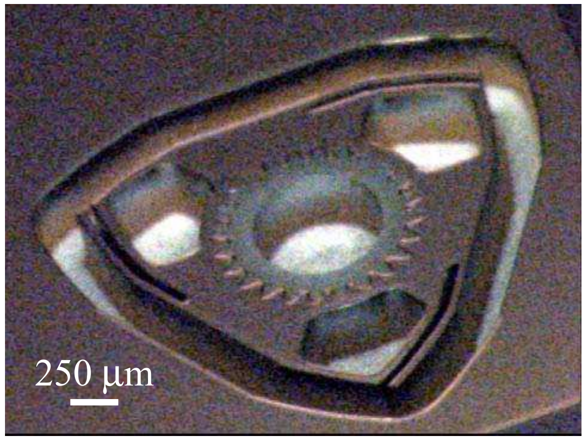

Figure 5.3: Microfabricated Wankel rotor, before electroplating.

5.2 Analysis

Several aspects of the design pose obstacles to straightforward analysis. Flux in the generator travels in three dimensions — axially, radially, and circumferentially. Examination of any one cross section of the machine does not yield a complete picture of the flux paths. Care must be taken in formulating magnetic circuit and finite element models to consider the generator as a three dimensional whole. Note also that the motion of the Wankel rotor includes both rotation and a small eccentricity (i.e. translation in a circular trajectory). Because the eccentricity is much smaller than the rotor radius, the rotor motion is approximated as purely rotational. Perhaps most importantly, the generator is homopolar; the magnetic field in the gap changes in magnitude, but not polarity, as the rotor turns. This implies that performance will be sensitive to saturation of the stator. If the bias field imposed on the stator by the permanent magnet is too large, the low incremental permeability of the stator components will reduce the AC flux linking the coil, resulting in a decrease in power output.

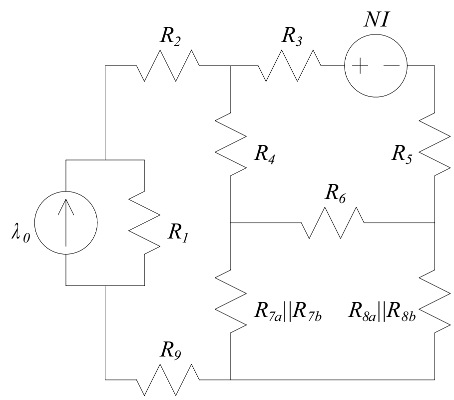

Figure 5.4: Magnetic circuit model of millimeter-scale generator.

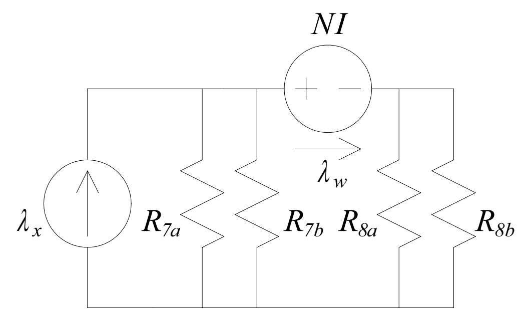

Figure 5.5: Simplified magnetic circuit model for millimeter-scale generator, assuming high permeability in the soft magnetic components. Expressions for the reluctances are given in Eqs. 5.1-5.4

Figure 5.4 shows a magnetic circuit model of the generator corresponding to the cross-section of Fig. 5.2. The permanent magnet is represented by a flux source λ_o in parallel with a leakage reluctance R_1. The winding appears as an MMF source NI. Reluctance R_2 represents the top portion of the magnet yoke; R_3 represents the top portion of the back iron. Reluctance R_4 models the series combination of the toroid and edge-connected pole faces. Similarly, R_5 models the series combination of the center post and center-connected pole faces. The pole to pole leakage path in the stator is represented by R_6. Reluctances R_{7a} and R_{7b} model two paths from the edge-connected pole faces to the lower back iron — one bypassing the rotor poles and one linking the rotor poles, respectively. Similarly, R_{8a} and R_{8b}, model flux paths from the center-connected pole faces to the back iron. Expressions for R_{7a}, R_{7b}, R_{8a} and R_{8b} are given below. Finally, R_9 represents a series combination of the lower back iron and lower magnet yoke, as well as the rotor shaft reluctance when the test rotor described in Section 5.3 is in place.

For the purposes of design, extracting closed-from expressions from a magnetic circuit model with more than five or six elements can be unwieldy. To develop design intuition, a simpler model such as the one shown in Fig. 5.5 is useful. Here high permeability is assumed in the soft magnetic materials, such that the air gaps dominate the design.

Defining area and length parameters as in Figs. 5.6 and 5.7, the reluctances in Fig. 5.5 can be written as

$$R_{7a} = \frac{\ell_a}{\mu_o(A_z - A_x(1-(\theta\frac{P}{2\pi})))} \tag{5.1}$$

$$R_{7b} = \frac{\ell_a - \ell_b}{\mu_o A_x(1-(\theta\frac{P}{2\pi}))} \tag{5.2}$$

$$R_{8a} = \frac{\ell_a}{\mu_o(A_y - A_x\theta\frac{P}{2\pi})} \tag{5.3}$$

$$R_{8b} = \frac{\ell_a - \ell_b}{\mu_o(A_x\theta\frac{P}{2\pi})} \tag{5.4}$$

where P is the number of poles, and the rotor angle θ varies from 0 to $\frac{2\pi}{P}$. Note that in this simple model, the parallel combination of all four reluctances does not depend on the rotor position θ, and the leakage reluctance across the permanent magnet is large compared to the gap reluctance. Hence the use of a constant flux source λ_x is justified.

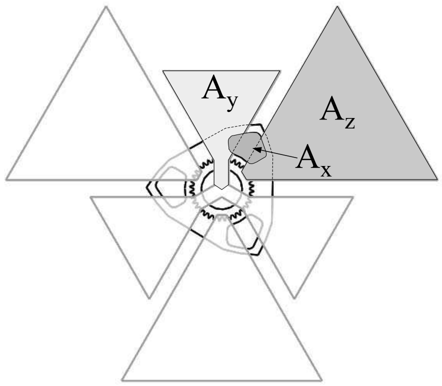

Figure 5.6: Pole area parameter definitions. The figure shows a plan view of the stator pole faces and rotor.

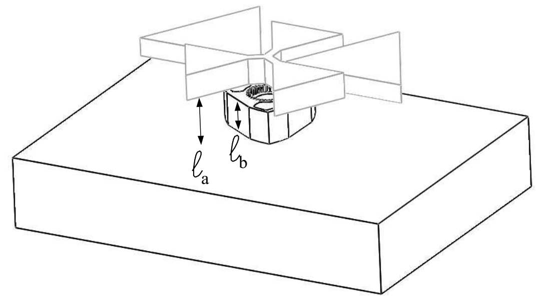

Figure 5.7: Length parameter definitions. The figure shows a perspective view of the stator pole faces, rotor, and back iron. Note that one stator pole face has been suppressed for clarity.

From Eqs. 5.1-5.4 and Figs. 5.5-5.7, the operation of the generator is apparent. As the rotor turns, flux from the permanent magnet is directed either around the outside of the winding, or through its center. This changing flux linkage through the winding generates the back-emf voltage.

Not only is the back-emf voltage intuitive and easy to compute, but it can be shown that for an ideal machine under steady-state conditions, the back-emf constant is equal to the torque constant [75]. Thus torque should be proportional to back-emf per turn, and the back-emf expression reveals a great deal about the design. From Fig. 5.5 we have

$$\lambda_w = \frac{R_{7a} \| R_{7b}}{(R_{7a} \| R_{7b}) + (R_{8a} \| R_{8b})} \lambda_x, \tag{5.5}$$

and substituting from Eqs. 5.1-5.4

$$\lambda_w = \frac{\ell_b A_x \theta + (\ell_a - \ell_b) A_y}{\ell_b A_x + (\ell_a - \ell_b)(A_y + A_z)} \lambda_x \tag{5.6}$$

gives the flux linking the winding (λ_w). Taking the derivative with respect to time under constant speed rotation gives the back-emf

$$V_o = \frac{\ell_b A_x}{\ell_b A_x + (\ell_a - \ell_b)(A_y + A_z)} \lambda_x \cdot \omega. \tag{5.7}$$

Examining Eq. 5.7, we see that a large ratio of ℓ_b to $(\ell_a - \ell_b)$ (i.e. a small gap) is desirable, as is a rotor pole area A_x that is equal in size to the stator pole areas A_y and A_z.

Using the circuit in Fig. 5.5, an expression for torque can also be derived. One approach is to calculate the coenergy in the gap, and then take the derivative of coenergy with respect to rotor angle to obtain torque. Note that since the flux in the permanent magnet is assumed to be constant, its contribution to the change in coenergy can be neglected. Coenergy in the soft magnetic components is small due to the materials' high permeability, and is also neglected.

Equation 5.8 gives an expression for the torque produced by a generator with P poles and winding current NI. The flux density in the rotor due only to the permanent magnet (B_{pm}) is assumed in the model to be independent of rotor position, hence it is simpler to formulate Eq. 5.8 in terms of this quantity rather than λ_x. The first term in square brackets is the torque due to Lorentz forces, while the second term is due to reluctance forces. For moderate winding currents the reluctance forces are small compared to the Lorentz forces, and the torque can be approximated for initial design purposes by the Lorentz expression only. The absence of a term involving B_{pm}^2 indicates that this model predicts zero cogging torque.

$$\begin{aligned}\tau &= \left[\frac{P^2}{4\pi}\left(\frac{\ell_b}{\ell_a}\right)A_x B_{pm} NI\right] + \left[\frac{\mu_o P^2}{\pi^2}\left(\frac{\ell_b}{\ell_a}\right)\right]\cdot \\ &\quad \left[\frac{A_x\{(\ell_a - \ell_b(A_y - A_z)\pi + \ell_b A_x(\theta P - \pi)\}}{(\ell_a - \ell_b)\{(\ell_a - \ell_b)(A_y + A_z) + \ell_b A_x\}}(NI)^2\right]\end{aligned} \tag{5.8}$$

Equation 5.8 gives intuition into the possibility of increasing the torque in the machine. Larger rotor pole area, a thicker rotor, and high flux densities all offer a linear increase in torque. Note however that torque increases with the square of the number of poles. Further, because the generator winding resistance is independent of the pole number, the only limits on the number of poles come from practical limits on the minimum gap size (and hence the pole arc length at which fringing begins to dominate), and higher core loss due to higher electrical frequencies. In the design presented here, a six pole configuration was chosen solely to coincide with the triangular shape of the Wankel rotor; the optimal pole number in terms of performance was not investigated.

While Eqs. 5.7 and 5.8 are useful in providing design intuition, a more accurate analysis is provided by numerical solution of the detailed magnetic circuit model of Fig. 5.4, using finite values for R_1, R_2, R_3, R_4, R_5, R_6 and R_9. As noted above, the homopolar nature of the design makes the generator output sensitive to saturation effects. These effects are difficult to calculate by hand; to more accurately model saturation as well as fringing effects, finite element analysis (FEA) can be applied with appropriate saturation characteristics for the soft magnetic materials.

With modest computing resources, nonlinear three-dimensional FEA can be difficult. Hence a series of two dimensional finite element models was developed, as shown in Fig. 5.8. The figure shows four axisymmetric magnetostatic models, representing cross-sections through two different $r-z$ planes of the generator, at two different rotor positions. In Fig. 5.8a, the cross section is taken through a center-connected stator pole, with the rotor in an aligned position. Figure 5.8b shows a cross section through an edge-connected stator pole at the same rotor position. Figures 5.8c and 5.8d show the same cross sections for the complementary rotor position, where the rotor is aligned with the edge-connected stator pole face.

From these FEA solutions, values for the relative permeability (μ_r) in each of the soft magnetic components can be determined. Because of their implicit axisymmetry, no one model captures the exact operating point of the generator. However, interpolating between 5.8a and 5.8b, and 5.8c and 5.8d can give estimates of the level of saturation and appropriate μ_r values for rotor positions $\theta=\frac{\pi}{3}$ and $\theta=0$ respectively.

Substituting these permeabilities into the magnetic circuit model of Fig. 5.4, flux linking the winding can be determined for the two rotor positions. Assuming these values to be the maximum and minimum of a sinusoidally varying flux, back-emf can be estimated. Using this method, we calculate a back-emf amplitude of 218 $\frac{\mathrm{nV \cdot s}}{\mathrm{rad \cdot turn}}$.

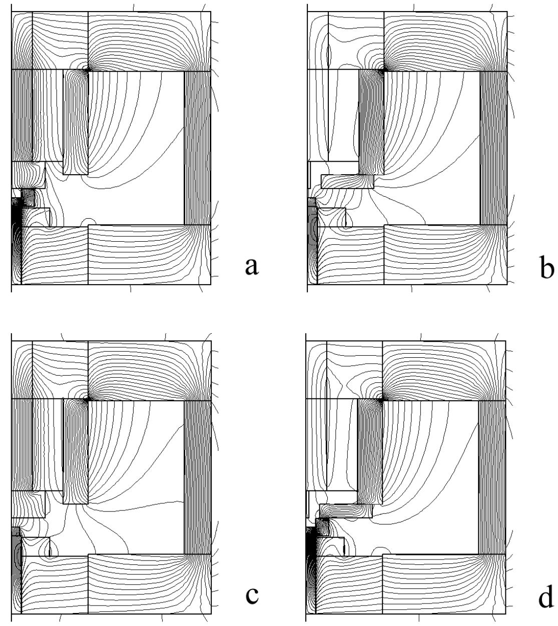

Figure 5.8: Axisymmetric finite element models, using the steel test rotor. The left side of each model is the axis of symmetry. Plotted are lines of constant magnetic potential.

5.3 Construction

A prototype has been constructed; the upper portion of the stator is shown in Fig. 5.9. Different soft magnetic materials were used for the various stator components, according to their particular requirements. The stator pole faces are made from powdered iron material (Micrometals' "-26" material [38]). This material was selected for its low loss, high saturation flux density, and isotropic properties. Due to their fine feature sizes, the stator pole faces were formed by electrical discharge machining (EDM). The stator pole faces were positioned with the help of a template, and then potted together with epoxy. The potted stator pole faces are shown in Fig. 5.10. Powdered iron was also used for the top and bottom portions of the back iron, again due to its low loss and isotropic properties. These pieces were machined with conventional techniques.

Figure 5.9: Partial stator assembly of millimeter-scale generator prototype, back iron and permanent magnet not shown.

In the center post and toroid portions of the stator, flux distribution is one- or two-dimensional, and high permeability is desired. Sheets of silicon steel (Arnold's "Arnon 5" [37]) 0.005" thick, with magnesium phosphate insulation, were used for these parts. The center post was formed by folding and compressing a single sheet of steel into a layered structure, and then grinding to final shape. The toroid was formed into a roll and secured with epoxy, and the ends were milled to final dimension. Both parts were then etched with dilute nitric acid in a 1:1 ratio of HNO_3:H_2O for 10 seconds to discourage edge-to-edge conduction between laminations. The center post was polished with fine-grain sandpaper before assembly. The finished center post and toroid appear in Figs. 5.11 and 5.14 respectively. The winding consists of 4200 turns of 50 AWG wire on a plastic bobbin that encloses the center post and fits inside the toroid.

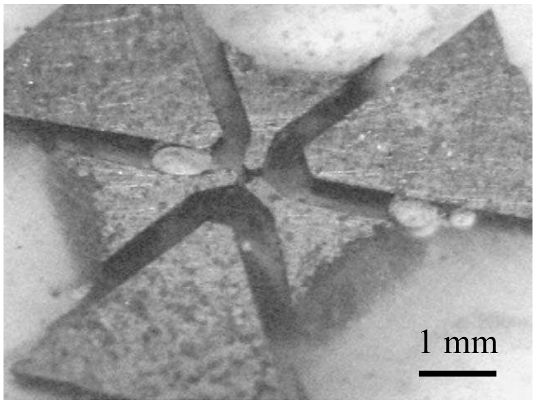

Figure 5.10: Powdered iron stator pole faces potted in epoxy.

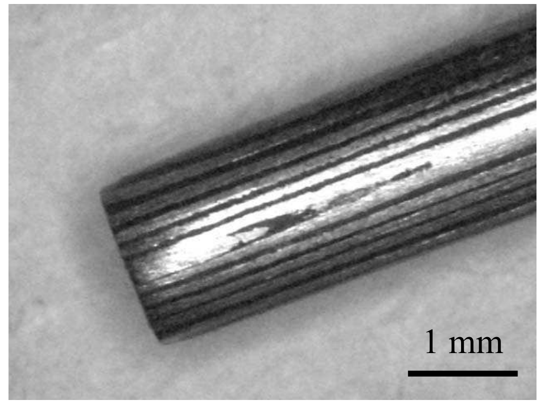

Figure 5.11: Laminated silicon steel center post, after etching and polishing.

The permanent magnet was machined from bonded NdFeB ("Neoform" from Dexter Magnetic Technologies [76]) and then magnetized. Due to the sensitivity of the generator design to saturation effects, a fixture was made to hold the permanent magnet and its two yoke pieces. The fixture allows the magnet to be gradually removed from the yoke by turning a screw. Thus the optimal amount of excitation can be determined experimentally.

The silicon rotor was fabricated in the U.C. Berkeley microlab, as described in [27]. The process begins with a 500 μm silicon wafer. Trenches are etched in the shape of the rotor poles. The wafer is then bonded to a second wafer which has a copper seed layer, and the wafer stack is electroplated with a 50:50 ratio of nickel to iron. This composition was selected to satisfy both curie temperature (350° C as given in [33]) and thermal expansion constraints. The electroplated rotor is shown

Figure 5.12: Electroplated rotor, before final DRIE [77].

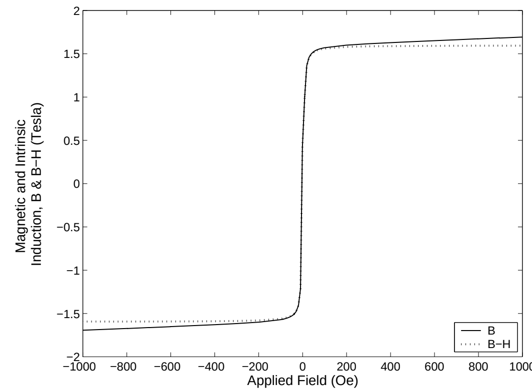

Figure 5.13: B-H characteristic of electroplated NiFe material [77].

in Fig. 5.12; the B-H characteristic of the NiFe material is shown in Fig. 5.13. The top surface of the plated wafer is then planarized, the seed wafer is removed, and the remaining features of the rotor are etched using deep reactive ion etching (DRIE).

Because the development of the MEMS Wankel engine has proceeded in parallel with the generator development, an electroplated silicon rotor was not available for generator testing at the time of writing. Hence a solid steel rotor (Fig. 5.15) was machined with salient pole shapes roughly matching those of the silicon Wankel rotor (Fig. 5.3). This test rotor has a shaft to allow the spinning of the rotor with an external electric motor.

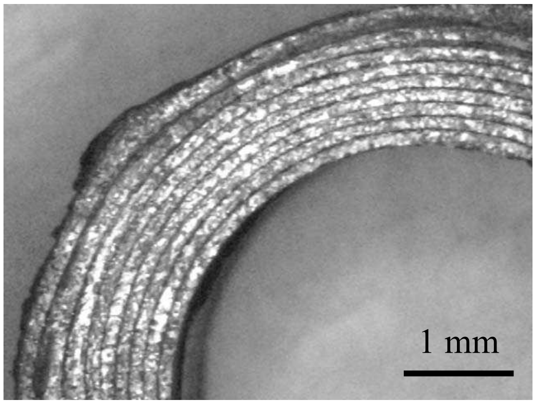

Figure 5.14: Laminated silicon steel toroid, after etching.

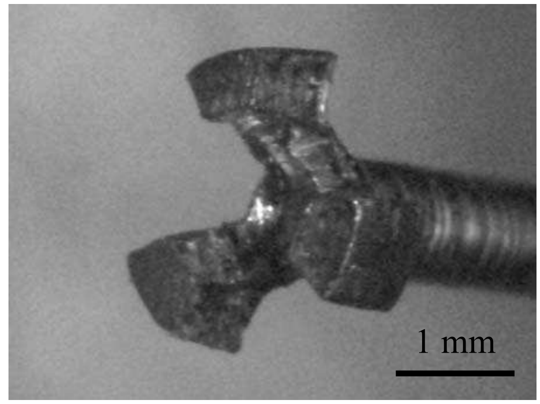

Figure 5.15: Steel test rotor. The salient poles are intended to roughly match the size and shape of the pole areas in Fig. 5.3.

5.4 Results

5.4.1 Torque

Direct measurement of torques on the order of microNewtons is extremely challenging. Hence to estimate the torque developed by the generator, an indirect measurement via mechanical resonance was performed. The experimental setup is shown in Fig. 5.16.

The experimental procedure was as follows. The stator was securely fixed to the bench, with the stator pole faces facing upwards. A permanent magnet was placed adjacent to the stator back iron, but the lower portion of the back iron was not included. A test rotor fitted with a large cylindrical proof mass was suspended vertically above the stator by a long, thin wire, such that in the rest position, the rotor poles were directly above the slots between the stator poles. The stator coil was

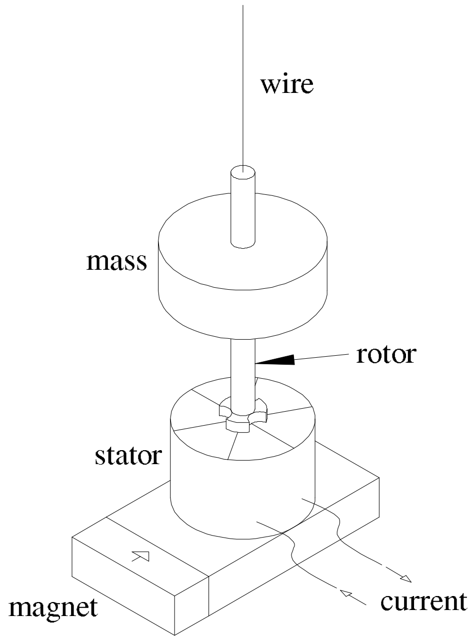

Figure 5.16: Experimental setup for torque estimation via mechanical resonance.

then energized with a DC current, producing a torque on the rotor to align the rotor and stator poles. Because of its large mass and low damping, the rotor settled into its equilibrium position in an oscillatory manner; the frequency of this oscillation was recorded. The coil excitation was then turned off, allowing the rotor to settle to its original position, with the frequency of oscillation again recorded.

Because of the low mechanical damping of the system (more than 20 cycles of ringing were visible to the naked eye), a mass-spring model for the system was assumed, with the proof mass dominating the moment of inertia, and both the suspending wire and electromagnetic torque providing spring forces. The natural frequency of such a system is given by

$$\omega_n = \sqrt{\frac{K}{J}}, \tag{5.9}$$

where K is the rotational spring constant, and J is the rotational moment of inertia. For the proof mass, J was calculated to be 24.45×10^{-9} kg$\cdot$m^2, and oscillation frequencies of 8.55 rad/sec and 15.71 rad/sec were measured for the relaxed and energized states, respectively. From Eq. 5.9, the calculated spring constants were 1.79×10^{-6} N$\cdot$m/rad for the relaxed state, and 6.03×10^{-6} N$\cdot$m/rad for the energized state.

The spring constant in the relaxed state is due only to the torsion of the wire, whereas in the energized state the spring constant comes from both the wire and the electromagnetic torque. Thus subtracting the two values gives the spring constant due only to electromagnetic torque, equal to 4.24×10^{-6} N$\cdot$m/rad. Assuming peak torque occurs for the 6 pole generator at $\frac{\pi}{6}$ rad, the peak torque can be calculated as 2.22×10^{-6} N$\cdot$m. The current for this test was 100 mA, and hence the torque constant for the machine was estimated to be 22.2×10^{-6} N$\cdot$m/A. Note that the machine configuration for this experiment was significantly different than that used in later tests, in that the lower portion of the back iron was removed in order to allow the rotor to spin freely. Further, due to stretching of the suspension wire, the gap length for the torque experiment was not well characterized. Thus the torque constant calculated here differs from the voltage constant calculated in Sec. 5.4.2.

5.4.2 Open-Circuit Voltage and Power

The assembled generator was mounted on a test stand that allows axial adjustment of gap length and lateral adjustment of rotor position. After setting the gap length, lateral position was manually adjusted for maximum back-emf. As described in Sec. 5.3, permanent magnet excitation was also manually adjusted to maximize back-emf. Resistance and inductance measurements were then made with an LCR meter at 120 Hz and 1 kHz. Measured and calculated values for the winding resistance (R_w), winding inductance (L_w), back-emf constant (K_v), open-circuit voltage (V_o) and maximum power output ($P_{out,max}$) are summarized in Table 5.1.

The nominal speed of operation for the MEMS Wankel engine is a shaft speed of 40 kRPM, corresponding to a rotor speed of 13.3 kRPM, and an electrical frequency of 667 Hz. All the voltage and power measurements reported here were obtained by spinning the steel test rotor with an external DC electric motor at 13.3 kRPM. Because the motor was operated without speed control, variation in the electrical frequency of about 2.5% was observed. In the following, the actual frequency of measurements has been noted where appropriate.

Experimental data showing the open-circuit voltage waveform across the generator terminals appears in Fig. 5.17. The output has a magnitude of approximately 2.63 V at 677 Hz. The subharmonic content is believed to be due to asymmetries in the rotor which cause variations in the waveform once per shaft rotation, or every three

Quantity	Calculated*	Measured
K_v	$218\ \frac{\text{nV}\cdot\text{s}}{\text{rad}\cdot\text{turn}}$	$147\ \frac{\text{nV}\cdot\text{s}}{\text{rad}\cdot\text{turn}}$
V_o	3.84 V	2.63 V**
R_w	1.92 kΩ	1.95 kΩ†
L_w	76–101 mH	294–310 mH†‡
$P_{out,max}$	947 μW	375 μW♮

* Calculations assume f=667 Hz.
** Measured at 677 Hz. See Fig. 5.17.
† Measured at 1 kHz.
‡ L_w varies depending on θ.
♮ Measured at f=673 Hz, R_{load}=2.72 kΩ.

Table 5.1: Experimental results for millimeter-scale generator .

electrical periods. A noticeable second harmonic is also present, most likely due to the different shapes of the center-connected and edge-connected stator pole faces.

Figure 5.18 shows average power output as a function of load resistance. The plot shows experimental data, as well as a calculated curve based on the measured values in Table 5.1. Because of the frequency variation present in the data, values rescaled to 667 Hz were also plotted, showing the results for constant frequency. The maximum measured power output was 375 μW, achieved at 673 Hz with a load of 2.72 kΩ.

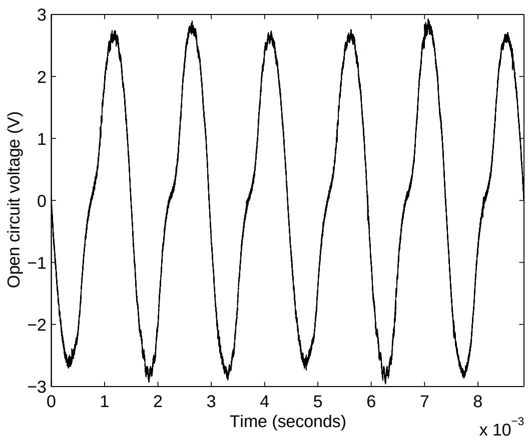

Figure 5.17: Open circuit output voltage, f=677 Hz. Peak voltage is approximately 2.63 V.

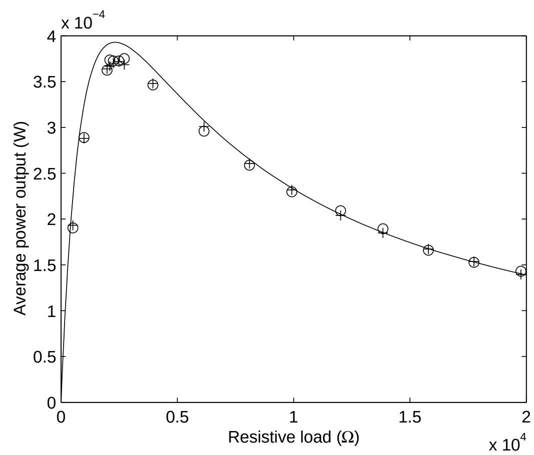

Figure 5.18: Average power output versus load resistance. The circles (○) are measured data points, the plus signs (+) are measured data rescaled to account for frequency variation, and the solid line (—) is the calculated result using the measured values from Table 5.1. The maximum measured power output is 375 μW.

Chapter 6

Machine Design and Analysis — Centimeter Scale

This chapter extends some of the design ideas of Chapter 5 to the macro scale, with focus on a power range of tens to hundreds of Watts. As in Chapter 5, the application of interest is a generator for combustion-based portable power systems, and hence power density is a key metric. However, it should be noted that there are an enormous number of applications over a wide range of power levels — from implantable medical devices to power tools to electric vehicle drives to wind power generation — that would benefit from high-density motor or generator technology. The discussion in this chapter pertains to these applications as well, particularly cases where speed is low, torque is high, and some torque ripple can be tolerated. The first section offers comments on the potential benefits of axial flux machines of the design under consideration.

6.1 Rationale

There is reason to expect that an axial flux machine having circumferential windings and a claw-pole stator structure offers the potential for performance improvements over conventional radial flux machines. Enumerated here are several arguments in favor of such a machine.

- It is generally agreed that axial flux machine configurations achieve higher torque density than conventional radial-flux machine configurations. The study in [51], for example, concluded that axial flux machines with radial stator windings are superior to radial flux designs in terms of power density, moment of inertia, and iron weight, copper weight, and permanent magnet weight per volume. Researchers in [53], meanwhile, find that axial flux machines offer higher specific torque than conventional designs.

  One of the main drawbacks of axial flux machines is their poor use of copper. Because the windings are oriented radially, the copper cross section is limited by the inner diameter of the winding structure. Using the stator proposed in Chapter 5 offers the possibility of an air gap geometry that is similar to many slotted axial flux machine designs, but has dramatically improved winding area.

- The back-emf of an electric machine can be increased by increasing its pole number while holding flux density and speed constant. Total flux linkage per phase remains the same, while the higher pole number translates to a higher electrical frequency, and hence a proportionally higher rate of change of flux linkage and back-emf. However, dividing a conventionally wound stator into a larger number of poles requires reducing the available winding area proportionally with pole number, as well as increasing winding length proportionally. Thus winding resistance increases as the square of the pole number. Consider a rough estimate for the power capability of the machine, taken to be the power delivered to a resistive load matched to the winding resistance, at speeds where winding impedance is primarily resistive:

$$P = \frac{V_{bemf}^2}{4R}. \tag{6.1}$$

It is clear that because back-emf voltage increases with pole number, and winding resistance increases as the square of the pole number, power remains constant over pole number.

Note that the circumferential current configuration, in common with transverse flux machines, has constant winding resistance as pole number changes. Thus over some range of pole numbers, power output should scale linearly with pole number. Of course at higher pole numbers core loss and loss in drive electronics increase to unacceptable levels, small pole pitch relative to gap length reduces pole interaction between rotor and stator, and large leakage inductance in the stator windings can reduce the machine's power factor.

- An axial flux machine with circumferential windings has advantages over radial flux machines in decoupling some geometric parameters. The rotor's area can be increased, for example, without increasing the stator winding length. The axial dimensions of the rotor and stator can be chosen independently, allowing almost arbitrarily large copper cross section for a fixed rotor and gap size. And the volume of permanent magnet in the rotor can be adjusted by changing the rotor height, without modifying the stator.

6.2 Design

The machine described in Chapter 5 has several advantageous features, as detailed in the previous section: a simple winding with large cross-section; torque that scales with pole number while winding resistance stays fixed; and a geometry that decouples some of the design constraints of a conventional machine. Further, some of the drawbacks of the machine — in particular the homopolar stator, restriction to six poles, and fixed rotor diameter — are artifacts of the machine's integration with the Wankel engine. Thus it is possible, in designing a stand-alone machine at the macro-scale, to improve upon the millimeter-scale design.

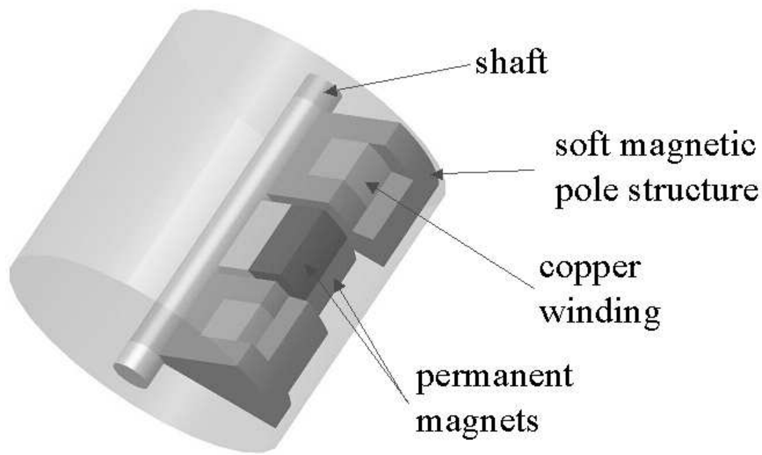

Figure 6.1: Macro-scale generator design concept.

Figure 6.1 shows a conceptual view of a possible macro-scale design. The combination of a fixed permanent magnet in the stator and soft magnetic poles in the rotor has been replaced by a permanent magnet rotor. This allows for reversing rather than homopolar flux in the stator structure, increasing the magnitude of AC flux linking the winding by at least a factor of two, and eliminating the sensitivity of the output to the permanent magnet excitation level. A second phase has also been added by duplicating the stator structure on the other side of the rotor, with a rotation of 90 electrical degrees (i.e. one half pole pitch). In addition to increasing the power output, adding a second phase provides smoother torque than a single-phase design, allows control of rotation direction in motoring operation, and reduces the net axial forces experienced by the rotor. And finally, a shaft is necessary as the rotor is no longer supported by the housing as it was at the smaller scale.

6.2.1 Stator

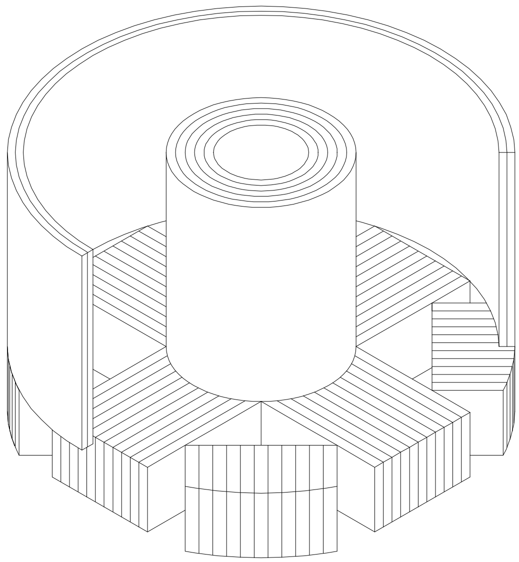

Figure 6.2: Macro-scale generator stator detail.

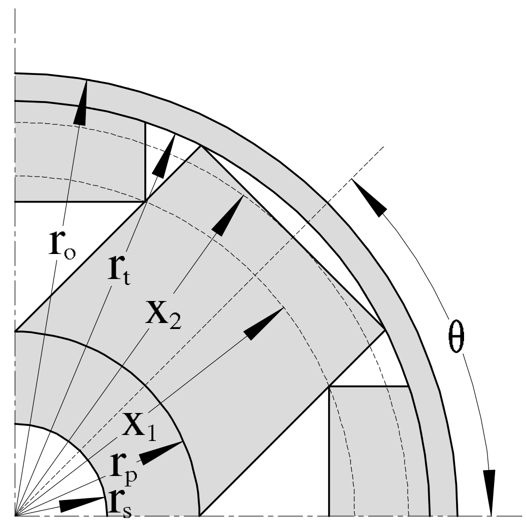

Figure 6.3: Macro-scale generator pole face configuration.

The design described here assumes the use of silicon-steel laminations for the majority of the stator structure. Other materials, notably powdered iron or ferrites, are also candidates, but each material comes with unique drawbacks (see Ch. 2). A decision was made to pursue a design primarily made from silicon steel, but this is by no means the only solution. Silicon steel has excellent magnetic properties, but is difficult to form into three-dimensional laminated structures. This results in some geometric restrictions on the design of the stator. A more detailed view of one half of the proposed stator is shown in Fig. 6.2. The construction uses two tape-wound silicon steel cylinders for the center post and outer toroid, laminated rectangular stacks oriented radially for the pole faces, and a piece of powdered iron for the back-iron. The stator pole faces presented to the gap are rectangular, with wedge-shaped slots between them; hence the slot width varies with radius. Furthermore, the poles are only interdigitated over a fraction of their length, such that the active area (range of radius shared by all pole faces) is limited. Figure 6.3 shows the stator pole faces and their related dimensions. Equations 6.2-6.4 give the relations between the pole face dimensions.

$$\theta = \tfrac{2\pi}{P} \tag{6.2}$$

$$x_1 = 2r_p \cos\left(\tfrac{\theta}{2}\right) \tag{6.3}$$

$$x_2 = (r_t^2 - r_p^2 \sin^2(\theta))^{\frac{1}{2}} \tag{6.4}$$

A significant change to the stator from the design in Ch. 5 is the introduction of an axially oriented through-hole for the rotor shaft. This hole runs the length of the stator center post, using area that would otherwise have been devoted to carrying magnetic flux. Thus the outer diameter of the center post (and hence the inner diameter of the winding) must increase somewhat.

6.2.2 Rotor

There are three main possibilities for the configuration of a permanent magnet rotor: surface magnets; embedded magnets; and the Halbach array. (Some minor variations on the first two can be found in [75].) A surface magnet rotor for an axial flux machine is shown in Fig. 6.4. The structure is shown as a linear actuator, but it can be considered as a circumferential slice of the machine in Fig. 6.1. The magnets are oriented in the axial direction, with alternating polarity. Note that this configuration requires no soft magnetic material in the rotor. Figure 6.5 shows an embedded magnet design. The magnets are oriented with alternating polarity in the circumferential direction, with soft magnetic pieces interposed to direct the flux axially. Because the cross-sectional area of the magnets can be large compared to the pole face area that the soft magnetic section presents to the gap, this is sometimes called a "flux-concentrating" design. This structure can improve the performance of low energy product magnets by utilizing a greater magnet area. The Halbach array [78] orients a series of magnets such that flux cancels on one side of the array, and adds on the other. For large numbers of segments per pole, with magnetization vectors varying in orientation accordingly, the flux pattern on the additive side approaches sinusoidal. Because of the one-sided nature of the field, two back-to-back arrays would be used for a two-phase generator design, as shown in Fig. 6.6.

To compare the fields produced by these three configurations, a two-dimensional finite-element analysis was performed for each using a generic slotless stator. For the surface and embedded magnet rotors, the proportion of the rotor occupied by permanent magnet was varied, while for the Halbach design magnet dimensions are fixed. The flux density in the middle of the gap for these geometries is plotted for each design in Figs. 6.7-6.9.

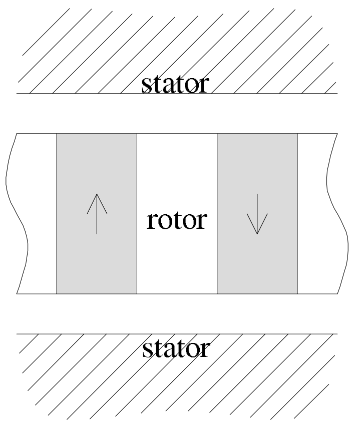

Figure 6.4: Surface magnet rotor.

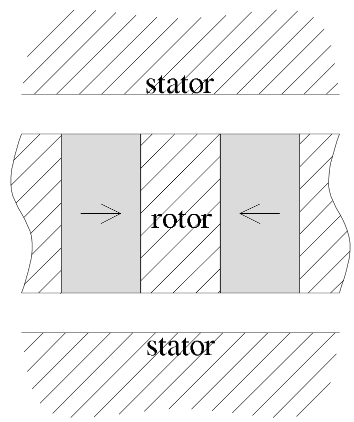

Figure 6.5: Embedded magnet rotor.

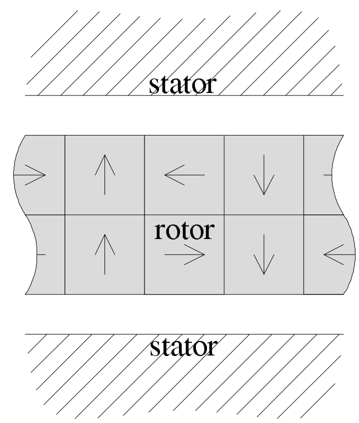

Figure 6.6: Back-to-back Halbach array rotor.

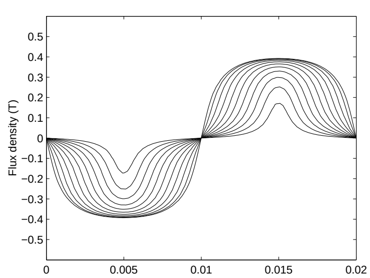

Figure 6.7: Gap flux density for surface magnet rotor.

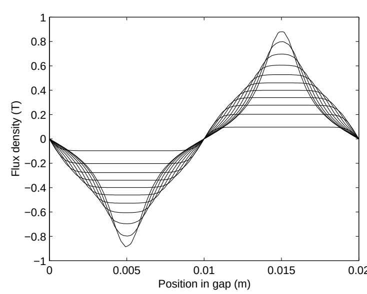

Figure 6.8: Gap flux density for embedded magnet rotor.

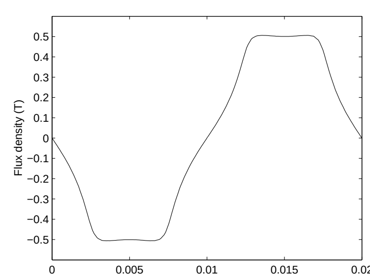

Figure 6.9: Gap flux density for Halbach array rotor.

For the surface magnet configuration in Fig. 6.7, the width of the high-flux portion of the gap grows along with the magnet width, as expected, and the magnitude of the flux density approaches that of an infinitely wide magnet, which is set by the ratio of the magnet and gap lengths. Of the three designs, the surface magnet configuration is perhaps the easiest to build, but offers the lowest flux densities.

The embedded magnet configuration in Fig. 6.8 shows a different trend. As the magnet gets wider and occupies more of the rotor, the soft magnetic pole that directs the flux into the gap gets narrower. Thus the extent of the high-flux portion of the gap gets narrower, but the peak flux density rises sharply as more flux is squeezed into a smaller area. The embedded magnet configuration can achieve high flux density, but only over a narrow area, and is perhaps more difficult to construct than a surface magnet design. Note also that the surface magnet configuration places the magnets in series, in the sense that flux lines must pass through both magnets, while the embedded configuration places them in parallel.

The rotor in the case of the Halbach configuration, shown in Fig. 6.9, is made entirely of equal width magnets, and so there is only a single curve. This design offers higher flux density than the surface magnet design over a wider range than the embedded magnet design. However, it is difficult to assemble and uses more magnet material, while only offering a marginal improvement in performance for this application. Hence the embedded magnet rotor was selected for use in the generator, as a compromise between performance and ease of construction.

6.3 Analysis

This section applies the analysis techniques presented in Chapter 4 to the proposed machine design. The approach is to begin with a lumped-element magnetic circuit model as in Sec. 4.2, and then apply energy method type analysis to compute torque as in Sec. 4.3. An optimization using Monte Carlo techniques is used to choose machine dimensions. Finite-element analysis is also applied as in Sec. 4.4 as a verification of the magnetic circuit analysis.

6.3.1 Lumped-Element Model

The magnetic structure that forms the basis of the lumped element modeling is shown in Fig. 6.10. Note that although the figure has been "unwrapped" to a linear rather than rotational actuator as well as "flattened" to a 2-D structure, it is unchanged magnetically from a qualitative standpoint. The equivalent magnetic circuit is shown in Fig. 6.11. Reluctances R_1 through R_8 represent the air gap between various rotor and stator poles, R_y models the leakage path between adjacent stator teeth, and R_z models soft magnetic reluctances in the stator. The permanent magnet is modeled by an MMF source i_{pm} and series reluctance R_v. Because of the periodic nature of the structure, the two permanent magnets and four windings shown in Fig. 6.10 can be represented in Fig. 6.11 by a single permanent magnet source and one winding for each phase. Thus the circuit applies for any number of pole pairs provided the component values are scaled appropriately.

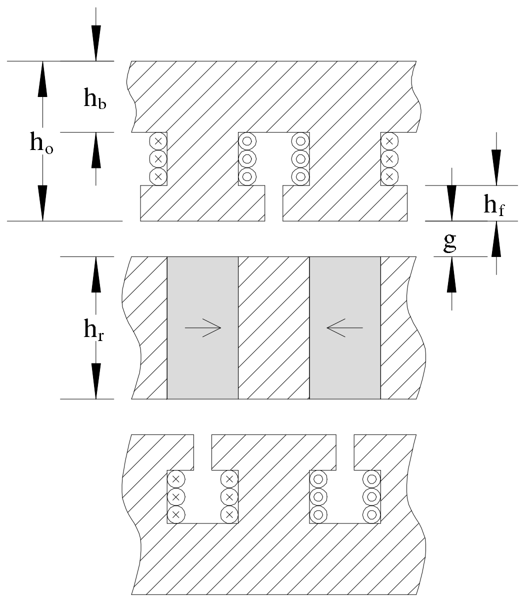

Figure 6.10: Conceptual magnetic structure for modeling of macro-scale generator.

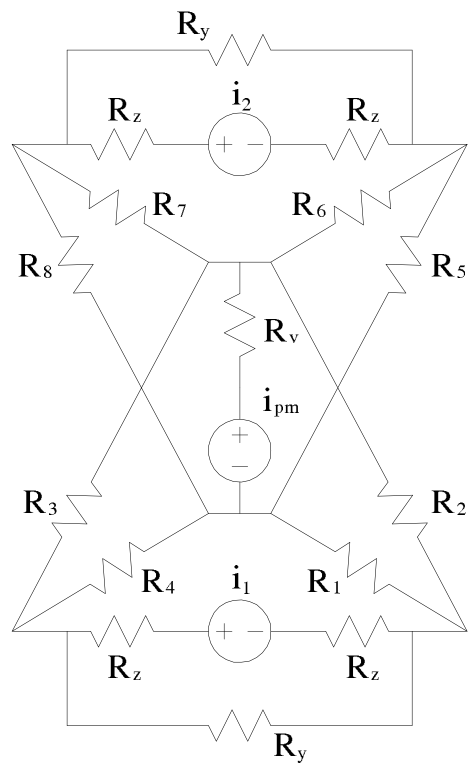

Figure 6.11: Magnetic circuit model.

Circuit equations associated with Fig. 6.11 are included in Sec. A.1. Equations A.1-A.4 can be used to solve for the fluxes in the circuit in closed-form, although the resulting expressions would be somewhat intractable due to the large number of circuit elements. However, given the geometry of the structure and values for phase currents and permanent magnet excitation, Eqs. A.1-A.4 are useful in solving for fluxes, and hence coenergy and force, numerically.

There are two approximations that limit the accuracy of the lumped-element model. The first is the use of constant magnetic permeability in the soft magnetic elements (i.e. the neglect of saturation effects). Although saturation effects could be included in the lumped element model, the resulting increase in the solution time would be undesirable for use with Monte Carlo optimization (see Section 6.3.2) that may require many iterations. The effect of saturation is to reduce the permeability of soft magnetic material, increasing the reluctance of the intended flux path, reducing the amount of flux crossing the gap, and encouraging flux to follow unintended leakage paths. This is a particular problem for powdered-iron material, which has low permeability even in the unsaturated state (see App. B). For designs that are anticipated to have high flux densities, approximate saturated permeabilities are used rather than the unsaturated values; this avoids a naïvely optimistic result.

The second approximation is the use of a "small-gap" reluctance model, where the length of the air gap is assumed to be small compared to the pole pitch. Under this approximation, magnetic field lines remain parallel as they cross the air gap, and the gap reluctance is well characterized by the gap length and area. However, for high numbers of poles, pole pitch begins to approach gap length, and the lumped element model above ceases to be a good approximation. The accuracy of the lumped-element model could be improved through the use of two-dimensional approximation techniques such as those found in in [79] or [80], although the added complexity is perhaps not worth the effort except for extremely simple magnetic structures.

6.3.2 Monte Carlo Optimization

A Monte Carlo method similar to the approach in [81, 82] was used to generate a set of optimal designs for the lumped element model of Section 6.3.1. Under this method, six design parameters are randomly chosen from a prespecified range: pole number; overall radius; center post radius; pole face height; back-iron height; and winding current. Overall volume, rotor height, shaft radius, and gap height are held constant. These values are given in Tab. 6.1. The code then computes fluxes and torque from the magnetic circuit model, and checks that the result is feasible (i.e. does not have nonphysical dimensions and does not exceed saturation limits). If a particular design is not feasible, it is discarded and another iteration begins. Mechanical power is then estimated by taking the peak of the fundamental component of the torque versus angular displacement curve, and multiplying by the mechanical frequency in radians per second:

$$P_{mech} = \max(|\tau_1|)\omega_{mech}. \tag{6.5}$$

Fixed Values	
Volume of half stator	45×10^{-6} m^3
Shaft radius (r_s)	3 mm
Gap length (g)	0.25 mm
Rotor height (h_r)	5 mm
Fraction of rotor occupied by magnet	0.55
Mechanical rotor speed	10 krpm
Parameter Ranges	
Pole number	6–18
Outer radius (r_o)	12–42 mm
Center post to outer radius ratio (r_p/r_o)	0.20–0.45
Pole face height to total height ratio (h_f/h_o)	0.03–0.35
Back-iron height to total height ratio (h_b/h_o)	0.10–0.50
Winding current	100–700 A·t

Table 6.1: Fixed values and parameter ranges for Monte Carlo optimization. Dimensions are defined in Figs. 6.3 and 6.10.

Core losses are calculated according to the loss functions for each material, using the electrical frequency and peak flux density:

$$P_{fe} = F(|B_{peak}|, f_{elec}). \tag{6.6}$$

The loss functions F for Arnon 5 and Micrometals -26 are given in Sec. 2.3.2. Copper losses are calculated as

$$P_{cu} = I^2 R, \tag{6.7}$$

where R is the winding resistance calculated from the geometry, resistivity of copper, and an assumed winding packing factor, and I is the amplitude of a square-wave current. Finally, efficiency is calculated:

$$\eta = \frac{(P_{mech} - P_{cu} - P_{fe})}{P_{mech}}. \tag{6.8}$$

Assuming a design has met the feasibility criteria, its power output and efficiency are compared with a list of existing "good" designs that have been saved from previous iterations. If the new design is worse than any individual existing design along both the power output and efficiency axes, it is discarded. If the new design is superior to all other designs along at least one of the two axes, it is saved. If the new design is saved, any existing designs that are worse than the new design along both axes are discarded.

In this way, over many iterations, a list of quasi-optimal designs is generated which gives a near-maximum efficiency over a range of power output values, or equivalently a near-maximum power output over a range of efficiency values. Figure 6.12 shows a plot of the designs generated using the values in Tab. 6.1. Because the process is random, designs are not truly optimal — there is a possibility that a design in the list may be rendered obsolete by a future iteration. However with a sufficient number of iterations the list can approach the truly optimum curve arbitrarily closely. Note that not all the points in Fig. 6.12 represent practical continuous operating points. At high power levels, the machine's continuous operation may be limited by the dissipation of heat generated by iron and copper loss. The points in the figure indicated by circles are acceptable continuous operating points from a thermal point of view, having a loss to surface area ratio of less than 3000 W/m^2. A MATLAB script that performs the optimization described above is included in Section C.2.

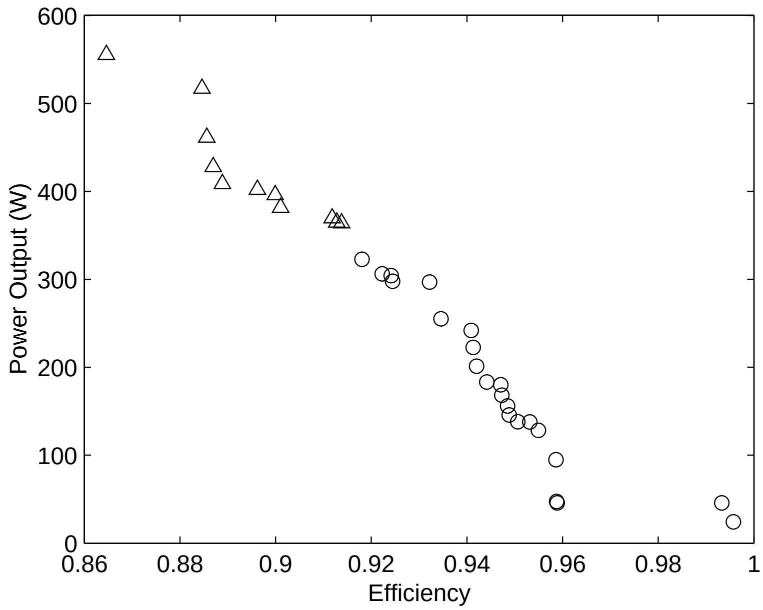

Figure 6.12: Monte Carlo optimization results, showing power output and efficiency for various geometries. Circles represent solutions that meet thermal criteria.

A benefit of this approach is the ability to observe trends in the relations between various parameters in the list of quasi-optimal designs. For example, Figs. 6.13 and 6.14 plot of overall radius versus power output and efficiency, respectively. Clearly, flatter machines (i.e. those with a large ratio of radius to axial length) tend to produce more power at lower efficiency. Of course without a deterministic expressions for power output and efficiency, other types of analysis must be used to determine why this is the case.

The great disadvantage of the Monte Carlo approach is the large number of iterations required. For six design parameters, a six-dimensional space must be filled with a sufficient density of points to ensure proximity to the optimal result. Setting tight bounds on the range that each parameter is drawn from can reduce the size of this

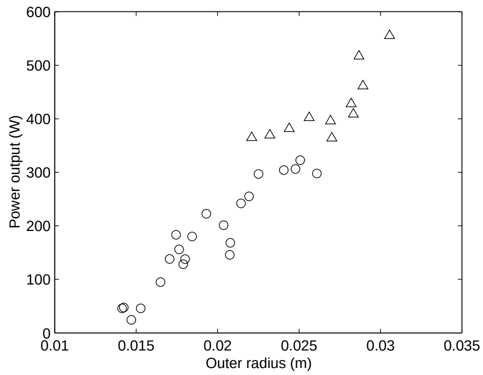

Figure 6.13: Power output versus outer radius for quasi-optimal designs.

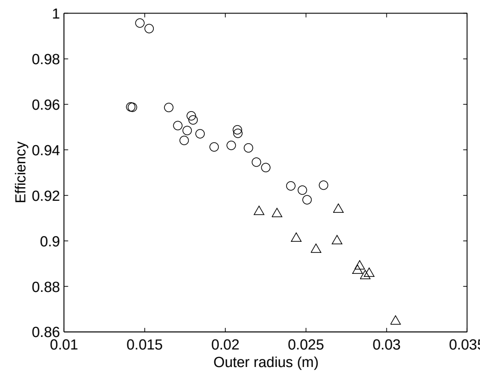

Figure 6.14: Efficiency versus outer radius for quasi-optimal designs.

space, and hence the run-time of the program, at the expense of searching a smaller design space. This problem is addressed in [82], in which the parameter ranges are dynamically adjusted according to a statistical analysis of the existing results. A simpler method, used in this work, is to run the optimization for a moderate number of iterations, view a histogram of each random variable in the saved solutions, adjust the variable's range accordingly, and restart the optimization. Figures 6.12-6.14 are the result of approximately 100,000 Monte Carlo iterations.

The data point in Fig. 6.12 with the highest continuous power output among the thermally acceptable results was selected as the most promising candidate design. The geometry and operating point values for this design are given in Tab. 6.2. Table 6.3 gives the calculated performance for this machine. Note that the power density of the machine compares favorably to the designs in Tab. 3.2. However, due to the approximations described in Sec. 6.3.1, a confirmation of these results is desirable.

P	10
r_o	25.1 mm
r_p	9.8 mm
h_f	4.0 mm
h_b	7.7 mm
I_w	405 A·t

Table 6.2: Design values chosen from Monte Carlo optimization results.

P_{out}	323 W
P_{cu}	7.7 W
P_{core}	21.1 W
η	0.92
P'	3.2×10^6 W/m^3

Table 6.3: Machine performance calculated from magnetic circuit results.

Finite-element analysis can be employed for this purpose, as described in the next section.

6.3.3 Finite-Element Analysis

Finite-element analysis, as described in Sec. 4.4, was applied to the two-dimensional model shown in Fig. 6.15, which is qualitatively equivalent to Fig. 6.10. As in Fig. 6.10, this structure represents two poles of a circumferential cross-section of the machine taken at a particular radius. The commercial finite-element software package FEMLAB was used to obtain the solution.

As compared to lumped-element analysis, finite-element analysis captures more closely the effects of realistic field geometries. Further, the soft magnetic portions of the model include the saturation effects described in Sec. 2.1. This is accomplished by defining the magnetic permeability of these regions of the model with a saturating function of flux density, given by

$$\mu_r(B) = \frac{\hat{\mu_r}}{C|B|^2 + 1} + 1. \tag{6.9}$$

For silicon steel $\hat{\mu_r}$=1000, while for powdered iron material $\hat{\mu_r}$=75; for both materials, C=25. (Information on magnetic material properties can be found in App. B.) The use of nonlinear materials complicates somewhat the calculation of coenergy density within the material. Rather than a linear calculation based only on the (B,H) operating point, the integral of Eq. 4.38 must be carried out over the particular B,H trajectory taken to reach the operating point. Equation 6.9 defines this trajectory — details of how the integration is carried out can be found in Sec. A.3.

A two-dimensional finite-element model was selected due to the extreme computational requirements a three-dimensional model would impose. The machine under consideration, however, has features that are not uniform in the radial direction. For example, a true circumferential cross-section of the machine at the radii of interest has no pole teeth — only pole faces appear, because the vertical pole tooth structure is confined to the radii of the center post and toroid. Magnetically, however, there must be a low-permeability path in the two-dimensional model that allows the flux to link the winding. This is handled by inserting a vertical member that has the same reluctance as the true three dimensional path.

Consider a reluctance $R_o = \frac{\ell_o}{\mu_o \mu_r A_o}$, in which ℓ_o and A_o reflect the actual dimensions of the machine, and μ_r the actual material's relative permeability. Then suppose that for the purposes of modeling the area must be scaled by a factor $0 < \mathrm{S} < 1$. Clearly, to achieve the same reluctance, the permeability can be scaled by $\frac{1}{\mathrm{S}}$. The length could also be scaled, but it is desirable to maintain as much as possible of the original geometry. For nonlinear materials, a further issue arises. Assume the reduced-area model reluctance is to carry the same flux as its real-world counterpart. Because it has a smaller area, its flux density will be higher, with the result that permeability will begin to decrease earlier than it should. Hence the flux density must also be corrected, by scaling B by a factor S. A rescaled version of Eq. 6.9, for a model with area scaled by S, is thus

$$\mu_r(B) = \frac{1}{S}\left(\frac{\hat{\mu_r}}{C|SB|^2+1}+1\right). \tag{6.10}$$

Another three-dimensional feature of the geometry is the slot between stator poles. As can be seen from Fig. 6.3, the width of the slot is a function of radius. To account for this variation, a full torque versus displacement curve was calculated at each of three different radii. A second-order polynomial was then fit to the results in the radial direction, and integration carried out to attempt to capture more accurately the torque over the useful range of radii. Details of this procedure can be found in Sec. A.2.

A 2-D finite-element model was created for the candidate design, using the dimensions and current in Tab. 6.2. Square wave currents were assumed, with all windings carrying the same magnitude current. Figure 6.16 shows the FEA solution for the displacement where the rotor is aligned with the stator. Qualitatively it is apparent from the figure how the field differs from the lumped-element "small-gap" approximation. A more quantitative comparison is given by Fig. 6.17, in which the flux linkage of one phase winding is shown for both the lumped-element and finite-element models. The

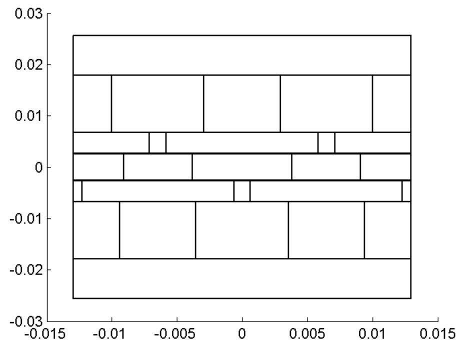

Figure 6.15: Finite-element model of macro-scale generator.

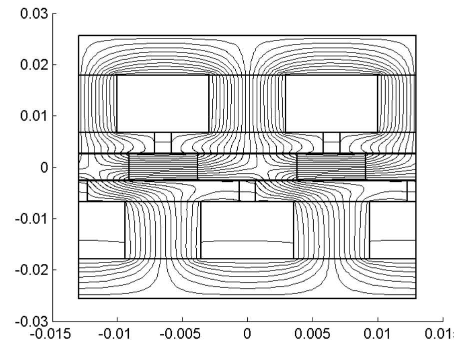

Figure 6.16: Typical finite-element solution.

peak flux linkage differs by about 40%, and while the qualitative shapes are similar, the FEA result has smoother transitions between various geometry configurations.

Figure 6.18 shows the coenergy computed for the magnetic circuit and FEA models. Note that the waveforms are similar, but differ by a constant, as in Sec. 4.5.4. Figure 6.19 shows the torque versus angular displacement results for the magnetic circuit model and FEA, using the dimensions given in Tab. 6.2. The magnetic circuit model result is represented by dots ($\cdot$); more points are plotted for this solution as points can be computed relatively quickly. The FEA, on the other hand, is time consuming and hence points are more sparse. The FEA solution is represented by circles ($\circ$). The curves agree to a good approximation over most of their useful range. The large deviation in the neighborhood of the unstable equilibrium point is the result of differentiating the unrealistically sharp coenergy waveform produced by the magnetic circuit analysis.

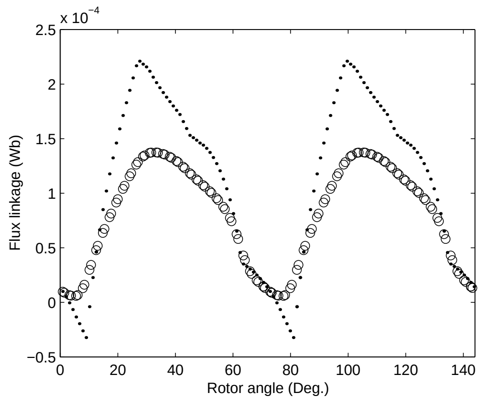

Figure 6.17: Flux linkage versus rotor angle calculated from magnetic circuit (dots) and finite-element analysis (circles).

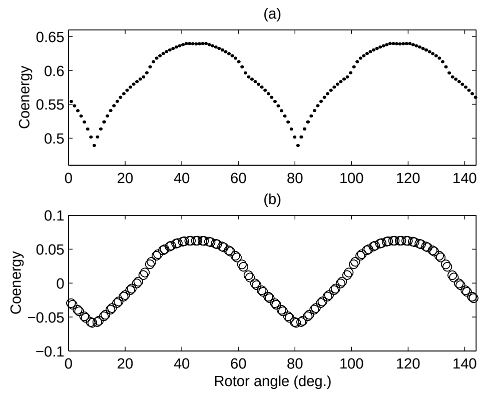

Figure 6.18: Coenergy versus rotor angle calculated from magnetic circuit (a) and finite-element analysis (b). Note that the range of the vertical axis is the same in both plots.

The agreement of the two results in Fig. 6.19 increases confidence in the results of the lumped element model. If the power density of 3.2×10^6 W/m^3 given in Tab. 6.3 were to be achieved, the optimal machine design resulting from the Monte Carlo optimization would in fact be the second best of those listed in Tab. 3.2, while having superior efficiency. Further, the machine presented here was designed for lower speeds than the better machines in the table, placing it at a disadvantage in terms of power; higher power levels could be attained by designing for higher speeds. Nonetheless, given the numerous advantages attributed to the design in Sec. 6.1, this result is somewhat less than expected.

A major drawback of the design presented in this chapter is the use of silicon steel laminations; while their magnetic properties are favorable, the geometric constraints they imposed were excessive. The active area of the machine was limited to radii

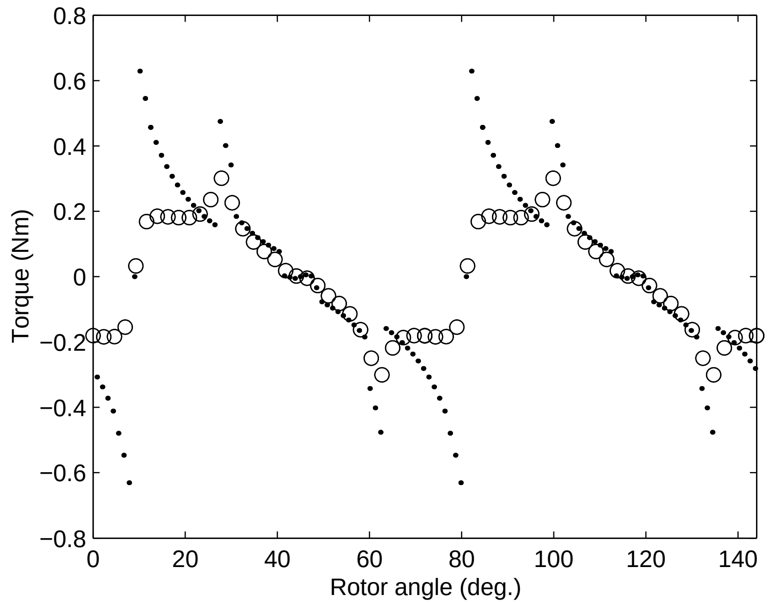

Figure 6.19: Torque versus rotor angle, calculated with magnetic circuit (dots) and finite-element analysis (circles).

between x_1 and x_2 (as shown in Fig. 6.3, with varying stator slot size. The shape of the stator poles, having a rectangular cross-section, was also problematic. An ideal design would have tapered the pole faces to reduce leakage inductance. Further conclusions are offered in the next chapter.

Chapter 7

Conclusions

Efficient and dense electromechanical energy conversion is a key component of many proposed portable power systems. Further, applications for such systems are numerous and growing. Two designs were presented for generators having axial flux and circumferential windings. Although their size and application requirements differ somewhat, the two machines have many common elements. This chapter offers reflections and conclusions drawn from these two design efforts, as well as an outline for future research.

7.1 Thoughts on Millimeter-Scale Design

Because the millimeter-scale design was intended to interact with a planar MEMS internal combustion engine, many design choices were guided by the engine configuration. The integrated design of the engine and generator, while novel, was a limitation on both devices. A permanent magnet rotor would have been the most appropriate choice, but temperature constraints made this impractical. The simpler option of soft magnetic poles nonetheless complicated the silicon rotor fabrication, while the size and shape of the rotor constrained the soft magnetic material to a sub-optimal configuration.

Although the two devices were never tested together, there was a potential mismatch in sizing between the engine and generator in terms of power output. Integration again constrained the two designs, such that the calculated maximum input power of the generator was less than the calculated output power of the engine [26]. Interestingly, the generator power ideally increases as the fourth power of a uniform scaling factor (see Eq. 3.10), while the engine scales as the third power; in theory there is an appropriate size where an integrated engine-generator design matches the power of the two machines.

The homopolar flux configuration of the stator introduced two problems. The first was large flux leakage in the non-aligned rotor position, which reduced the magnitude of the AC flux linking the stator winding. The second was stator saturation, which was experimentally demonstrated to reduce the power output of the machine. Thus great care must be taken to find the optimal flux level. A design with a permanent magnet rotor, such as in Ch. 6, has fully reversing flux, and hence should be able to increase the AC flux linkage by at least of factor of two.

Machining of powdered iron proved to be problematic. The materials tested were brittle and inhomogenous, resulting in frequent fractures when machining small parts. Sharp tools, high cutting speeds, and sacrificial supporting jigs mitigate this problem somewhat, but it may be preferable to have parts pressed from molds.

The powdered iron also proved to be undesirable magnetically. The low permeability of the material required that key portions of the stator (i.e. the center post and toroid, which carry the highest flux densities) be made from silicon steel.

7.2 Thoughts on Centimeter-Scale Design

The design process described in Chapter 6 is iterative, because none of the analyses available are appropriate for the entire problem. Magnetic circuit techniques are fast but make substantial approximations, while finite-element techniques can be more accurate but are often too slow for use in optimization problems that require many solution iterations. Thus the approach was to develop a first-pass optimal design with magnetic circuit techniques, and use FEA to verify its performance and fine-tune calculations.

The resulting machine is calculated to have 323 W maximum continuous power output at just under 92% efficiency, with a power density of 3.2×10^6 W/m^3. This places the design among some of the better machines in Table 3.2. The design speed was relatively low, indicating that further gains could be realized by designing for higher speeds. On the other hand, the calculated performance, particularly core loss, may prove to be optimistic; this can only be verified by experimentation.

An issue that is left unresolved is the true upper bound on the performance of such a machine. Basic calculations indicate that torque should scale with pole number. Of course, higher pole numbers demand higher electrical frequencies, and at a certain point core losses will be excessive. There is also a practical limitation on pole number imposed by the gap length — when the pole pitch becomes small, flux no longer crosses the gap. It is not clear from the Monte Carlo result which of these effects is primarily responsible for limiting the pole number of the optimal designs.

Nontheless, the factors that negatively impact performance are practical, not fundamental. Smaller gaps, low loss materials, and careful design to minimize winding inductance could provide further performance increases. It is also possible that some of the design ideas presented here could be useful in MEMS applications, where gaps can be smaller, allowing larger numbers of poles. Microfabrication also offers different material and fabrication choices, which may resolve the conflict between silicon steel and powdered iron.

7.3 Thoughts on Future Research Directions

As noted in Chapter 6, the axial-flux circumferential current machine has potential to improve on the power density of conventional machines. However, as was also shown, obstacles exist that degrade the performance of the design. Suggestions for future research are presented below.

7.3.1 Isotropic Materials

The use of silicon steel laminations for the design in Chapter 6, while providing for good magnetic properties, may have introduced excessive limitations on geometry. A larger effective stator pole area, for example, might be obtained through the use of an isotropic material. Such a material would also allow the leakage between stator poles to be minimized by tapering and otherwise shaping the poles. Indeed, with isotropic materials, the design space becomes much larger, and more opportunities arise for improved performance.

However, a larger design space also implies greater difficulty in finding an optimum design. Further, available isotropic materials have poor magnetic properties. Thus the greater losses and low permeability of powdered iron materials may offset the advantages of its isotropic nature. A similar challenge comes from the low saturation flux density of ferrite material.

7.3.2 Small Gap, Low Speed Machine

If the machine design is freed from the speed constraints of a particular application, core loss no longer places a limit on pole number — the machine can simply be run at a speed where core losses are acceptable, including DC if necessary. The design problem is then that of maximizing torque rather than power, and the optimal pole number and hence maximum torque is determined by the gap length. Hence the challenge is mainly the mechanical issue of constructing a machine with an extremely small gap.

The research effort would consist of optimization of the magnetic structure with gap length as a parameter, such that the relationship between optimal pole number and gap length is well characterized. This would be followed by careful thermal analysis and mechanical design, perhaps utilizing novel machining and assembly techniques to meet tight tolerances, or creating novel structures having compliance for thermal expansion while still maintaining gap spacing.

7.3.3 Materials and Manufacturing

The material options that currently exist for complex three-dimensional magnetic structures are poor. Isotropic materials such as powdered iron or ferrites carry penalties in magnetic performance, while silicon steel laminations are difficult to form into the required geometries.

There are several diverse avenues for addressing this problem. A straightforward approach may be to examine hybrid structures, that make use of multiple types of material depending on the particular requirements. This was done in both Ch. 5 and Ch. 6, in which silicon steel was used for high-saturation components while powdered iron was used in components that required isotropic properties.

An alternative approach might be to investigate methods of producing three-dimensional structures from silicon steel laminations, utilizing complex cut and folded shapes. Finally, a risky approach to the problem might attempt to produce better magnetic materials, perhaps via novel electroplating processes. This would require significant innovation, however, and may not be feasible on a large scale.

Bibliography

[1] (2005) Phonescoop. Database of mobile phone information. Phone Factor, LLC. [Online]. Available: http://www.phonescoop.com

[2] (2005) Cellphone battery warehouse. Product Catalog. Cellphone Battery Warehouse, LLC. [Online]. Available: http://www.batteries4less.com

[3] (2005) Dell. Product Catalog. Dell, Inc. [Online]. Available: http://www.dell.com

[4] (2005) 4allbatteries.com. Product Catalog. 4 All Batteries. [Online]. Available: http://www.4allbatteries.com

[5] "Statistical review – business appliances," Appliance, Gartner Group, 2004.

[6] J. Haughey, "Is technology adoption quickening?" Electronic Business, International Telecom Union, p. 16, Aug. 2004.

[7] Committee on Electric Power for the Dismounted Soldier, "Energy–efficient technologies for the dismounted soldier," Technical report, National Research Council, 1997.

[8] P. Flynn *et al*, "Meeting the energy needs of future warriors," Technical Report, National Research Council, 2004.

[9] N. Lewis *et al*, "Portable energy for the dismounted soldier," Technical Report, The MITRE Corporation, 2003.

[10] A. Patil, "U.S. Army CERDEC fuel cell technology," presented at Science at the Leading Edge (170th Annual Meeting of the AAAS). American Association for the Advancement of Science, Feb. 2004.

[11] J. Jansen *et al*, "Exoskeleton for soldier enhancement systems feasibility study," Technical report, Oak Ridge National Laboratory, 2000.

[12] J. Grasmeyer and M. Keennon, "Development of the black widow micro air vehicle," presented at the 39th Aerospace Sciences Meeting and Exhibit. American Institute of Aeronautics and Astronautics, Inc., 2001, paper AIAA-2001-0127.

[13] (2004) Epson announces advanced model of the world's lightest micro-flying robot. Press Release. Seiko Epson Corp. [Online]. Available: http://www.epson.co.jp/e/newsroom/news_2004_08_18.htm

[14] M. Woods, J. Henderson, and G. Lock, "Energy requirements for the flight of micro air vehicles," *The Aeronautical Journal*, vol. 105, no. 1045, pp. 135–149, March 2001.

[15] J. Hill, M. Horton, R. Kling, and L. Krishnamurthy, "The platforms enabling wireless sensor networks," *Communications of the ACM*, vol. 47, no. 6, pp. 41–6, June 2004.

[16] S. Roundy, D. Steingart, L. Frechette, P. Wright, and J. Rabaey, "Power sources for wireless sensor networks," in *Wireless Sensor Networks, First European Workshop*. Springer-Verlag, 2004, pp. 1–17.

[17] P. Krein, "The power of forever: managing the ultimate in long-term energy needs of spacecraft and other remote systems," Power and energy seminar presentation, University of Illinois at Urbana-Champaign, Oct. 2004.

[18] P. Glynne-Jones, M. Tudor, S. Beeby, and N. White, "An electromagnetic, vibration-powered generator for intelligent sensor systems," *Sensors and Acutators, A: Physical*, vol. 110, no. 1-3, pp. 344–9, Feb. 2004.

[19] S. Roundy, P. Wright, and K. Pister, "Micro-electrostatic vibration-to-electricity converters," in *2002 AMSE International Mechanical Engineering Congress and Exposition*. ASME, Nov. 2002, pp. 487–96.

[20] S. Roundy, P. Wright, and J. Rabaey, "A study of low level vibrations as a power source for wireless sensor nodes," *Computer Communications*, vol. 26, no. 11, pp. 1131–44.

[21] T. R. Crompton, *Battery Reference Book*. Reed Educational and Professional Publishing, 2000.

[22] E. Jonietz, "Ant power packs," Technology Review, Sept. 2004.

[23] Y. Zhu, S. Ha, and R. Masel, "High power density direct formic acid fuel cells," *Journal of Power Sources*, vol. 130, no. 1-2, pp. 8–14, May 2004.

[24] A. C. Fernandez-Pello, "Micropower generation using combustion: issues and approaches," in *Twenty-ninth International Symposium on Combustion*, vol. 29. Proceedings of the Combustion Institute, 2002, pp. 883–98.

[25] A. H. Epstein *et al*, "Power MEMS and microengines," in *1997 International Conference on Solid–State Sensors and Actuators (TRANSDUCERS '97)*, vol. 2. IEEE, 1997, pp. 753–6.

[26] A. J. Knobloch, "Ultra–deep reactive ion etching for silicon wankel internal combustion engines," Ph.D. dissertation, University of California, Berkeley, 2003.

[27] A. J. Knobloch, M. Wasilik, C. Fernandez-Pello, and A. P. Pisano, "Micro internal-combustion engine fabrication with 900 μm deep features via DRIE," in *2003 ASME International Mechanical Engineering Congress*, vol. 5. ASME, Nov. 2003, pp. 115–23.

[28] D. G. Jones and A. P. Pisano, "Fabrication of ultra thick ferromagnetic structures in silicon," in *2004 ASME International Mechanical Engineering Congress and Exposition*. ASME, 2004.

[29] F. C. Martinez, "Apex seal design for the MEMS rotary engine power system," Master's thesis, University of California, Berkeley, 2000.

[30] B. Haendler, "Liquid to vapor phase change in constant cross-section silicon microchannels," Master's thesis, University of California, Berkeley, 2003.

[31] R. Boll, ed., *Soft Magnetic Materials : Fundamentals, Alloys, Properties, Products, Applications*. Heyden, 1979.

[32] R. C. O'Handley, *Modern Magnetic Materials: Principles and Applications*. John Wiley & Sons, Inc., 2000.

[33] R. M. Bozorth, *Ferromagnetism*. American Telephone and Telegraph Company, 1978.

[34] J. F. Gieras and M. Wing, *Permanent Magnet Motor Technology*. Marcel Dekker, Inc., 2002.

[35] E. P. Furlani, *Permanent Magnet and Electromechanical Devices*. Academic Press, 2001.

[36] A. E. Fitzgerald, C. Kingsley, Jr., and S. Umans, *Electric Machinery*. McGraw–Hill, 1990.

[37] (2003) Precision rolled strip & foil. Product catalog. Arnold. [Online]. Available: http://www.arnoldmagnetics.com

[38] (2003) Iron powder cores for power conversion and line filter applications. Product catalog. Micrometals, Inc. [Online]. Available: http://www.micrometals.com

[39] N. Maluf, *An Introduction to Microelectromechanical Systems Engineering*. Artech House, Inc., 2000.

[40] D. P. Arnold, I. Zana, F. Cros, and M. G. Allen, "Vertically laminated magnetic cores by electroplating ni-fe into micromachined si," *IEEE Transactions on Magnetics*, vol. 40, no. 4, pp. 3060–62, July 2004.

[41] T. Budde, M. Föhse, B. Majjer, H. Lüthje, G. Bräuer, and H. H. Gatzen, "An investigation on technologies to fabricate magnetic microcomponents for miniaturized actuator systems," *Microsystem Technologies*, vol. 11, no. 1, pp. 78–84, February 2002.

[42] W. P. Taylor, M. Schneider, H. Baltes, and M. G. Allen, "A NiFeMo electroplating bath for micromachined structures," *Electrochemical and Solid-State Letters*, vol. 2, no. 12, pp. 624–6, December 1999.

[43] N. V. Myung, D.-Y. Park, B.-Y. Yoo, and P. T. A. Sumodjo, "Development of electroplated magnetic materials for MEMS," *Journal of Magnetism and Magnetic Materials*, vol. 265, no. 2, pp. 189–98, September 2003.

[44] H. J. Cho and C. H. Ahn, "Microscale resin-bonded permanent magnets for magnetic micro-electro-mechanical systems applications," *Journal of Applied Physics*, vol. 93, no. 10, pp. 8674–6, May 2003.

[45] L. K. Lagorce, O. Brand, and M. G. Allen, "Magnetic microactuators based on polymer magnets," *IEEE Journal of Microelectromechanical Systems*, vol. 8, no. 1, pp. 2–9, March 1999.

[46] H. J. Cho and C. H. Ahn, "A bidirectional magnetic microactuator using electroplated permanent magnet arrays," *Journal of Microelectromechanical Systems*, vol. 10, no. 3, pp. 237–40, March 2004.

[47] B. Pawlowski, S. Schwarzer, A. Rahmig, and J. Töpfer, "NdFeB thick films prepared by tape casting," *Journal of Magnetism and Magnetic Materials*, vol. 265, no. 3, pp. 337–44, October 2003.

[48] T. Budde and H. H. Gatzen, "Magnetic properties of an SmCo/NiFe system for magnetic microactuators," *Journal of Magnetism and Magnetic Materials*, vol. 272-276, no. 3, pp. 2027–8, May 2004.

[49] J.-C. Shih, H.-H. Hsiao, J.-L. Tsai, and T.-S. Chin, "Low-temperature in-situ growth of high-coercivity Fe-Pt films," *IEEE Transactions on Magnetics*, vol. 37, no. 4, pp. 1280–2, July 2001.

[50] S. Franz, P. Cavallotti, M. Bestetti, V. Sirtori, and L. Lombardi, “Electrodeposition of cobalt platinum alloys micromagnets,” *Journal of Magnetism and Magnetic Materials*, vol. 272-276, no. 3, pp. 2430–1, May 2004.

[51] K. Sitapati and R. Krishnan, “Performance comparisons of radial and axial field, permanent-magnet, brushless machines,” *IEEE Transactions on Industry Applications*, vol. 37, no. 5, pp. 1219–26, Sept./Oct. 2001.

[52] S. Huang, J. Luo, F. Leonardi, and T. A. Lipo, “A comparison of power density for axial flux machines based on general purpose sizing equations,” *IEEE Transactions on Energy Conversion*, vol. 14, no. 2, pp. 185–92, June 1999.

[53] N. B. Şimşir and H. B. Ertan, “A comparison of torque capabilities of axial flux and radial flux type of brushless DC (BLDC) drives for wide speed range applications,” in *1999 International Conference on Power Electronics and Drive Systems (PEDS ’99)*. IEEE, Jul. 1999, pp. 719–24.

[54] W. Arshad, T. Bäckström, and C. Sadarangani, “Analytical design and analysis procedure for a transverse flux machine,” in *International Electric Machines and Drives Conference (IEMDC 2001)*. IEEE, Jun. 2001, pp. 115–21.

[55] P. L. Chapman and P. T. Krein, “Micromotor technology: Electric drive designer’s perspective,” in *Conference Record of the 2001 IEEE Industry Applications Society Annual Meeting*, vol. 3. IEEE, 2001, pp. 1978–83.

[56] J. W. Judy, “Batch–fabricated ferromagnetic microactuators with silicon flexures,” Ph.D. dissertation, University of California, Berkeley, 1996.

[57] (2005) Maxon motors. Product catalog. Maxon Motor A.G. [Online]. Available: http://www.maxonmotor.com

[58] (2005) Faulhaber brushless motors. Product catalog. FAULHABER Group. [Online]. Available: http://www.micromo.com/products

[59] L.-S. Fan, Y.-C. Tai, and R. S. Muller, “IC-processed electrostatic micromotors,” *Sensors and Actuators*, vol. 20, no. 1-2, pp. 41–7, Nov. 1989.

[60] H. Guckel *et al*, “Fabrication and testing of the planar magnetic micromotor,” *Journal of Micromechanics & Microengineering*, vol. 1, no. 3, pp. 135–8, Sept. 1991.

[61] ——, “A first functional current excited planar rotational magnetic micromotor,” in *Micro Electro Mechanical Systems*. IEEE, Feb. 1993, pp. 7–11.

[62] T. Christenson, H. Guckel, and J. Klein, "A variable reluctance stepping microdynamometer," *Microsystem Technologies*, vol. 2, no. 3, pp. 139–43, Aug. 1996.

[63] H. Köşer and F. Cros and M. G. Allen and J. H. Lang, "A high torque density MEMS magnetic induction machine," in *11th International Conference on Solid–State Sensors and Actuators (TRANSDUCERS '01)*, vol. 1. Springer–Verlag, 2001, pp. 284–7.

[64] H. Köşer and J. H. Lang, "Modeling a high power density MEMS magnetic induction machine," in *2001 International Conference on Modeling and Simulation of Microsystems*, vol. 1. Nano Science and Technology Institute, 2001, pp. 286–9.

[65] David P. Arnold *et al*, "Magnetic induction machines embedded in fusion-bonded silicon," presented at the Solid-State Sensor, Actuator and Microsystems Workshop (Hilton Head 2004), 2004.

[66] M. Nienhaus, W. Ehrfeld, H.-D. Stölting, F. Michel, S. Kleen, S. Hardt, F. Schmitz, and T. Stange, "Design and realization of a penny-shaped micromotor," in *Design, Test, and Microfabrication of MEMS and MOEMS*, vol. 3680. SPIE - the International Society for Optical Engineering, 1999, pp. 592–600.

[67] T. Kohlmeier, V. Seidemann, S. Büttgenbach, and H. H. Gatzen, "Application of UV depth lithography and 3D-microforming for high aspect ratio electromagnetic microactuator components," *Microsystem Technologies*, vol. 8, no. 4-5, pp. 304–7, Aug. 2002.

[68] J. Edler, H.-D. Stölting, M. Föhse, and H. H. Gatzen, "A linear microactuator with enhanced design," *Microsystem Technologies*, vol. 7, no. 5-6, pp. 261–4, Jan. 2002.

[69] J. R. Melcher, *Continuum Electromechanics.* MIT Press, 1981.

[70] H. H. Woodson and J. R. Melcher, *Electromechnical Dynamics.* John Wiley & Sons, Inc., 1968.

[71] J.-M. Jin, *The Finite Element Method in Electromagnetics.* John Wiley & Sons, Inc., 2002.

[72] J. Luo, D. Qin, T. A. Lipo, S. Li, and S. Huang, "Axial flux circumferential current permanent magnet (AFCC) machine," in *1998 IEEE Industry Applications Conference*, vol. 1. IEEE, 1998, pp. 144–51.

[73] J. Cros, J. R. Figueroa, and P. Viarouge, "BLDC motors with surface mounted PM rotor for wide constant power operation," in *2003 IEEE Industry Applications Conference*, vol. 3. IEEE, 2003, pp. 1933–40.

[74] J. Wang, W. Wang, G. W. Jewell, and D. Howe, "Design optimisation of a miniature multi-pole permanent magnet generator," in *Ninth International Conference on Electrical Machines and Drives*. IEE, 1999, pp. 128–32.

[75] J. R. Hendershot, Jr. and T. J. E. Miller, *Design of Brushless Permanent–Magnet Motors*. Magna Physics Publishing, 1994.

[76] "Neoform material properties," Product data sheet, Dexter Magnetic Technologies, Inc. [Online]. Available: http://www.dextermag.com

[77] D. G. Jones, "Fabrication of ultra thick ferromagnetic structures in silicon," Master's thesis, University of California, Berkeley, 2004.

[78] K. Halbach, "Application of permanent magnets in accelerators and electron storage rings," *Journal of Applied Physics*, vol. 57, no. 8, pp. 3605–8, Apr. 1985.

[79] H. C. Roters, *Electromagnetic Devices*. John Wiley & Sons, Inc., 1941.

[80] H.-D. Chai, *Electromechanical Motion Devices*. Prentice Hall, Inc., 1998.

[81] J. A. Moses, J. L. Kirtley, Jr., J. H. Lang, R. D. Tabors, and F. de Caudra García, "A computer-based design assistant for induction motors," *IEEE Transactions on Industry Applications*, vol. 30, no. 6, pp. 1616–24, Nov./Dec. 1994.

[82] U. Sinha and J. L. Kirtley, Jr., "Design synthesis of induction motors," in *International Conference on Electrical Machines (ICEM '94)*, vol. 1. Soc. Electr. Electron., 1994, pp. 106–11.

Appendix A

Equations

A.1 Magnetic Circuit Equations

Referring to the magnetic circuit model given in Fig. 6.11, given the reluctance values and MMF source values, the fluxes in the loops defined in the figure are given by

$$\lambda = \mathbf{R}^{-1}\mathbf{I} \tag{A.1}$$

where the MMF vector $\mathbf{I}$ is

$$\mathbf{I} = \begin{bmatrix} i_2 & i_2 & i_{pm} & i_{pm} & i_{pm} & i_{pm} & i_1 & i_1 \end{bmatrix}^T \tag{A.2}$$

and the flux vector λ is

$$\lambda = \begin{bmatrix} \lambda_1 & \lambda_2 & \lambda_3 & \lambda_4 & \lambda_5 & \lambda_6 & \lambda_7 & \lambda_8 \end{bmatrix}^T. \tag{A.3}$$

The reluctance matrix is given by

$$\mathbf{R}=\begin{bmatrix} \frac{1}{2}R_y+2R_z & 2R_z & 0 & 0 & 0 & 0 & 0 & 0 \\ 2R_z & R_{22} & -R_7 & R_6 & 0 & 0 & 0 & 0 \\ 0 & -R_7 & R_{33} & R_v+\frac{1}{2}R_x & R_v+\frac{1}{2}R_x & R_v+\frac{1}{2}R_x & 0 & 0 \\ 0 & R_6 & R_v+\frac{1}{2}R_x & R_{44} & R_v+\frac{1}{2}R_x & R_v+\frac{1}{2}R_x & 0 & 0 \\ 0 & 0 & R_v+\frac{1}{2}R_x & R_v+\frac{1}{2}R_x & R_{55} & R_v+\frac{1}{2}R_x & R_4 & 0 \\ 0 & 0 & R_v+\frac{1}{2}R_x & R_v+\frac{1}{2}R_x & R_v+\frac{1}{2}R_x & R_{66} & -R_1 & 0 \\ 0 & 0 & 0 & 0 & R_4 & -R_1 & R_{77} & 2R_z \\ 0 & 0 & 0 & 0 & 0 & 0 & 2R_z & \frac{1}{2}R_y+2R_z \end{bmatrix} \tag{A.4}$$

where

$$\begin{aligned} R_{22} &= R_6+R_7+2R_z \\ R_{33} &= R_7+R_8+R_v+\tfrac{1}{2}R_x \\ R_{44} &= R_5+R_6+R_v+\tfrac{1}{2}R_x \\ R_{55} &= R_3+R_4+R_v+\tfrac{1}{2}R_x \\ R_{66} &= R_1+R_2+R_v+\tfrac{1}{2}R_x \\ R_{77} &= R_1+R_4+2R_z. \end{aligned}$$

While knowledge of the values for λ_1-λ_8 is useful in understanding circuit behavior, the main concern is the flux through each of the MMF sources, i.e.

$$\lambda' = \begin{bmatrix} \lambda'_1 \\ \lambda'_2 \\ \lambda'_{pm} \end{bmatrix} = \begin{bmatrix} \lambda_7+\lambda_8 \\ \lambda_1+\lambda_2 \\ \lambda_3+\lambda_4+\lambda_5+\lambda_6 \end{bmatrix}. \tag{A.5}$$

Note that $\lambda' = \mathbf{T}\lambda$, where

$$\mathbf{T} = \begin{bmatrix} 0 & 0 & 0 & 0 & 0 & 0 & 1 & 1 \\ 1 & 1 & 0 & 0 & 0 & 0 & 0 & 0 \\ 0 & 0 & 1 & 1 & 1 & 1 & 0 & 0 \end{bmatrix} \tag{A.6}$$

and define

$$\mathbf{I}' = \begin{bmatrix} i_1 \\ i_2 \\ i_{pm} \end{bmatrix} \tag{A.7}$$

such that

$$\mathbf{I} = T^T \mathbf{I}'. \tag{A.8}$$

Then

$$\lambda' = (\mathbf{T}\mathbf{R}^{-1}\mathbf{T}^{\mathbf{T}})\mathbf{I}' \tag{A.9}$$

and hence the inductance matrix is given by

$$\mathbf{L} = \mathbf{T}\mathbf{R}^{-1}\mathbf{T}^{\mathbf{T}}. \tag{A.10}$$

It is then straightforward to calculate the coenergy for the case of linear materials:

$$W_c = \tfrac{1}{2}\mathbf{I}'^{\mathbf{T}}\mathbf{L}\mathbf{I}'. \tag{A.11}$$

A.2 Combining FEA Results at Varying Radius

Three radii are selected at which to evaluate the circumferential cross section of the machine. The axial dimensions do not change; only the circumferential dimensions change according to variations in the pole geometry over radius. A force density versus displacement curve is computed for each geometry using the coenergy density approach, with each curve having the same number of points. The result is a discrete-valued function $f'(\phi, r)$, where ϕ is rotor angle and r is radius

For force density as a function of radius at a given angle $f'(\phi, r)$, torque can be computed as

$$\tau(\phi) = \int_{r_1}^{r_2} f'(\phi, r) r dr. \tag{A.12}$$

A second-order polynomial was selected to fit to the discrete $f'(\phi, r)$ data points at each value of ϕ. At a given rotor angular position, the function described above gives three force density values at different radii: $f'(r_1)$, $f'(r_2)$, $f'(r_3)$. The polynomial fit must satisfy

$$\begin{bmatrix} f'(\phi, r_1) \\ f'(\phi, r_2) \\ f'(\phi, r_3) \end{bmatrix} = \begin{bmatrix} r_1^2 & r_1 & 1 \\ r_2^2 & r_2 & 1 \\ r_3^2 & r_3 & 1 \end{bmatrix} \begin{bmatrix} a_1 \\ a_2 \\ a_3 \end{bmatrix} \tag{A.13}$$

where a_1-a_3 are the polynomial coefficients. Solving for the coefficients gives

$$\vec{a} = \mathbf{r}^{-1}\vec{f}. \tag{A.14}$$

Now, substituting the polynomial into Eq. A.12 gives

$$\tau = \int_{r_1}^{r_3} (a_1 r_2 + a_2 r + a_3 r) r dr, \tag{A.15}$$

which evaluates to

$$\tau = (\frac{a_1}{4})(r_3^4 - r_1^4) + (\frac{a_2}{3})(r_3^3 - r_1^3) + (\frac{a_3}{2})(r_3^2 - r_1^2). \tag{A.16}$$

A.3 Coenergy Density in Nonlinear Materials

The coenergy density within the nonlinear soft magnetic material included in the FEA model of Ch. 6 can be found by evaluating the integral

$$W_c' = \int B(H) \cdot dH. \tag{A.17}$$

However, the nature of the FEA solution requires that μ_r be specified in terms of B, as in Eq. 6.9. Hence the energy density integral

$$W' = \int H(B) \cdot dB \tag{A.18}$$

is easier to evaluate. Nonetheless, calculation via FEA demands the use of coenergy. Thus, as in Eq. 4.27, Eq. A.10 above can be written in terms of Eq. A.11:

$$W_c' = H \cdot B - \int H(\hat{B}) \cdot d\hat{B}. \tag{A.19}$$

Assuming that Eq. 6.9 represents the pointwise slope of the B-H relationship for the soft magnetic material under consideration, the function $H(B)$ can be reconstructed by evaluating

$$H(B) = \int_0^B \frac{1}{\mu(B)} dB, \tag{A.20}$$

where $\mu(B)$ is given by Eq. 6.9. This difficult integration can be performed symbolically by MATLAB, returning

$$H(B) = \frac{B}{\mu_o} - \frac{\mu_r \arctan\left(\frac{CB}{\sqrt{C(\mu_r+1)}}\right)}{\mu_o\sqrt{C(\mu_r+1)}}. \tag{A.21}$$

Evaluating A.11 for H(B) as given by Eq. A.21 gives

$$W' = \frac{1}{2}\frac{B^2}{\mu_o} - \frac{\mu_r B \arctan\left(\frac{CB}{\sqrt{C(\mu_r+1)}}\right)}{\mu_o\sqrt{C(\mu_r+1)}} + \frac{1}{2}\frac{\mu_r \ln(1 + \frac{CB^2}{\mu_r+1})}{\mu_o C}. \tag{A.22}$$

Hence the coenergy density in the saturating soft magnetic materials can be calculated by

$$W_c' = H \cdot B - W', \tag{A.23}$$

where W' is given by Eq. A.22. And finally, coenergy can be found by integrating coenergy density over volume, as in Eq. 4.44.

Appendix B

Material Data

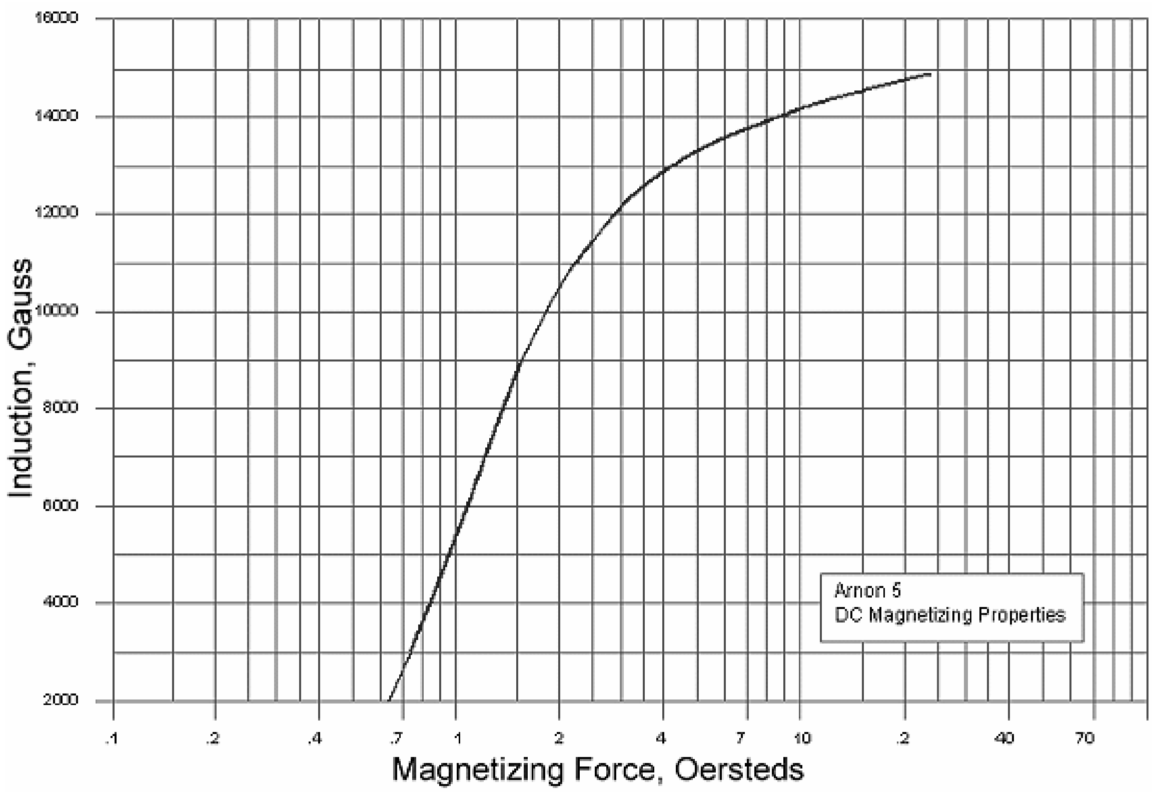

Figure B.1: Magnetization curve for Arnon 5 material [37].

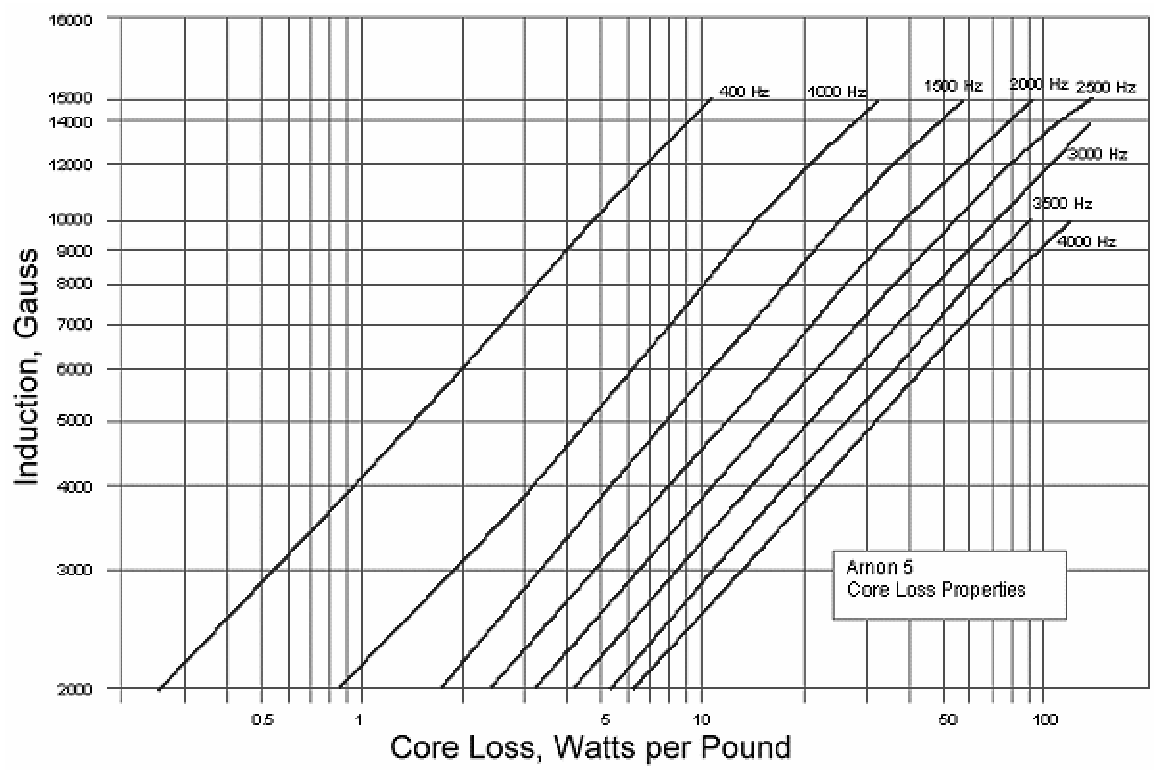

Figure B.2: Core loss for Arnon 5 material [37].

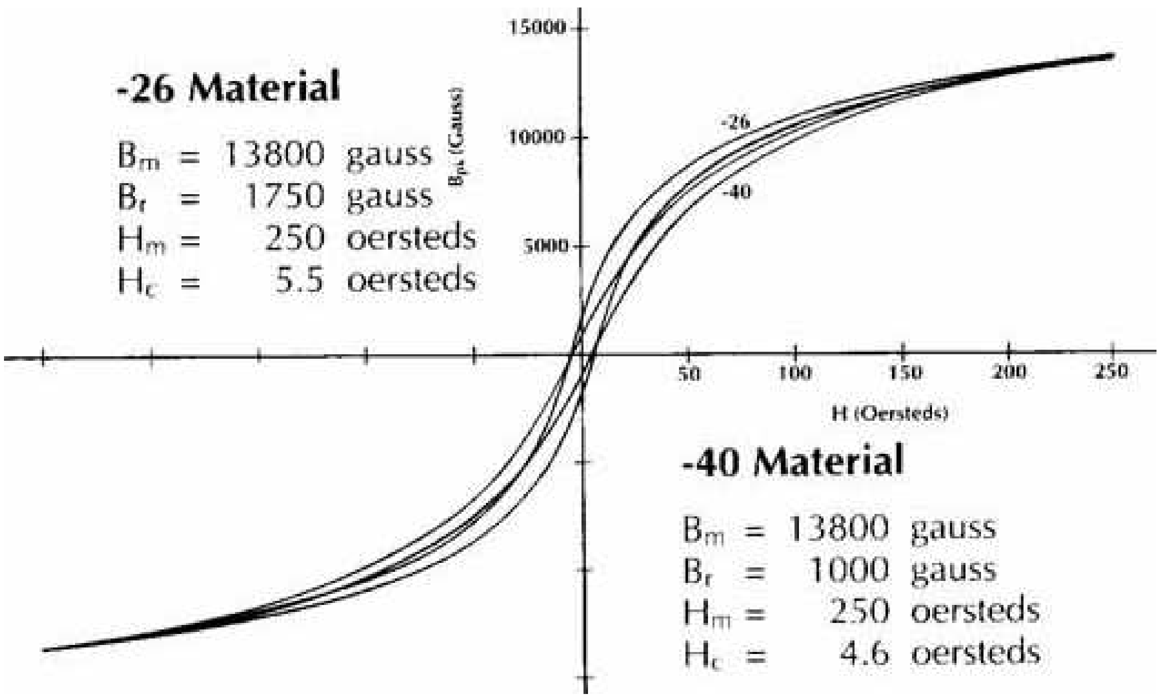

Figure B.3: B-H loop for Micrometals -26 material [38].

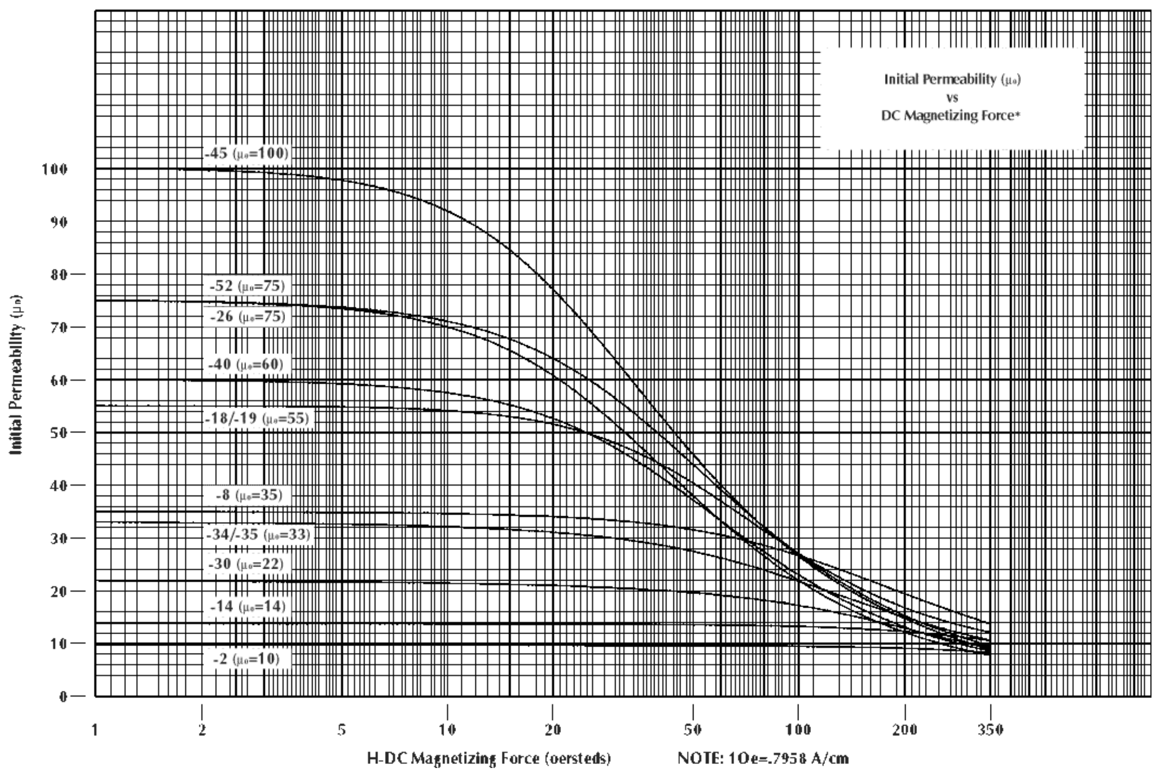

Figure B.4: Permeability versus field intensity for Micrometals -26 material [38].

Appendix C

Simulation Code

C.1 Lumped Element Calculations

```
% File: ckt_model_fn.m
% Function to perform lumped element calculations
% Last updated: 3/19/05

function [hVect,Wc,Torque]=ckt_model_fn(nIter,P,ro,rt,rp,hb,Iw,...
rx,wi,wm,wa,hc,hf,ell,wf,pitch,Ap)
% Note that Ap is center post area for *one pole pair*

global uo urfe ur26 rhocu rhofe Br g hr rs ironfrac stp wi...
shiftVect1 shiftVect0;

%------------------------
% Operating point

i1=Iw;
i2=Iw;

%------------------------
% Constant reluctances

Rv=wi/(uo*urfe*hr*ell); % rotor iron
Rx=wm/(uo*hr*ell);      % magnet
Ry=wa/(uo*hf*ell);      % winding leakage
Rza=hc/(uo*urfe*Ap);    % stator tooth
Rzb=(0.5*(ro+rt)-0.5*(rp+rs))/(uo*ur26*pi*(ro+rt+rp+rs)*hb/P); % back iron
Rz=Rza+0.5*Rzb;

%------------------------
% Magnet values

lamPM=2*Br*hr*ell;      % PM flux
ipm=0.5*lamPM*Rx;       % equivalent current source
```

```
%-----------------------
% Displacement loop

shiftVect0=linspace(0,pitch,nIter/2);
shiftVect1=sort([shiftVect0-pitch/1e5,shiftVect0+pitch/1e5]);

for iter=1:nIter
    Q=shiftVect1(iter);

    %-----------------------
    % Varying reluctances
        % define ends of each stator pole
        stp(1,:)=[0, wf];
        stp(2,:)=stp(1,:)+pitch;
        stp(3,:)=stp(1,:)+0.5*pitch;
        stp(4,:)=stp(1,:)+1.5*pitch;
        stp(5,:)=[inf inf];
        if stp(4,2)>2*pitch
            wrapFlag=1;
            stp(4,:)=[stp(4,1), 2*pitch];
            stp(5,:)=[0, stp(3,1)-wa];
        else wrapFlag=0;
        end

        % define ends of rotor pole
        rop=[0, wi]+Q;

        Rmax=1e10;   % max reluctance for unaligned poles

        % compare rotor to stator to determine R's

            % for pole 1
            if rop(2)<=stp(1,1)      % no ovrlap w stp 1
                R1=1e12;
            elseif stp(1,2)<=rop(1)  % no ovrlap w stp 1
                R1=1e12;
            elseif rop(1)<stp(1,1) & stp(1,1)<rop(2) & rop(2)<stp(1,2) % some ovrlap w stp 1
                R1=g/(uo*ell*(rop(2)-stp(1,1)));
            elseif stp(1,1)<rop(1) & rop(1)<stp(1,2) & stp(1,2)<rop(2) % some ovrlap w stp 1
                R1=g/(uo*ell*(stp(1,2)-rop(1)));
            elseif rop(1)<=stp(1,1) & stp(1,2)<=rop(2)      % complete ovrlap w stp 1
                R1=g/(uo*ell*(stp(1,2)-stp(1,1)));
            elseif stp(1,1)<=rop(1) & rop(2)<=stp(1,2)      % complete ovrlap w stp 1
                R1=g/(uo*ell*(rop(2)-rop(1)));
            else end

            if R1 > Rmax
                R1=Rmax;
            else end

        R3=R1;

            % for pole 2
            if rop(2)<=stp(2,1)       % no ovrlap w stp 2
                R2=1e12;
            elseif stp(2,2)<=rop(1)  % no ovrlap w stp 2
                R2=1e12;
            elseif rop(1)<stp(2,1) & stp(2,1)<rop(2) & rop(2)<stp(2,2) % some ovrlap w stp 2
                R2=g/(uo*ell*(rop(2)-stp(2,1)));
            elseif stp(2,1)<rop(1) & rop(1)<stp(2,2) & stp(2,2)<rop(2) % some ovrlap w stp 2
                R2=g/(uo*ell*(stp(2,2)-rop(1)));
            elseif rop(1)<=stp(2,1) & stp(2,2)<=rop(2)      % complete ovrlap w stp 2
```

```
        R2=g/(uo*ell*(stp(2,2)-stp(2,1)));
    elseif stp(2,1)<=rop(1) & rop(2)<=stp(2,2)      % complete ovrlap w stp 2
        R2=g/(uo*ell*(rop(2)-rop(1)));
    else end

    if R2 > Rmax
        R2=Rmax;
    else end

R4=R2;

    % for pole 3
    if rop(2)<=stp(3,1)       % no ovrlap w stp 3
        R6=1e12;
    elseif stp(3,2)<=rop(1)  % no ovrlap w stp 3
        R6=1e12;
    elseif rop(1)<stp(3,1) & stp(3,1)<rop(2) & rop(2)<stp(3,2) % some ovrlap w stp 3
        R6=g/(uo*ell*(rop(2)-stp(3,1)));
    elseif stp(3,1)<rop(1) & rop(1)<stp(3,2) & stp(3,2)<rop(2) % some ovrlap w stp 3
        R6=g/(uo*ell*(stp(3,2)-rop(1)));
    elseif rop(1)<=stp(3,1) & stp(3,2)<=rop(2)      % complete ovrlap w stp 3
        R6=g/(uo*ell*(stp(3,2)-stp(3,1)));
    elseif stp(3,1)<=rop(1) & rop(2)<=stp(3,2)      % complete ovrlap w stp 3
        R6=g/(uo*ell*(rop(2)-rop(1)));
    else end

    if R6 > Rmax
        R6=Rmax;
    else end

R8=R6;

if wrapFlag==1
    % for pole 4
    if rop(1)>=stp(5,2) & rop(2)<=stp(4,1)       % no ovrlap w stp 4 or 5
        R5=1e12;
    elseif rop(1)<stp(4,1) & stp(4,1)<rop(2) & rop(2)<stp(4,2) % some ovrlap w stp 4 not 5
        R5=g/(uo*ell*(rop(2)-stp(4,1)));
    elseif stp(5,1)<rop(1) & rop(1)<stp(5,2) & stp(5,2)<rop(2) % some ovrlap w stp 5 not 4
        R5=g/(uo*ell*(stp(5,2)-rop(1)));
    elseif rop(1)<=stp(4,1) & stp(4,2)<=rop(2)      % complete ovrlap w stp 4
        R5=g/(uo*ell*(stp(4,2)-stp(4,1)));
    elseif stp(4,1)<=rop(1) & rop(2)<=stp(4,2)      % complete ovrlap w stp 4
        R5=g/(uo*ell*(rop(2)-rop(1)));
    elseif rop(1)<=stp(5,1) & stp(5,2)<=rop(2)      % complete ovrlap w stp 5
        R5=g/(uo*ell*(stp(5,2)-stp(5,1)));
    elseif stp(5,1)<=rop(1) & rop(2)<=stp(5,2)      % complete ovrlap w stp 5
        R5=g/(uo*ell*(rop(2)-rop(1)));
    else
        R5=1e12;
    end

else
    % for pole 4
    if rop(2)<=stp(4,1)       % no ovrlap w stp 4
        R5=1e12;
    elseif stp(4,2)<=rop(1)  % no ovrlap w stp 4
        R5=1e12;
    elseif rop(1)<stp(4,1) & stp(4,1)<rop(2) & rop(2)<stp(4,2) % some ovrlap w stp 4
        R5=g/(uo*ell*(rop(2)-stp(4,1)));
    elseif stp(4,1)<rop(1) & rop(1)<stp(4,2) & stp(4,2)<rop(2) % some ovrlap w stp 4
        R5=g/(uo*ell*(stp(4,2)-rop(1)));
    elseif rop(1)<=stp(4,1) & stp(4,2)<=rop(2)      % complete ovrlap w stp 4
```

```
            R5=g/(uo*ell*(stp(4,2)-stp(4,1)));
        elseif stp(4,1)<=rop(1) & rop(2)<=stp(4,2)      % complete ovrlap w stp 4
            R5=g/(uo*ell*(rop(2)-rop(1)));
        else
            R5=1e12;
        end
    end

    if R5 > Rmax
        R5=Rmax;
    else end

    R7=R5;

    %-----------------------
    % Reluctance matrix

      RRR=[ 2*Rz+0.5*Ry 2*Rz, 0, 0, 0, 0, 0, 0; ...
            2*Rz, R6+R7+2*Rz, -R7, R6, 0, 0, 0, 0; ...
            0, -R7, R7+R8+Rv+0.5*Rx, Rv+0.5*Rx, Rv+0.5*Rx, Rv+0.5*Rx, 0, 0; ...
            0, R6, Rv+0.5*Rx, R5+R6+Rv+0.5*Rx, Rv+0.5*Rx, Rv+0.5*Rx, 0, 0; ...
            0, 0, Rv+0.5*Rx, Rv+0.5*Rx, R3+R4+Rv+0.5*Rx, Rv+0.5*Rx, R4, 0; ...
            0, 0, Rv+0.5*Rx, Rv+0.5*Rx, Rv+0.5*Rx, R1+R2+Rv+0.5*Rx, -R1, 0; ...
            0, 0, 0, 0, R4, -R1, R1+R4+2*Rz, 2*Rz; ...
            0, 0, 0, 0, 0, 0, 2*Rz, 2*Rz+0.5*Ry ];

    TTT=[0 0 0 0 0 0 1 1; 1 1 0 0 0 0 0 0; 0 0 1 1 1 1 0 0];

    LLL=TTT*inv(RRR)*TTT';

    Wc(iter)=0.5*[i1 i2 ipm]*LLL*[i1; i2; ipm];

    % mmf vector
    MMM=[i2; i2; ipm; ipm; ipm; ipm; i1; i1];

    % Flux solution
    hVect(:,iter)=inv(RRR)*MMM;

end

dWc=diff(Wc); dWc=dWc(1:2:nIter-1); dSh=diff(shiftVect1);
dSh=dSh(1:2:nIter-1);
Force=dWc./dSh;   % This is a force, not a force density, for one pole pair
Torque=Force*rx;  % This is a torque, not a torque density, for one pole pair
```

C.2 Monte-Carlo Optimization

```
% File: monte_carlo_for_thesis_2.m
% Stator optimization script, monte carlo style
% Last updated 4/18/05

% Setup ============================================================================

    % Logistics
        warning off;    % suppresses warnings
        numIter=1000;   % Number of monte carlo iterations
        dispIter=64;    % Number of rotor displacement iterations (even number)
        myOrder=1;      % Order of sinsusoidal fit to torque curve
```

```
        % Material constants
            global uo urfe ur26 rhocu Br;
            uo=4*pi*1e-7;   % permeability of vacuum
            urfe=100;       % relative permeability of steel lams
            %urfe=1000;
            %urfe=83;
            ur26=50;
            %ur26=75;
            %ur26=59;
            rhocu=1.7e-8;   % resistivity of copper (ohm-meters)
            Br=1.2;         % Residual flux density
            maxLam=1.0;     % saturation level of mag material

        % Operating point
            rpm=10e3;       % mechanical rotor speed
            fmech=rpm/60;   % mechanical frequency, in Hz
            wmech=fmech*2*pi;   % mechanical frequency, in rad/sec

        % Fixed geometry
            global Vol g hr ironfrac rs;
            Vol=45e-6;      % overall volume of the assembly (half stator), in m^3
            rs=3e-3;        % shaft radius
            g=0.25e-3;      % gap
            hr=5e-3;        % rotor height
            ironfrac=.55;   % fraction of iron in rotor at min radius
            pf=0.5;         % copper packing factor

        % Design parameter ranges
            Pmin=6;         % Number of poles
            PRange=12;

            roMin=12e-3;    % Outer radius
            roRange=30e-3;

            rpMin=0.20;     % Center post/outer radius ratio
            rpRange=0.25;

            hfMin=0.03;     % Pole face height/total height ratio
            hfRange=0.32;

            hbMin=0.10;     % Back iron height/total height ratio
            hbRange=0.40;

            IwMin=100;      % Winding current
            IwRange=600;

            pause;

        % Solution library
            %myOutput=zeros(1,20);
            load outLibrary_4-18;

% Monte Carlo loop ===================================================================

    for iter=1:numIter

        % Randomly generate design parameters
            P=Pmin+2*round(rand*PRange/2);  % Number of poles
            ro=roMin+rand*roRange;          % Outer radius
            rpFrac=rpMin+rand*rpRange;      % Center post/outer radius ratio
            hfFrac=hfMin+rand*hfRange;      % Pole face height/total height ratio
            hbFrac=hbMin+rand*hbRange;      % Back iron height/total height ratio
            Iw=IwMin+rand*IwRange;          % Winding current
```

```
% Calculate remaining parameters
    % Heights
    ho=Vol/(pi*ro^2);   % overall assembly height (half stator, not incl. rotor)
    hf=hfFrac*ho;       % pole face height
    hb=hbFrac*ho;       % back iron height
    hc=ho-hf-hb;        % copper height

    % Radii
    rp=rpFrac*ro;                   % radius of center post
    rt=sqrt(ro^2-rp^2+rs^2);        % toroid inner radius
    x1=2*rp*cos(pi/P);              % inner magnet radius
    x2=(rt^2-rp^2*(sin(2*pi/P))^2)^0.5; % outer magnet radius
    ell=x2-x1;                      % span of magnet (depth into page)
    rx=(x1+x2)/2;               % radius of circ. cross-section (avg. radius)

    % Widths and circumferential dimensions
    pitch=rx*2*pi/P;            % circ. distance between poles at avg. radius
    realwm=2*x1*sin((1-ironfrac)*pi/P);     % actual width of magnet
    phim=2*asin(realwm/(2*rx));             % angle occupied by magnet at rx
    wm=rx*phim;                             % circ. width of magnet at rx
    wi=pitch-wm;                            % circ. width of rotor iron at rx
    realwf=2*rp*sin(2*pi/P);            % width of one stator pole face
    phif=2*asin(realwf/(2*rx));         % angle occupied by pole face at rx
    wf=rx*phif;                         % circ. width of pole face at rx
    wa=pitch-wf;                        % circ. width of air at rx
    ellc=2*pi*0.5*(rt+rp);      % average winding turn length

    % Areas
    Ap=pi*(rp^2-rs^2);  % center post cross sectional area
    At=Ap;              % toroid cross sectional area
    Abav=hb*pi*(ro+rt+rp+rs)/P; % avg cross sectional area of back iron
    Abpk=2*pi*0.5*(rp+rs)*hb;   % peak cross sectional area of back iron
    Afr=(P/2)*wf*hf;    % radially oriented cross sectional area of pole faces
    Afa=(P/2)*wf*ell;   % axially oriented cross sectional area of pole faces
    Ac=(rt-rp)*hc;      % copper cross sectional area
    Asurf=2*pi*ro*ho+pi*ro^2; % stator surface area (half stator)

% Get flux solution
    [hVect,Wc,Torque,TorqFit]=ckt_model_fn_fft(dispIter,P,ro,rt,rp,hb,Iw,rx,wi,wm,wa,...
    hc,hf,ell,wf,pitch,2*Ap/P,myOrder);


% Calculate flux densities in saturable components
    lam78=max(abs((P/2)*(hVect(7,:)+hVect(8,:))));  % center post flux phase 1
    lam12=max(abs((P/2)*(hVect(1,:)+hVect(2,:))));  % center post flux phase 2
    lam=max([lam78 lam12]);                         % max flux

    Bp=lam/Ap;      % peak flux density in center post
    Bt=Bp;          % flux density in toroid
    Bbav=lam/Abav;      % average flux density in back iron
    Bbpk=lam/Abpk;      % peak flux density in back iron
    Bf=lam/Afr;     % flux density in pole faces

% Need a few values for loss calculation
    felec=(P/2)*fmech;      % electrical frequency, in Hz
    Rw=rhocu*ellc/(Ac*pf);  % winding resistance

% filter out results w over-saturated materials, non-interleaved faces, or anomalous results
if Bp<maxLam & Bbpk<maxLam & Bf<maxLam & ell>0 & rp>rs & max(Torque)<25*mean(abs(Torque))

    PpDens=myArnonLoss(Bp,felec);       % loss dens in center post
    PtDens=PpDens;                  % loss dens in toroid
```

```
            PbDens=myMicrometLoss(Bbav,felec);  % loss dens in back iron (use average flux density)
            PfDens=myArnonLoss(Bf,felec);       % loss dens in pole faces

            volP=Ap*hc;         % volume of center post (half stator)
            volT=volP;          % volume of toroid (half stator)
            volB=Abav*(0.5*(ro+rt)-0.5*(rp+rs));  % effective volume of back iron (half stator)
            volF=2*Afr*(ro-rs); % approximate volume of pole faces (overestimates)

            % Power calculations =================================================

            Pp=PpDens*volP;     % core loss in center post (half stator)
            Pt=PtDens*volT;     % core loss in toroid (half stator)
            Pb=PbDens*volB;     % core loss in back iron (half stator)
            Pf=PfDens*volF;     % core loss in pole faces (half stator)
            Pcore=2*(Pp+Pt+Pb+Pf);  % total core loss (whole machine)

            Pmech=(P/2)*max(abs(TorqFit))*wmech;    % Mechanical power (whole machine)

            Pcu=2*Iw^2*Rw;        % conduction loss (whole machine)
            Pout=Pmech-Pcu-Pcore;   % Net power (whole machine)
            eta=Pout/Pmech;  % efficiency


        % Check list
        dropFlag=0;
        for nchk=1:size(myOutput)*[1;0]
            if (myOutput(nchk,1) < Pout | myOutput(nchk,2) < eta)
                % point is approved if it has superior Pout OR eta, AND is thermally acceptable
            else
                dropFlag=1;
            end % if
        end % for

        if dropFlag==0
            % Purge list
            ntemp=1;
            tempOutput=[];
            for npur=1:size(myOutput)*[1;0]
                if myOutput(npur,1) < Pout & myOutput(npur,2) < eta
                    plot(myOutput(npur,2), myOutput(npur,1),'rx');
                    hold on;
                else
                    tempOutput(ntemp,:)=myOutput(npur,:);   % keep good points
                    ntemp=ntemp+1;
                end % if
            end % for
            myOutput=tempOutput;

            % Save point
            myOutput(size(myOutput)*[1;0]+1,:)=[Pout,eta,P,ro,rp,rt,rx,ho,hf,hb,hc,Ap,Bp,Bt,...
            Bbpk,Bf,Iw,Pcore,Pcu,(Pcore+Pcu)/(2*Asurf)];
            plot(eta, Pout,'ko');
            hold on;
        else end % if dropFlag==0
    else
    end % if Bp<1 etc

end % for

save outLibrary_4-19 myOutput;
%
```

C.3 Finite Element Analysis

```
% File: mini_gen_002_3pt_pole_axial_4.m
% 2-D finite-element generator model
% w nested loops to account for variation
% in pole geometry w radius
% Corrected tooth width calculation
% Last updated 4/19/05
% Includes nonlinear calculation of coenergy
% Updated so that all domains are accounted for in coeng calc

% Overall
ro=25.1e-3; rt=23.3e-3; rp=9.8e-3; rs=3e-3; P=10;

x1=2*rp*cos(pi/P);      % see notes 11/11/04
x2=(rt^2-rp^2*(sin(2*pi/P))^2)^0.5; ell=x2-x1;

%=========================================================
% Radius loop setup

rxVect=x2-ell*[0.9 0.5 0.1];    % rxVect actually goes from small to large

for rxCount=1:max(size(rxVect))
    rx=rxVect(rxCount);

%=========================================================
%=========================================================
% My dimensions
%=========================================================

    % Y dimensions
    hb=7.7e-3;    % back iron height
    hc=11.1e-3;   % copper height
    hf=4.0e-3;    % stator pole face height
    g=0.25e-3;     % gap
    hr=5e-3;    % rotor height

    Y1=hr/2;    % top of rotor
    Y2=Y1+g;    % bottom of stator
    Y3=Y2+hf;   % bottom of coil
    Y4=Y3+hc;   % top of coil
    Y5=Y4+hb;   % top of stator

    % X dimensions
    pitch=rx*2*pi/P;

    %============================================================
    ironfrac=.55;                                   % fraction of iron in rotor at min radius
    realwm=2*x1*sin((1-ironfrac)*pi/P);             % actual width of magnet
    phi=2*asin(realwm/(2*rx));                      % angle occupied by magnet at given radius
    wm=rx*phi;                                      % circumferential width of magnet at given radius
    wi=pitch-wm;                                    % circumferential width of iron at given radius


        Xr1=wi/2;
        Xr2=Xr1+wm;
        Xr3=pitch;
    %============================================================

    airfrac=1-(P/pi)*asin((rp/rx)*sin(2*pi/P));    % fraction of air in stator
    wa=pitch*airfrac;
    wf=pitch*(1-airfrac);
    wt=0.5*wf;
```

```
    AtError=wt*ell/(pi*(rp^2-rs^2)*(2/P));   % ratio of FEA area to real area for teeth
    AbError=ell/((pi/2)*(ro+rt+rp+rs)*(2/P));       % ratio of FEA area to real area for back iron

        Xs1=wt/2;
        Xs2=wf/2;
        Xs3=Xs2+wa;
        Xs4=pitch-wt/2;
        Xs5=pitch;

        Xs6=wa/2;
        Xs9=Xs6+wf;
        Xs7=(pitch/2)-(wt/2);
        Xs8=Xs7+wt;

        Y1=hr/2;    % top of rotor
        Y2=Y1+g;    % bottom of stator
        Y3=Y2+hf;   % bottom of coil
        Y4=Y3+hc;   % top of coil
        Y5=Y4+hb;   % top of stator

%========================================================

% Loop setup ==================
numIter=64; % use an even number
shiftVect0=linspace(0,2*pitch,numIter/2);
shiftVect1=sort([shiftVect0-pitch/1e3,shiftVect0+pitch/1e3]);

    % Check shiftVect to avoid degenerate geometries ++++++++++++++
        mydelta=1;
        goo=abs([pitch-(-Xr2+shiftVect1);pitch-(-Xr1+shiftVect1);pitch-(Xr1+shiftVect1);...
        pitch-(Xr2+shiftVect1)]);
        while (min(min(goo))<Y1/15 & mydelta<=40)
            shiftVect1=sort([shiftVect0-pitch*mydelta/1e3,shiftVect0+pitch*mydelta/1e3]);
            goo=abs([pitch-(-Xr2+shiftVect1);pitch-(-Xr1+shiftVect1);pitch-(Xr1+shiftVect1);...
            pitch-(Xr2+shiftVect1)]);
            mydelta=mydelta+1;
        end % while

    %+++++++++++++++++++++++++++++++++++++++++++++++++++++++++++

for indx=1:numIter for indx=1:1

    shift=shiftVect1(indx);

%=============================

%------------------------
flclear fem
% FEMLAB Version
clear vrsn; vrsn.name='FEMLAB 2.2'; vrsn.major=0; vrsn.build=183;
fem.version=vrsn;
%------------------------
%------------------------
% New geometry 1
fem.sdim={'x','y'};

% Geometry
clear s c p
% Top stator
R1=rect2(-Xs5,Xs5,Y4,Y5,0); R2=rect2(-Xs5,-Xs4,Y3,Y4,0);
R3=rect2(-Xs4,-Xs1,Y3,Y4,0); R4=rect2(-Xs1,Xs1,Y3,Y4,0);
R5=rect2(Xs1,Xs4,Y3,Y4,0); R6=rect2(Xs4,Xs5,Y3,Y4,0);
R7=rect2(-Xs5,-Xs3,Y2,Y3,0); R8=rect2(-Xs3,-Xs2,Y2,Y3,0);
```

```
R9=rect2(-Xs2,Xs2,Y2,Y3,0); R10=rect2(Xs2,Xs3,Y2,Y3,0);
R11=rect2(Xs3,Xs5,Y2,Y3,0); R12=rect2(-Xs5,Xs5,Y1,Y2,0);

% Rotor

% wrap around ==================================================
    if Xr1+shift <= Xr3 & Xr2+shift > Xr3       % small shift

            R13=rect2(-Xr3,Xr2+shift-2*Xr3,-Y1,Y1,0);       % +mval
            R14=rect2(Xr2+shift-2*Xr3,-Xr2+shift,-Y1,Y1,0); % steel
            R15=rect2(-Xr2+shift,-Xr1+shift,-Y1,Y1,0);      % -mval
            R16=rect2(-Xr1+shift,Xr1+shift,-Y1,Y1,0);       % steel
            R17=rect2(Xr1+shift,Xr3,-Y1,Y1,0);              % +mval

    elseif -Xr1+shift <= Xr3 & Xr1+shift > Xr3    % large shift

            R13=rect2(-Xr3,Xr1+shift-2*Xr3,-Y1,Y1,0);               % steel
            R14=rect2(Xr1+shift-2*Xr3,Xr2+shift-2*Xr3,-Y1,Y1,0);    % +mval
            R15=rect2(Xr2+shift-2*Xr3,-Xr2+shift,-Y1,Y1,0);         % steel
            R16=rect2(-Xr2+shift,-Xr1+shift,-Y1,Y1,0);              % -mval
            R17=rect2(-Xr1+shift,Xr3,-Y1,Y1,0);                     % steel

    elseif -Xr2+shift <= Xr3 & -Xr1+shift > Xr3

            R13=rect2(-Xr3,-Xr1+shift-2*Xr3,-Y1,Y1,0);              % -mval
            R14=rect2(-Xr1+shift-2*Xr3,Xr1+shift-2*Xr3,-Y1,Y1,0);   % steel
            R15=rect2(Xr1+shift-2*Xr3,Xr2+shift-2*Xr3,-Y1,Y1,0);    % +mval
            R16=rect2(Xr2+shift-2*Xr3,-Xr2+shift,-Y1,Y1,0);         % steel
            R17=rect2(-Xr2+shift,Xr3,-Y1,Y1,0);                     % -mval

    elseif -Xr2+shift > Xr3

            R13=rect2(-Xr3,-Xr2+shift-2*Xr3,-Y1,Y1,0);              % steel
            R14=rect2(-Xr2+shift-2*Xr3,-Xr1+shift-2*Xr3,-Y1,Y1,0);  % -mval
            R15=rect2(-Xr1+shift-2*Xr3,Xr1+shift-2*Xr3,-Y1,Y1,0);   % steel
            R16=rect2(Xr1+shift-2*Xr3,Xr2+shift-2*Xr3,-Y1,Y1,0);    % +mval
            R17=rect2(Xr2+shift-2*Xr3,Xr3,-Y1,Y1,0);                % steel

    else    % nominal case w rotor centered

            R13=rect2(-Xr3,-Xr2+shift,-Y1,Y1,0);        % steel
            R14=rect2(-Xr2+shift,-Xr1+shift,-Y1,Y1,0);  % -mval
            R15=rect2(-Xr1+shift,Xr1+shift,-Y1,Y1,0);   % steel
            R16=rect2(Xr1+shift,Xr2+shift,-Y1,Y1,0);    % +mval
            R17=rect2(Xr2+shift,Xr3,-Y1,Y1,0);          % steel

    end
%===============================================================

% Bottom stator
R18=rect2(-Xs5,Xs5,-Y2,-Y1,0); R19=rect2(-Xs5,-Xs9,-Y3,-Y2,0);
R20=rect2(-Xs9,-Xs6,-Y3,-Y2,0); R21=rect2(-Xs6,Xs6,-Y3,-Y2,0);
R22=rect2(Xs6,Xs9,-Y3,-Y2,0); R23=rect2(Xs9,Xs5,-Y3,-Y2,0);
R24=rect2(-Xs5,-Xs8,-Y4,-Y3,0); R25=rect2(-Xs8,-Xs7,-Y4,-Y3,0);
R26=rect2(-Xs7,Xs7,-Y4,-Y3,0); R27=rect2(Xs7,Xs8,-Y4,-Y3,0);
R28=rect2(Xs8,Xs5,-Y4,-Y3,0); R29=rect2(-Xs5,Xs5,-Y5,-Y4,0);
objs={R1,R2,R3,R4,R5,R6,R7,R8,R9,R10,R11,R12,R13,R14,R15,R16,R17,R18,R19,
... R20,R21,R22,R23,R24,R25,R26,R27,R28,R29};
names={'R1','R2','R3','R4','R5','R6','R7','R8','R9','R10','R11','R12','R13',
...
'R14','R15','R16','R17','R18','R19','R20','R21','R22','R23','R24','R25',
... 'R26','R27','R28','R29'}; s.objs=objs; s.name=names;
```

```
objs={}; names={}; c.objs=objs; c.name=names;

objs={}; names={}; p.objs=objs; p.name=names;

drawstruct=struct('s',s,'c',c,'p',p); fem.draw=drawstruct;
fem.geom=geomcsg(fem);
%------------------------
%==================================
% Domain group assignments for R's
% 1=powdered iron (nonlin)
% 2=-ival (copper)
% 3=air
% 4=-mval(pm)
% 5=steel (no correction) (nonlin)
% 6=ival (copper)
% 7=mval (pm)
% 8=steel (w area correction) (nonlin)

% bot stator modified from original current configuration.

    if Xr1+shift <= Xr3 & Xr2+shift > Xr3       % small shift
        %       0 0 0 0 0 0 0 0 0 1 1 1 1 1 1 1 1 1 1 2 2 2 2 2 2 2 2 2 2
        %       1 2 3 4 5 6 7 8 9 0 1 2 3 4 5 6 7 8 9 0 1 2 3 4 5 6 7 8 9
        myRs = [1 8 6 8 2 8 5 3 5 3 5 3 7 5 4 5 7 3 3 5 3 5 3 6 8 2 8 6 1];
    elseif -Xr1+shift <= Xr3 & Xr1+shift > Xr3  % large shift
        %       0 0 0 0 0 0 0 0 0 1 1 1 1 1 1 1 1 1 1 2 2 2 2 2 2 2 2 2 2
        %       1 2 3 4 5 6 7 8 9 0 1 2 3 4 5 6 7 8 9 0 1 2 3 4 5 6 7 8 9
        myRs = [1 8 6 8 2 8 5 3 5 3 5 3 5 7 5 4 5 3 3 5 3 5 3 6 8 2 8 6 1];
    elseif -Xr2+shift <= Xr3 & -Xr1+shift > Xr3
        %       0 0 0 0 0 0 0 0 0 1 1 1 1 1 1 1 1 1 1 2 2 2 2 2 2 2 2 2 2
        %       1 2 3 4 5 6 7 8 9 0 1 2 3 4 5 6 7 8 9 0 1 2 3 4 5 6 7 8 9
        myRs = [1 8 6 8 2 8 5 3 5 3 5 3 4 5 7 5 4 3 3 5 3 5 3 6 8 2 8 6 1];
    elseif -Xr2+shift > Xr3
        %       0 0 0 0 0 0 0 0 0 1 1 1 1 1 1 1 1 1 1 2 2 2 2 2 2 2 2 2 2
        %       1 2 3 4 5 6 7 8 9 0 1 2 3 4 5 6 7 8 9 0 1 2 3 4 5 6 7 8 9
        myRs = [1 8 6 8 2 8 5 3 5 3 5 3 5 4 5 7 5 3 3 5 3 5 3 6 8 2 8 6 1];
    else    % nominal case w rotor centered
        %       0 0 0 0 0 0 0 0 0 1 1 1 1 1 1 1 1 1 1 2 2 2 2 2 2 2 2 2 2
        %       1 2 3 4 5 6 7 8 9 0 1 2 3 4 5 6 7 8 9 0 1 2 3 4 5 6 7 8 9
        myRs = [1 8 6 8 2 8 5 3 5 3 5 3 5 4 5 7 5 3 3 5 3 5 3 6 8 2 8 6 1];
    end

% Get mapping from R's to subdomains (mySt is a sparse matrix)
mySt=geomcsg(fem,'Out','st');

% Apply mapping to get domain group assignments for subdomains
mySubdomains=(full(mySt)*myRs')';
%==================================

%------------------------
clear appl

% Application mode 1
appl{1}.mode=flcemqap('dim',{'Az'},'sdim',{'x','y'},'submode','t2','tdiff',
... 'on'); appl{1}.name='qap'; appl{1}.dim={'Az'};
appl{1}.border='off';
appl{1}.var={'epsilon0','8.854187817e-12','mu0','4*pi*1e-7','omega','0'};
appl{1}.form='coefficient'; appl{1}.elemdefault='Lag2';
appl{1}.assign={'Bx';'Bx_qap';'By';'By_qap';'Dz';'Dz_qap';'Ez';'Ez_qap';
...
'Hx';'Hx_qap';'Hy';'Hy_qap';'Jez';'Jez_qap';'Jiz';'Jiz_qap';'Jvz';'Jvz_qap';
...
'Jz';'Jz_qap';'Mx';'Mx_qap';'My';'My_qap';'Poxav';'Poxav_qap';'Poyav';
```

```
...
'Poyav_qap';'Pz';'Pz_qap';'Qav';'Qav_qap';'Qiav';'Qiav_qap';'Qvav';
...
'Qvav_qap';'Wav';'Wav_qap';'Weav';'Weav_qap';'Wm';'Wm_qap';'Wmav';
...
'Wmav_qap';'eMx';'eMx_qap';'eMy';'eMy_qap';'ePz';'ePz_qap';'epsilon';
...
'epsilon_qap';'epsilon0';'epsilon0_qap';'mu';'mu_qap';'mu0';'mu0_qap';
...
'muxx';'muxx_qap';'muxy';'muxy_qap';'muyx';'muyx_qap';'muyy';'muyy_qap';
...
'nPoav';'nPoav_qap';'normB';'normB_qap';'normE';'normE_qap';'normH';
...
'normH_qap';'normJ';'normJ_qap';'omega';'omega_qap';'sigma';'sigma_qap';
... 'tH';'tH_qap';'vx';'vx_qap';'vy';'vy_qap'};
appl{1}.shape={'shlag(2,''Az'')'}; appl{1}.sshape=2;
appl{1}.equ.sigma={{{'0'}},{{'0'}},{{'0'}},{{'0'}},{{'0'}},{{'0'}},{{'0'}},{{'0'}}};
appl{1}.equ.mur={{{'u26/(1+C3*normB_qap^2)+1'}},{{'1'}},{{'1'}},{{'1'}},
...
{{'uFe/(1+C*normB_qap^2)+1'}},{{'1'}},{{'1'}},{{'uFe2/(1+C2*normB_qap^2)+1'}}};
appl{1}.equ.murtensor={{{'1','0';'0','1'}},{{'1','0';'0','1'}},{{'1','0';
...
'0','1'}},{{'1','0';'0','1'}},{{'1','0';'0','1'}},{{'1','0';'0','1'}},{{'1',
... '0';'0','1'}},{{'1','0';'0','1'}}};
appl{1}.equ.M={{{'0','0'}},{{'0','0'}},{{'0','0'}},{{'-mval','0'}},{{'0',
... '0'}},{{'0','0'}},{{'mval','0'}},{{'0','0'}}};
appl{1}.equ.Jext={{{'0'}},{{'-ival'}},{{'0'}},{{'0'}},{{'0'}},{{'ival'}},
... {{'0'}},{{'0'}}};
appl{1}.equ.v={{{'0','0'}},{{'0','0'}},{{'0','0'}},{{'0','0'}},{{'0','0'}},
... {{'0','0'}},{{'0','0'}},{{'0','0'}}};
appl{1}.equ.epsilonr={{{'1'}},{{'1'}},{{'1'}},{{'1'}},{{'1'}},{{'1'}},
... {{'1'}},{{'1'}}};
appl{1}.equ.P={{{'0'}},{{'0'}},{{'0'}},{{'0'}},{{'0'}},{{'0'}},{{'0'}},{{'0'}}};
appl{1}.equ.mutype={'iso','iso','iso','iso','iso','iso','iso','iso'};
appl{1}.equ.gporder={{4},{4},{4},{4},{4},{4},{4},{4}};
appl{1}.equ.cporder={{2},{2},{2},{2},{2},{2},{2},{2}};
appl{1}.equ.shape={1,1,1,1,1,1,1,1};
appl{1}.equ.init={{{'0'}},{{'0'}},{{'0'}},{{'0'}},{{'0'}},{{'0'}},{{'0'}},{{'0'}}};
appl{1}.equ.usage={1,1,1,1,1,1,1,1};
%---------------------------
appl{1}.equ.ind=mySubdomains;
%---------------------------
appl{1}.bnd.H={{{'0'},{'0'}},{{'0'},{'0'}}};
appl{1}.bnd.Js={{{'0'}},{{'0'}}}; appl{1}.bnd.A={{{'0'}},{{'0'}}};
appl{1}.bnd.type={'A0','tH0'}; appl{1}.bnd.gporder={{0},{0}};
appl{1}.bnd.cporder={{0},{0}}; appl{1}.bnd.shape={0,0};
appl{1}.bnd.ind=[1 1 1 2 1 2 1 2 1 2 1 2 1 2 1 2 1 2 1 2 2 2 2 2 2 2
2 2 2  ... 2 2 2 2 2 2 2 2 2 2 2 2 2 2 2 2 2 2 2 2 2 2 2 2 2 2 2 2 2 2
2 2 2 2 2 2 2 2 2  ... 2 2 2 2 2 2 2 2 2 2 2 2 2 1 1 1 1 1 1 1 1 1];

fem.appl=appl;

% Symmetry boundaries
fem.equiv=[1 3 5 7 9 11 13 15 17;80 81 82 83 84 85 86 87 88];

% Initialize mesh
fem.mesh=meshinit(fem,...
    'Out',    {'mesh'},...
    'jiggle', 'mean',...
    'Hcurve', 0.29999999999999999,...
    'Hgrad',  1.3,...
    'Hmax',   {[],zeros(1,0),zeros(1,0),zeros(1,0)},...
    'Hnum',   {[],zeros(1,0)},...
```

```
    'Hpnt',   {10,zeros(1,0)});

% Dimension
fem.dim={'Az'};

% Boundary conditions
fem.border=1;

% Problem form
fem.form='coefficient';

% Geometry element order
fem.sshape=2;

% Differentiation simplification
fem.simplify='on';

% Define application mode variables
fem.var={...
    'epsilon0_qap','8.854187817e-12',...
    'mu0_qap','4*pi*1e-7'};

% Point settings
clear pnt pnt.var={}; pnt.ind=ones(1,60); pnt.weak={{{'0'}}};
pnt.dweak={{{'0'}}}; pnt.constr={{{'0'}}}; pnt.init={{{''}}};
pnt.shape={1}; pnt.expr={}; fem.pnt=pnt;

% Boundary conditions
clear bnd bnd.var={'tH_qap','ncu1+nalu1-nga1'}; bnd.vart={};
bnd.varu={}; bnd.ind=[1 1 1 2 1 2 1 2 1 2 1 2 1 2 1 2 1 2 1 2 2 2 2
2 2 2 2 2 2 2 2 2 2  ... 2 2 2 2 2 2 2 2 2 2 2 2 2 2 2 2 2 2 2 2 2 2
2 2 2 2 2 2 2 2 2 2 2 2 2 2 2 2  ... 2 2 2 2 2 2 2 2 2 3 3 3 3 3 3 3 3
3]; bnd.q={{{'0'}},{{'0'}},{{'0'}}};
bnd.g={{{'0'}},{{'0'}},{{'0'}}}; bnd.h={{{'1'}},{{'0'}},{{'-1'}}};
bnd.r={{{'0'}},{{'0'}},{{'0'}}}; bnd.weak={{{'0'}},{{'0'}},{{'0'}}};
bnd.dweak={{{'0'}},{{'0'}},{{'0'}}};
bnd.constr={{{'0'}},{{'0'}},{{'0'}}};
bnd.init={{{''}},{{''}},{{''}}}; bnd.gporder={{4},{1},{4}};
bnd.cporder={{2},{1},{2}}; bnd.shape={1,1,1}; bnd.expr={};
fem.bnd=bnd;

% PDE coefficients
clear equ equ.var={'mu_qap',{'u26/(1+C3*normB_qap^2)+1','1','1','1',
...
'uFe/(1+C*normB_qap^2)+1','1','1','uFe2/(1+C2*normB_qap^2)+1'},'muxx_qap',...
{'u26/(1+C3*normB_qap^2)+1',...
'1','1','1','uFe/(1+C*normB_qap^2)+1','1','1','uFe2/(1+C2*normB_qap^2)+1'},'muxy_qap',...
{'0','0','0','0', ...
'0','0','0','0'},'muyx_qap',{'0','0','0','0','0','0','0','0'},'muyy_qap',...
{'u26/(1+C3*normB_qap^2)+1','1','1','1','uFe/(1+C*normB_qap^2)+1','1','1',...
'uFe2/(1+C2*normB_qap^2)+1'}, ...
'epsilon_qap',{'1','1','1','1','1','1','1','1'},'sigma_qap',{'0','0','0','0',...
'0','0','0','0'},'ePz_qap',{'0','0','0','0','0','0','0','0'},'eMx_qap',{'0','0','0',...
'-mval','0','0','mval','0'},'eMy_qap',{'0','0','0','0','0','0','0','0'},'Jez_qap',...
{'0','-ival','0','0','0','ival','0','0'},'vx_qap',{'0','0','0','0','0','0','0','0'},...
'vy_qap',{'0','0','0','0','0','0','0','0'},'Bx_qap','Azy','By_qap','-Azx',...
'normB_qap','sqrt(Bx_qap.*conj(Bx_qap)+By_qap.*conj(By_qap))','Hx_qap',...
'(cu1y+alu1y-ga1y)','Hy_qap','-(cu1x+alu1x-ga1x)','normH_qap', ...
'sqrt(Hx_qap.*conj(Hx_qap)+Hy_qap.*conj(Hy_qap))','Mx_qap', ...
'Bx_qap./mu0_qap-Hx_qap','My_qap','By_qap./mu0_qap-Hy_qap','Wm_qap',...
'0.5.*(Hx_qap.*Bx_qap+Hy_qap.*By_qap)'}; equ.vart={}; equ.varu={};
%--------------------
equ.ind=mySubdomains;
```

```
%--------------------
equ.da={{{'0'}},{{'0'}},{{'0'}},{{'0'}},{{'0'}},{{'0'}},{{'0'}},{{'0'}}};
equ.c={{{'1/mu0_qap/((1+u26/(1+C3*normB_qap^2))*(1+u26/(1+C3*normB_qap^2)))*...
(1+u26/(1+C3*normB_qap^2))','0','0', ...
'1/mu0_qap/((1+u26/(1+C3*normB_qap^2))*(1+u26/(1+C3*normB_qap^2)))*...
(1+u26/(1+C3*normB_qap^2))'}},...
{{'1/mu0_qap','0','0','1/mu0_qap'}},{{'1/mu0_qap','0','0','1/mu0_qap'}},...
{{'1/mu0_qap','0','0','1/mu0_qap'}}, ...
{{'1/mu0_qap/((1+uFe/(1+C*normB_qap^2))*(1+uFe/(1+C*normB_qap^2)))*...
(1+uFe/(1+C*normB_qap^2))','0','0', ...
'1/mu0_qap/((1+uFe/(1+C*normB_qap^2))*(1+uFe/(1+C*normB_qap^2)))*...
(1+uFe/(1+C*normB_qap^2))'}},...
{{'1/mu0_qap','0','0','1/mu0_qap'}},{{'1/mu0_qap','0','0','1/mu0_qap'}},...
{{'1/mu0_qap/((1+uFe2/(1+C2*normB_qap^2))*(1+uFe2/(1+C2*normB_qap^2)))*...
(1+uFe2/(1+C2*normB_qap^2))','0','0', ...
'1/mu0_qap/((1+uFe2/(1+C2*normB_qap^2))*(1+uFe2/(1+C2*normB_qap^2)))*...
(1+uFe2/(1+C2*normB_qap^2))'}}};
equ.al={{{'0';'0'}},{{'0';'0'}},{{'0';'0'}},{{'0';'0'}},{{'0';'0'}},{{'0';
... '0'}},{{'0';'0'}},{{'0';'0'}}};
equ.ga={{{'0','0'}},{{'0','0'}},{{'0','0'}},{{'0','-mval'}},{{'0','0'}},
... {{'0','0'}},{{'0','mval'}},{{'0','0'}}};
equ.be={{{'0','0'}},{{'0','0'}},{{'0','0'}},{{'0','0'}},{{'0','0'}},{{'0',
... '0'}},{{'0','0'}},{{'0','0'}}};
equ.a={{{'0'}},{{'0'}},{{'0'}},{{'0'}},{{'0'}},{{'0'}},{{'0'}},{{'0'}}};
equ.f={{{'0'}},{{'-ival'}},{{'0'}},{{'0'}},{{'0'}},{{'ival'}},{{'0'}},{{'0'}}};
equ.weak={{{'0'}},{{'0'}},{{'0'}},{{'0'}},{{'0'}},{{'0'}},{{'0'}},{{'0'}}};
equ.dweak={{{'0'}},{{'0'}},{{'0'}},{{'0'}},{{'0'}},{{'0'}},{{'0'}},{{'0'}}};
equ.constr={{{'0'}},{{'0'}},{{'0'}},{{'0'}},{{'0'}},{{'0'}},{{'0'}},{{'0'}}};
equ.init={{{'0'}},{{'0'}},{{'0'}},{{'0'}},{{'0'}},{{'0'}},{{'0'}},{{'0'}}};
equ.gporder={{4},{4},{4},{4},{4},{4},{4},{4}};
equ.cporder={{2},{2},{2},{2},{2},{2},{2},{2}};
equ.shape={1,1,1,1,1,1,1,1}; equ.expr={}; fem.equ=equ;

% Shape functions
fem.shape={'shlag(2,''Az'')'};

% Differentiation rules
fem.rules={};

% Define variables
fem.variables={...
    'uo',     1.2566370614359173e-006,...
    'uFe',    1000,...
    'uFe2',   1000/AtError,...
    'C',      25,...
    'C2',     25*AtError^2,...
    'C3',     25*AbError^2,...
    'Br',     1.2,...
    'mval',   954929.65855137201,...
    'ival',   405/((Xs4-Xs1)*(Y4-Y3)),...
    'u26',    75/AbError};
fem.eleminitmph=cell(1,0); fem.elemmph=cell(1,0);

% Extend the mesh
fem.xmesh=meshextend(fem,'context','local','cplbndeq','on','cplbndsh','on');

% Evaluate initial condition
init=asseminit(fem,...
    'context','local',...
    'init',   fem.xmesh.eleminit);

% Solve nonlinear problem
fem.sol=femnlin(fem,...
```

```
    'out',    'sol',...
    'stop',   'on',...
    'init',   init,...
    'report', 'on',...
    'context','local',...
    'sd',     'off',...
    'nullfun','flnullorth',...
    'blocksize',5000,...
    'solcomp',{'Az'},...
    'linsolver','matlab',...
    'bsteps', 0,...
    'ntol',   9.9999999999999995e-007,...
    'hnlin',  'off',...
    'jacobian','equ',...
    'maxiter',25,...
    'method', 'eliminate');

% Save current fem structure for restart purposes
fem0=fem;

%=================================================
% Calculate Flux linkage
    % figure out which subdomains to consider - want R4 and R25
        R4vect=[zeros(3,1);1;zeros(25,1)];
        newR4=find(mySt*R4vect==1);

        R2vect=[0;1;zeros(27,1)];
        newR2=find(mySt*R2vect==1);

        R6vect=[zeros(5,1);1;zeros(23,1)];
        newR6=find(mySt*R6vect==1);

        R25vect=[zeros(24,1);1;zeros(4,1)];
        newR25=find(mySt*R25vect==1);

    % integrate By over subdomain
        B_int_4=postint(fem,'By_qap','Dl',[newR4]);
        B_int_2_6=postint(fem,'By_qap','Dl',[newR2 newR6]);
        B_int_25=postint(fem,'By_qap','Dl',[newR25]);

    % divide by area to get average By
        B_avg_4(indx)=B_int_4/(2*Xs1*(Y4-Y3));
        B_avg_2_6(indx)=B_int_2_6/(2*Xs1*(Y4-Y3));
        B_avg_25(indx)=B_int_25/(2*Xs1*(Y4-Y3));

    % multiply by z oriented area and P/2 to get flux
        lam_4(indx)=B_avg_4(indx)*(2*Xs1*0.8*ell);
        lam_2_6(indx)=B_avg_2_6(indx)*(2*Xs1*0.8*ell);
        lam_25(indx)=B_avg_25(indx)*(2*Xs1*0.8*ell);

%=================================================
% Calculate Coenergy
pmDomains=[find(mySubdomains==4),find(mySubdomains==7)];
pmWc(indx)=postint(fem,'mu_qap*4*pi*1e-7*(0.5*(Hx_qap^2+Hy_qap^2)+Mx_qap*Hx_qap+My_qap*Hy_qap)',
...
    'Dl',pmDomains);

airDomains=[find(mySubdomains==2),find(mySubdomains==3),find(mySubdomains==6)];
airWc(indx)=postint(fem,'0.5*mu_qap*4*pi*1e-7*(Hx_qap^2+Hy_qap^2)','Dl',airDomains);

fe1Domains=[find(mySubdomains==1)];
fe1Wc(indx)=postint(fem,'(Bx_qap*Hx_qap+By_qap*Hy_qap)-(1/2/uo*normB_qap^2-...
1/uo*u26*normB_qap/((u26+1)*C3)^(1/2)*atan(C3*normB_qap/((u26+1)*C3)^(1/2))+...
```

```
1/2/uo*u26/C3*log(1+C3*normB_qap^2/(u26+1)))','Dl',fe1Domains);

fe5Domains=[find(mySubdomains==5)];
fe5Wc(indx)=postint(fem,'(Bx_qap*Hx_qap+By_qap*Hy_qap)-(1/2/uo*normB_qap^2-...
1/uo*uFe*normB_qap/((uFe+1)*C)^(1/2)*atan(C*normB_qap/((uFe+1)*C)^(1/2))+...
1/2/uo*uFe/C*log(1+C*normB_qap^2/(uFe+1)))','Dl',fe5Domains);

fe8Domains=[find(mySubdomains==8)];
fe8Wc(indx)=postint(fem,'(Bx_qap*Hx_qap+By_qap*Hy_qap)-(1/2/uo*normB_qap^2-...
1/uo*uFe2*normB_qap/((uFe2+1)*C2)^(1/2)*atan(C2*normB_qap/((uFe2+1)*C2)^(1/2))+...
1/2/uo*uFe2/C2*log(1+C2*normB_qap^2/(uFe2+1)))','Dl',fe8Domains);

%==================================================

% Plot solution
% figure(indx);
% postplot(fem,...
%   'geomnum',1,...
%   'context','local',...
%   'tridata',{'normB_qap','cont','internal'},...
%   'trifacestyle','interp',...
%   'triedgestyle','none',...
%   'trimap', 'jet',...
%   'trimaxmin','off',...
%   'tridlim',[0 2],...
%   'tribar', 'on',...
%   'arrowdata',{'Bx_qap','By_qap'},...
%   'arrowcolor',[1 0 0],...
%   'arrowscale',0.20000000000000001,...
%   'arrowstyle','normalized',...
%   'arrowxspacing',15,...
%   'arrowyspacing',20,...
%   'arrowmaxmin','off',...
%   'geom',   'on',...
%   'geomcol','bginv',...
%   'refine', 3,...
%   'contorder',2,...
%   'phase',  0,...
%   'title',  'Surface: (normB_qap)  Arrow: [(Bx_qap), (By_qap)]  ',...
%   'renderer','zbuffer',...
%   'solnum', 1,...
%   'axisvisible','on')

%postplot(fem,...
%    'geomnum',1,...
%    'context','local',...
%    'contdata',{'Az','cont','internal'},...
%    'contlevels',20,...
%    'contstyle','bginv',...
%    'contlabel','off',...
%    'contmaxmin','off',...
%    'contbar','off',...
%    'contmap','cool',...
%    'geom',   'on',...
%    'geomcol','bginv',...
%    'refine', 3,...
%    'contorder',2,...
%    'phase',  0,...
%    'title',  '',...
%    'renderer','zbuffer',...
%    'solnum', 1,...
%    'axisvisible','on')
```

```
end % rotor position loop

Wc=(airWc+fe1Wc+fe5Wc+fe8Wc+pmWc);    % Sum coenergies
dWc=diff(Wc); dWc=dWc(1:2:numIter-1); dSh=diff(shiftVect1);
dSh=dSh(1:2:numIter-1);
Force=dWc./dSh;                 % This is a force density (force per radial length)
eval(strcat('save apr_20_int_',num2str(rxCount)));
eval(strcat('F',num2str(rxCount),'=Force;'));

% end radius loop
end

%============================
invRmat=inv([rxVect'.^2, rxVect',ones(3,1)]);

for foo=1:max(size(Force))

   % fit 2nd order polynomial
   b=[F1(foo);F2(foo);F3(foo)];
   a=invRmat*b;

   fullTorque(foo)=(a(1)/4)*(rxVect(3)^4-rxVect(1)^4)+...
      (a(2)/3)*(rxVect(3)^3-rxVect(1)^3)+...
      (a(3)/2)*(rxVect(3)^2-rxVect(1)^2);

% end torque calculation loop
end
%============================

eval(strcat('save apr_20_a'));
```

Appendix D

Mechanical Drawings

D.1 Millimeter-Scale Generator Components

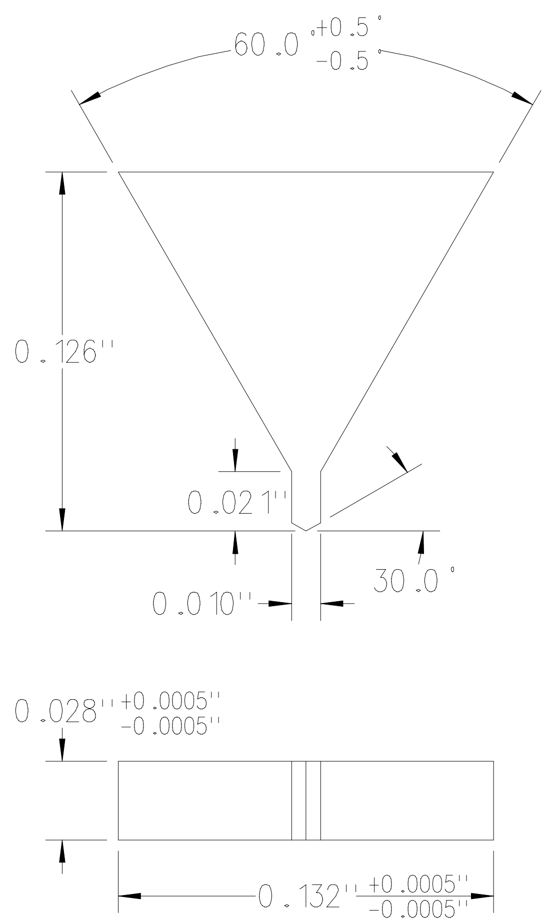

ACTUAL SIZE:

STATOR CORE BASE	7/15/03	FINAL
SCALE 20:1	MAT'L: -26	
MAKE 32 PARTS		ALL TOLERANCES +0.0010/-0.0010 UNLESS OTHERWISE NOTED
MATTHEW SENESKY	(510) 643-5895	UC BERKELEY POWER ELECTRONICS

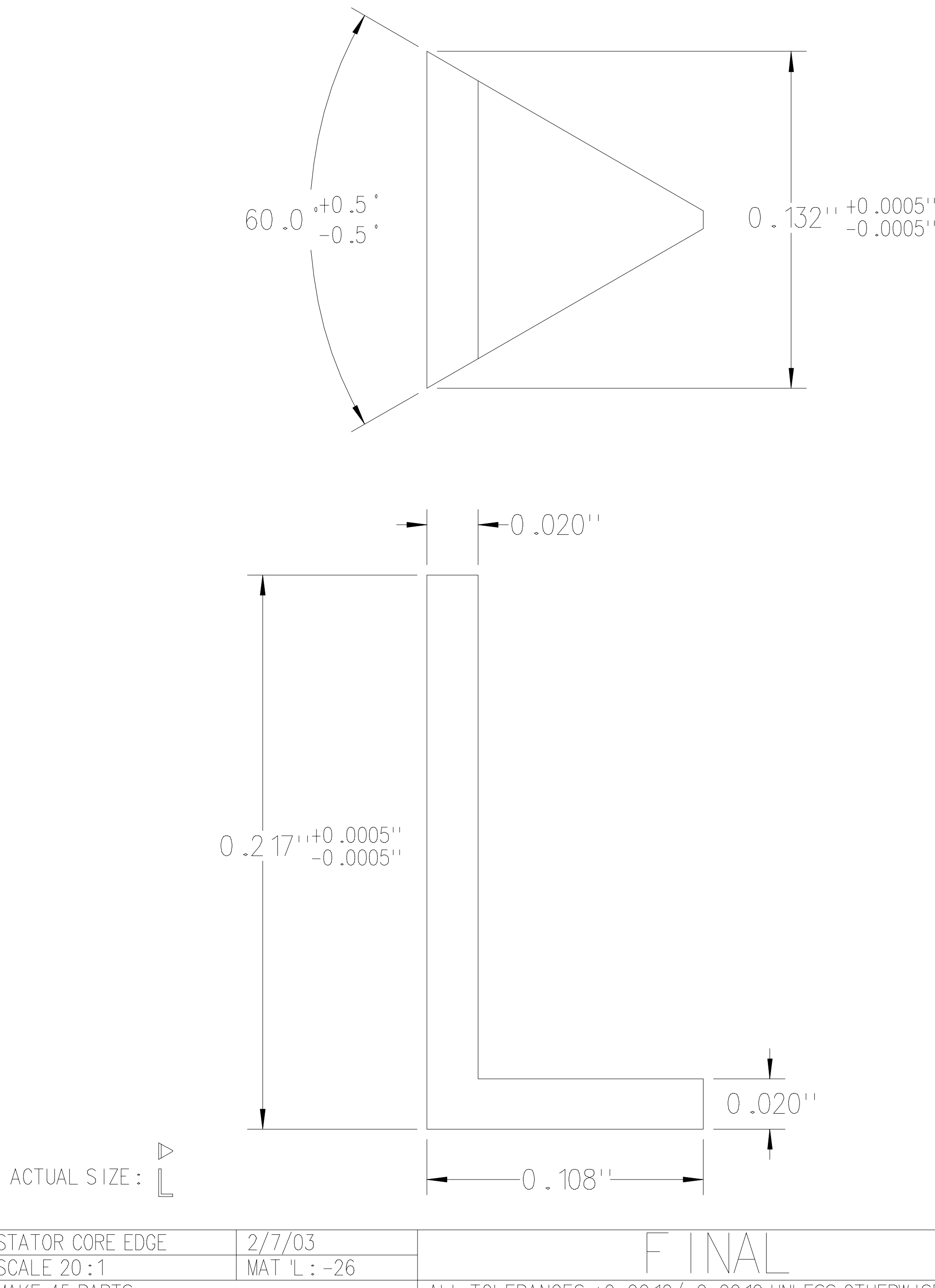

STATOR CORE EDGE	2/7/03	FINAL
SCALE 20:1	MAT'L: -26	
MAKE 45 PARTS		ALL TOLERANCES +0.0010/-0.0010 UNLESS OTHERWISE NOTED
MATTHEW SENESKY	(510) 643-5895	UC BERKELEY POWER ELECTRONICS

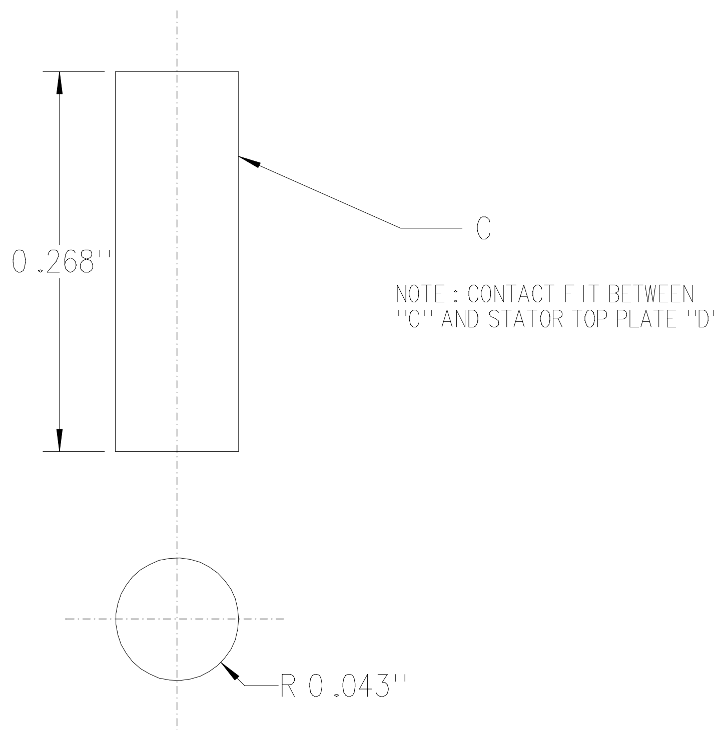

ACTUAL SIZE: 

STATOR CORE POST	2/7/03	FINAL
SCALE 10:1	MAT'L: -26	
MAKE 15 PARTS		ALL TOLERANCES +0.0010/-0.0010 UNLESS OTHERWISE NOTED
MATTHEW SENESKY	(510) 643-5895	UC BERKELEY POWER ELECTRONICS

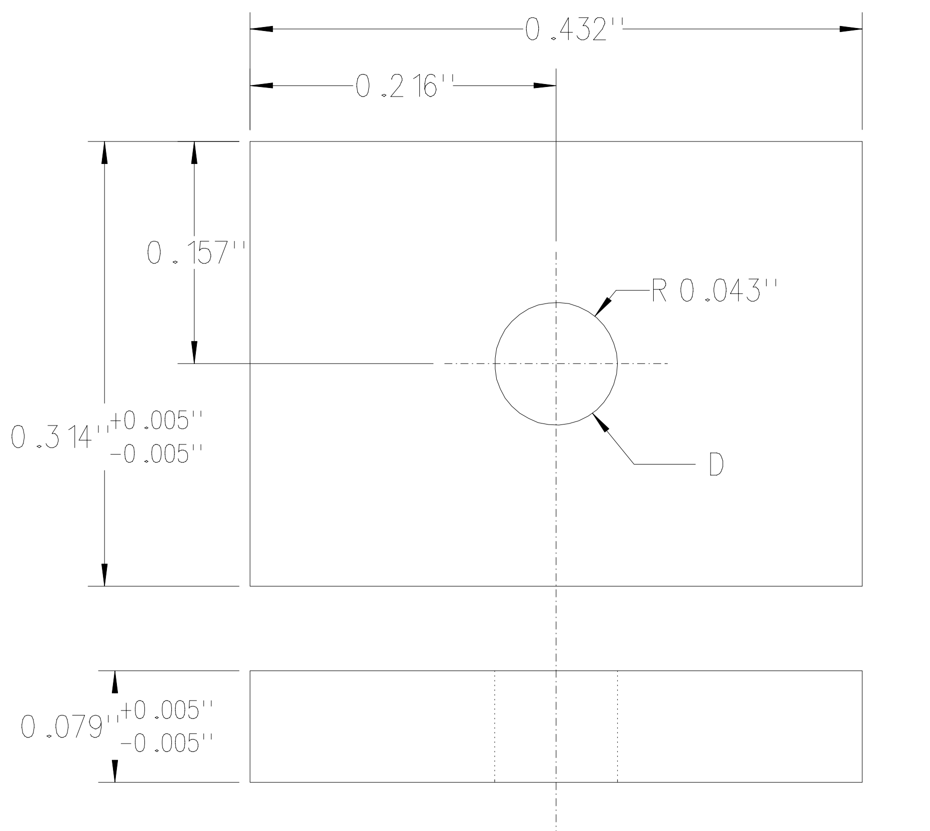

NOTE: CONTACT FIT BETWEEN
''D'' AND STATOR CORE POST ''C''

ACTUAL SIZE:

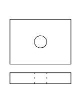

STATOR TOP PLATE	2/7/03	FINAL
SCALE 10:1	MAT'L: -26	
MAKE 15 PARTS		ALL TOLERANCES +0.0010/-0.0010 UNLESS OTHERWISE NOTED
MATTHEW SENESKY	(510) 643-5895	UC BERKELEY POWER ELECTRONICS

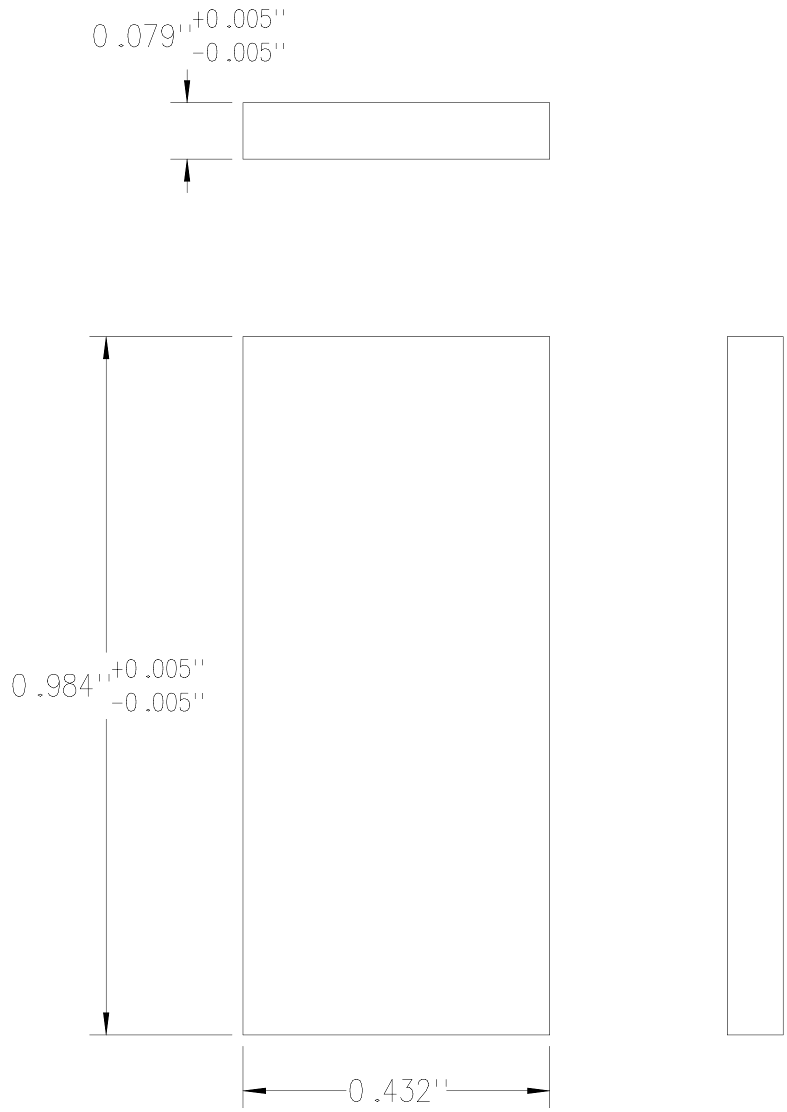

ACTUAL SIZE: 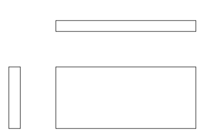

STATOR BOTTOM PLATE	2/7/03	FINAL
SCALE 5:1	MAT'L: -26	
MAKE 15 PARTS		ALL TOLERANCES +0.0010/-0.0010 UNLESS OTHERWISE NOTED
MATTHEW SENESKY	(510) 643-5895	UC BERKELEY POWER ELECTRONICS

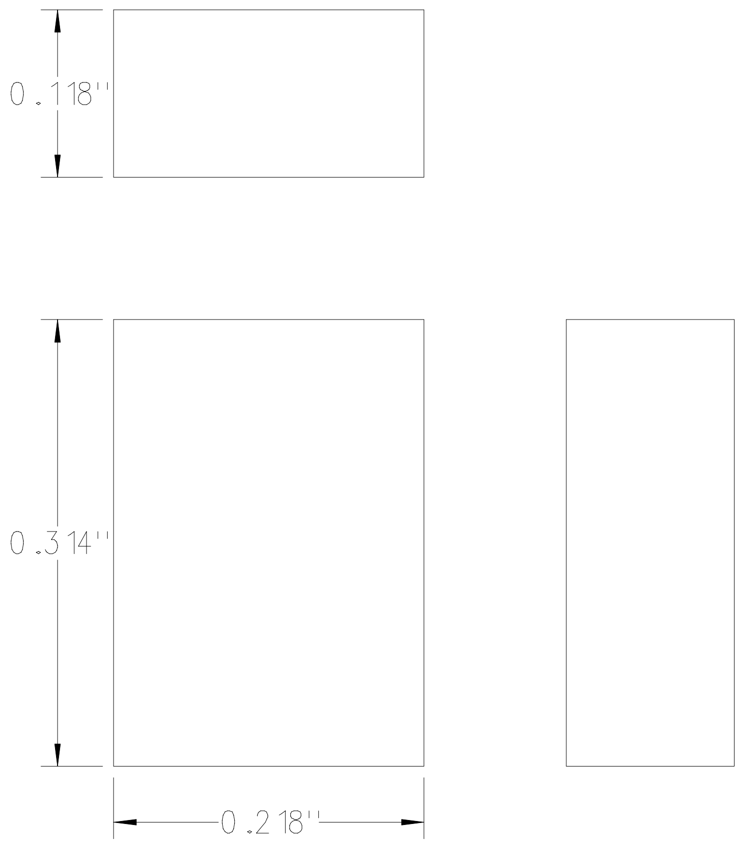

ACTUAL SIZE:

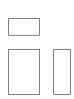

STATOR SIDE PLATE	2/9/03	FINAL
SCALE 10:1	MAT'L: -26	
MAKE 30 PARTS		ALL TOLERANCES +0.0050/-0.0050 UNLESS OTHERWISE NOTED
MATTHEW SENESKY	(510) 643-5895	UC BERKELEY POWER ELECTRONICS

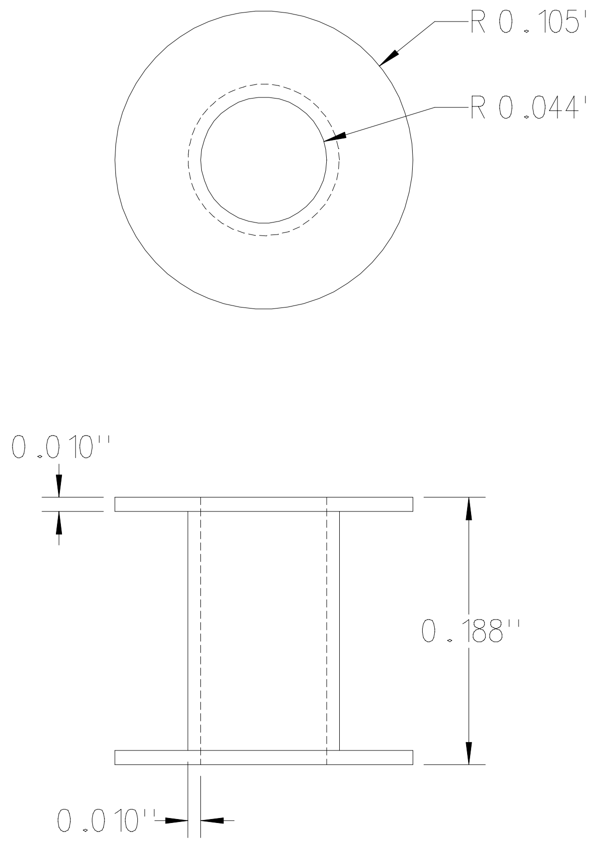

ACTUAL SIZE:

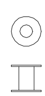

BOBBIN	2/6/03	FINAL
SCALE 10:1	MAT'L: DELRIN	
MAKE 15 PARTS		ALL TOLERANCES +0.0010/-0.0010 UNLESS OTHERWISE NOTED
MATTHEW SENESKY	(510) 643-5895	UC BERKELEY POWER ELECTRONICS